الجـــــــــــــــــــــــــــمهـوريـــــــة الجـــــــــــــــزائـريـة الديمـــــــقـراطيـة الشـــــــــعبيـة

PEOPLE'S DEMOCRATIC REPUBLIC OF ALGERIA

وزارة التـــــــــــــــــــــــــــــعـليـم العـــــــالي و البـــــــــــحث العـــــلـمـــي

Ministry of Higher Education and Scientific Research

جـــــــــــــــامعة أبي بكـــر بـلـقـايد – تـلمســـــــــــــان –

Abou Bekr Belkaïd University – Tlemcen –
Faculty of TECHNOLOGY

THESIS

Presented to obtain the **3rd Cycle DOCTORATE degree**

In : Telecommunication

Speciality : Optical and Microwave Telecommunications

By: ***Imam Abderrahmane***

Subject

Plasmonic Microstructure: Study And Applications

Publicly defended, the. 06/06/2024 , before the jury composed of:

MELIANI Maghnia	Prof	Univ. Tlemcen	President
BADAOUI Hadjira	Prof	Univ. Tlemcen	Supervisor
ABRI Mehadji	Prof	Univ. Tlemcen	Co- Supervisor
ABID HAMZA	Prof	Univ. Sidi Bel Abbes	Examiner
ANANI MACHO	Prof	Univ. Sidi Bel Abbes	Examiner
RAHMI BACHIR	MRB	INRE. Alger	Guest

Abstract

The advent of optical fibers marked a groundbreaking revolution in telecommunication systems, enabling high-speed data transmission and information rates per second. The integration of all-optical devices further enhanced the efficiency of these systems. In recent years, plasmonic microstructures have garnered significant attention for their potential application in telecommunications due to their ability to overcome the diffraction limit and manipulate light at the subwavelength scale. This is particularly crucial in addressing challenges faced by crystal photonic systems. Recognizing the potential of plasmonics, the objective of this thesis is to investigate and design novel plasmonic structures suitable for implementation in Wavelength Division Multiplexing (WDM) systems, specifically as demultiplexers. The focus is on achieving the highest number of outputs and superior characteristics compared to existing works in the field, contributing to the advancement of telecommunications technology.

Keywords:

Plasmonic, diffraction limit, subwavelength scale, wavelength division multiplexing(WDM), demultiplexers.

ملخص:

ظهور الألياف البصرية قام بثورة رائدة في أنظمة الاتصالات، مما سمح بنقل البيانات بسرعة عالية ومعدلات معلوماتية مرتفعة في الثانية . دمج الأجهزة البصرية بالكامل عزز بشكل إضافي كفاءة هذه الأنظمة. في السنوات الأخيرة، جذبت هياكل البلازمون الميكرومترية اهتماماً كبيراً نظرًا لإمكانيتها في التطبيقات المحتملة في مجال الاتصالات بسبب قدرتها على التغلب على حد الانكسار وتلاعب الضوء على نطاق تحت الطول الموجي الفرعي. وهذا يكون خاصة حيويًا في مواجهة التحديات التي تواجهها أنظمة البصريات البلورية. مع الاعتراف بإمكانيات البلازمونيات، تهدف هذا الأطروحة إلى استكشاف وتصميم هياكل بلازمونية مبتكرة خصوصا كمزيلات تعدد الإرسال. يتم التركيز أيضا على تحقيق أعلى عدد من المخرجات بمخرجات وخصائص متفوقة مقارنة بالأعمال الحالية في المجال، مما يسهم في تقدم تكنولوجيا الإتصالات.

الكلمات المفتاحية:

البلازمونات، حدة الإنكسار، نطاق الطول الموجي الفرعي، مزيل تعدد الإرسال.

Résumé

L'avènement des fibres optiques a marqué une révolution fondamentale dans les systèmes de télécommunication, permettant une transmission de données à haute vitesse et des taux d'information par seconde élevés. L'intégration de dispositifs tout optiques a encore amélioré l'efficacité de ces systèmes. Ces dernières années, les microstructures plasmoniques ont suscité une attention particulière en raison de leur potentiel d'application dans les télécommunicati -ons, en surmontant la limite de diffraction et en manipulant la lumière à l'échelle sublongueur d'onde. Ceci est particulièrement crucial pour relever les défis auxquels font face les systèmes photoniques à cristal. Reconnaissant le potentiel de la plasmonique, l'objectif de cette thèse est d'investiguer et de concevoir de nouvelles structures plasmoniques adaptées à une implémentation dans les systèmes de Multiplexage par Répartition en Longueur d'Onde (WDM), spécifiquement en tant que démultiplexeurs. L'accent est mis sur l'obtention du nombre le plus élevé de sorties et de caractéristiques supérieures par rapport aux travaux existants dans le domaine, contribuant ainsi à l'avancement de la technologie des télécommunications.

Mots clé:

Plasmonique, limite de diffraction, échelle sub-longueur d'onde, multiplexage en longueur d'onde (WDM), démultiplexeurs.

Acknowledgements

We humbly express our deepest gratitude to the Almighty **Allah**, whose boundless grace empowered us with unwavering strength, indomitable courage, and enduring patience to embark upon this remarkable endeavor. We would like to extend our sincere thanks and appreciations to the supervisor **Pr. BADAOUI Hadjira** and **Pr. ABRI Mehadji** for leading this work. I sincerely thank the examiners **Pr. MELIANI Maghnia** , **Pr. ABID HAMZA**, **Pr. ANANI MACHO** and **Dr. RAHMI BACHIR** for accepting and reviewing our dissertation. I am extremely grateful to all the teachers in the telecommunication department who contributed to our training. Lastly, I want to express my deep appreciation to everyone who provided constant encouragement and support throughout the preparation of our work.

Dedication

In loving memory of my cherished parents, the guiding stars of my life, and the unwavering support they have bestowed upon me. To my brothers, who have shared both laughter and tears, and remain my pillars of strength.

To my dearest friends, whose unwavering presence has filled my days with joy and warmth and whose unwavering support has been a constant source of inspiration.

To the exceptional staff of Tlemcen University, whose dedication to education and nurturing minds has shaped me into the person I am today. Your commitment to excellence has fueled my ambitions and pushed me beyond my limits. This dedication is a testament to the love, encouragement,

and guidance I have received from my remarkable family, treasured friends, and the esteemed university staff. You have all played an invaluable role in shaping my journey, and I am forever grateful.

Abderrahmane

Contents

List of Figures

List of Tables

INTRODUCTION

In recent years, notable strides have been achieved in wireless communication systems, marking the onset of a transformative era that has reached its pinnacle with the advent of 5G. This technological leap encompasses paradigm-defining techniques such as network softwarization, virtualization, massive MIMO ultra-densification, and the introduction of new frequency bands [1]. However, the ever-growing demand for higher data rates and bandwidth have prompted researchers and regulatory communities to engage in discussions about the vision for 6G networks [2]. This arises due to a significant increase in the number of new use cases that 5G cannot adequately support, such as holographic teleportation, requiring *Tbps*-level data rates and microsecond-level latency [1].

During the pandemic, wireless communication saw a roughly 40% increase, while teleconferencing surged by nearly 300% [3]. Next-generation networks are expected to provide multi-Tb/s data transmission using the unallocated THz spectrum. To make this a reality, THz connections must seamlessly integrate with a range of inter/intra chip nanoelectronic functionalities to minimize communication performance bottlenecks [2]. Plasmonic nano devices have recently emerged as a promising alternative in this regard. Another crucial advantage of this technology is its ability to achieve high-speed optical signal transmission with device sizes below the diffraction limit, confining light at sub-wavelength dimensions, thereby allowing for higher integration levels [4][5][6].

Plasmonics, a crucial element of the field of nanophotonics, explores how electromagnetic fields can be confined over sub-wavelength scales. Plasmonic nanostructures find applications in optical signal filtering, transmission, detection, guiding, and modulation with lightning-fast speed and the highest bandwidth. Plasmonic devices can be 100 times smaller and 1000 times faster than current photonic devices, with footprints ranging from 1 to 100 μm^2. The capacity to manipulate light at the nanoscale seems strongly connected to the next major technological development.

In recent decades, the rapid development of vertical-cavity surface-emitting lasers, microdisk lasers, photonic crystal lasers, and nanowire lasers exemplifies the success of laser miniaturization, aiming for faster coherent light sources with lower power consumption [7]. These semiconductor lasers uti-

lize smaller microscale cavities to improve light-matter interaction, resulting in higher laser modulation speeds, lower thresholds, and reduced power consumption. The diffraction limit impedes their continued miniaturization deep into the nanometer scale, while pure dielectric micro-cavities can reach scales approaching half the wavelength of light [8]. Plasmonics can support propagation modes coupled to metallic surfaces and confine the wave at the subwavelength scale, garnering significant interest for its potential to overcome the diffraction limit and allow higher integration levels.

This significant development in light sources is accompanied by the creation of new mechanisms to manipulate all devices connected to networks using light, aiming for the greatest possible efficiency. In recent years, substantial work has been done in utilizing the THz spectrum, from infrared to visible light, to fulfill the increasing requirement for greater data speeds, bigger bandwidths, lower power consumption, and improved on-chip integrability in telecommunications applications. Metallic nanostructures' unique capacity to absorb and confine light at sub-wavelength dimensions has emerged as a potential option in this context [9]. Electromagnetic waves that propagate over metal-insulator interfaces are known as surface plasmons (SPs) [10], and plasmonic devices based on SPPs have already been built in various forms.

The innovative Wavelength-Division Multiplexing (WDM) technology enables the simultaneous transmission of diverse optical channels, each characterized by a distinct wavelength, over a singular fiber. This approach serves as a highly effective means to fully exploit the favorable low-loss properties inherent in fibers within the extended wavelength range. The advancements in Wavelength Division Multiplexing (WDM), strategically dividing the available bandwidth into smaller, more manageable channels, position it as a pivotal technology for deployment in upcoming network environments. The ongoing scholarly endeavors are particularly noteworthy in the continual development of optical networks grounded in the principles of Dense Wavelength Division Multiplexing (DWDM) [11][12].

In this thesis, we have addressed the foundational aspects of plasmonics, starting with the fondamentals of Maxwell's equations and the characteristics of surface plasmons, along with a discussion on the selection of metals. The first chapter lays the groundwork. Subsequently, in the second chapter, we delve into light polarization and the diverse applications of plasmonics, exploring their performance, advantages, and disadvantages. The subsequent chapter focuses on modeling techniques, a comparison of various software tools, and the methods employed in fabrication. The concluding chapter is dedicated to presenting the published work, encompassing simulation results and comparisons.

Chapter 1

Plasmonics Fundamentals

1.1 Introduction

Plasmonics is a branch of science that studies and manipulates plasmons, which are collective oscillations of electrons in a material. It includes the interaction of light with surface plasmons, which are collective electron oscillations that occur at the interface of a metal and a dielectric substance. Plasmonics seeks to understand and use plasmons' distinctive optical and electrical capabilities for a variety of applications including nanophotonics, sensing, imaging, energy conversion, and information processing at the nanoscale.

Plasmonics studies the interplay of plasmons and electromagnetic waves by combining concepts from optics, electromagnetism, solid-state physics, and nanotechnology. It implies the design, production, and characterization of plasmonic structures and materials capable of manipulating and controlling light at the nanoscale. Plasmonic devices can circumvent the diffraction limit of traditional optics by utilizing the intense localization and confinement of electromagnetic fields associated with plasmons [13]. Plasmonic structures are often made up of metallic nanostructures supporting surface plasmons, such as nanoparticles, nanowires, nanorods, or thin films. These structures are designed to alter plasmon parameters including frequency, propagation length, and confinement. Researchers can accomplish desired capabilities such as increased light-matter interactions, effective light absorption, and subwavelength imaging by altering the shape, composition, and arrangement of these structures.

Plasmonics has been used in a variety of fields, including biosensing, optical data storage, photovoltaics, catalysis, telecommunications, and quantum optics. The area continues to evolve as researchers investigate new materials, create unique plasmonic structures, and discover new plasmonic phenomena [14]. Plasmonic devices and technologies have the potential to transform a wide range of industries by offering unparalleled control and manipulation

of light at the nanoscale. In this chapter we will give an introduction to the field of plasmonics, their types, the characteristic of plasmonic EM waves and the excitation modes.

1.2 Plasmonics

A fascinating phenomenon called surface plasmons appears at the point of contact between a metal and a dielectric material. They involve the interaction of electromagnetic waves with the collective motion of free electrons on the surface of a conductor [15]. Due to their distinct characteristics and the potential for their use in numerous scientific and technological fields, surface plasmons have garnered a lot of interest. Light can interact with free electrons in metals when it meets with a metal-dielectric contact, resulting in the creation of surface plasmons [16]. These plasmons are basically collective oscillations of the surface electron density, producing a localized electromagnetic field that extends along the contact. The depiction of Surface plasmons with a speed equal to that of light and possessing wavelengths on the order of tens of nanometers as seen in figure 1.1. The ongoing advancement and evolution of chip-scale electronics and photonics has demonstrated remarkable capabilities in data processing and transportation, permeating various facets of contemporary life. Plasmonics, a novel and propitious technology, employs the distinct optical characteristics of metallic nanostructures to facilitate the manipulation and guidance of light at the nanoscale. These plasmonic components possess a small physical footprint and have the ability to operate without any restrictions on bandwidth, which is in stark contrast to the limitations of conventional photonics. However, it is crucial to acknowledge that plasmonic devices do experience significant levels of energy losses [17]. This raises an important question pertaining to the specific domains and scenarios in which plasmonics can introduce a transformative impact.

The development of several plasmonic electro-optical modulators, waveguides, couplers, RF-receivers, and detectors has advanced plasmonic devices. A comprehensive analysis involves a comparative assessment against devices based on the established silicon technology paradigm. Through such examinations, researchers aim to identify the optimal contexts and applications where plasmonics can offer distinct advantages and surpass traditional alternatives. Beyond the diffraction limit of traditional optics, this interaction between light and surface plasmons permits light confinement as well as manipulation at the nanoscale. Surface plasmons are notable for their capacity to concentrate electromagnetic energy into subwavelength volumes [18]. This characteristic has created new opportunities for improving light-matter interactions in areas like sensing, spectroscopy, and nanophotonics. Surface plasmons also have the ability to regulate light propagation and manipula-

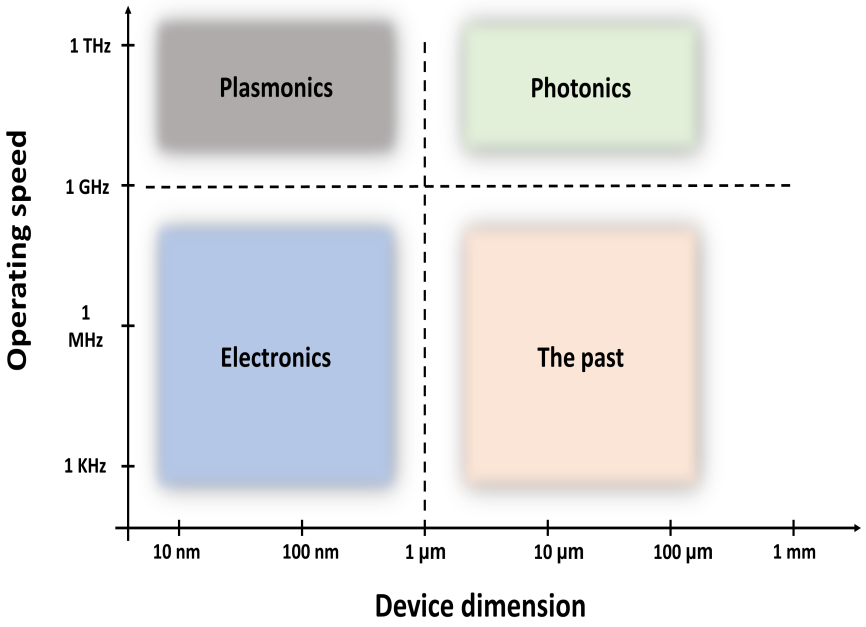

Figure 1.1: Devices operating speeds and sizes of plasmonics and other devices.

tion at the nanoscale, allowing for the construction of new optical devices and circuits. Furthermore, depending on the shape and composition of the metal-dielectric contact, surface plasmons may exhibit fascinating behaviors. These characteristics may be modified by adjusting factors including metal type, thickness, form, and dielectric environment. This tunability enables surface plasmons' properties to be tailored to specific applications, such as plasmonic waveguides, biosensing platforms, photovoltaic systems, and optical data storage.

1.3 Plasmonics' metal properties

The plasmonic characteristics of metals describe the manner in which free electrons in the conduction band of the metal interact with the incoming fields. The collective oscillation of electrons is akin to that of a basic damped harmonic oscillator, wherein the approximation of damping proportionate to the speed of motion by Newton is applicable. Metals, being an extensively researched field of study, are known to typically possess a high density of free electrons. As a result of this peculiar property, it is observed that metals exhibit a higher plasma frequency as compared to other materials, as elucidated by equation (1.1). This intrinsic higher plasma fre-

quency of metals is, in fact, the key feature that renders them an extremely promising material for potential plasmonic applications. It is worthy to note that, for most metals, the plasma frequency spans across a wide range of approximately 100 nm to 1 mm, covering the infrared to ultraviolet range [19].

$$\omega_p = \sqrt{\frac{Nq^2}{m\varepsilon_0}} \tag{1.1}$$

The model developed by Lorentz is frequently utilized to depict the joint oscillation of electrons brought about by an externally applied field, denoted as $\overrightarrow{E}$. The dielectric function for Lorentz model is:

$$\varepsilon(\omega) = 1 + \frac{\omega_p^2}{\omega_0^2 - \omega^2 - i\Gamma\omega} \tag{1.2}$$

with real part:

$$\varepsilon'(\omega) = 1 + \omega_p^2 \frac{\omega_0^2 - \omega^2}{(\omega_0^2 - \omega^2)^2 + \omega^2\Gamma^2} \tag{1.3a}$$

and imaginary part:

$$\varepsilon''(\omega) = \omega_p^2 \frac{\Gamma\omega}{(\omega_0^2 - \omega^2)^2 + \omega^2\Gamma^2} \tag{1.3b}$$

Assuming $\omega_0 = 0$ in the case of metal due to the fundamental nature of the atomic structure, it is widely acknowledged that the majority of electrons are not constrained by the electrostatic attraction of the nucleus, affording them the liberty to roam unencumbered throughout the system. Subsequently, it is feasible for us to procure the Drude model, a theoretical construct, for the metal dielectric function that is explicitly provided in the equation below .

$$\varepsilon(\omega) = 1 - \frac{\omega_p^2}{\omega^2 + i\Gamma\omega} \tag{1.4}$$

with real part:

$$\varepsilon'(\omega) = 1 - \frac{\omega_p^2}{\omega^2 + \Gamma^2} \tag{1.5a}$$

and imaginary part:

$$\varepsilon''(\omega) = \frac{\omega_p^2\Gamma}{\omega(\omega^2 + \Gamma^2)} \tag{1.5b}$$

The imaginary part represents ohmic losses in the metal.

1.3.1 Maxwell's Equations

Maxwell's equations pertaining to plasmonic structures entail the utilization of the same fundamental equations as those presented in classical electromagnetism. However, they are implemented in the context of materials that possess robust electromagnetic interactions, owing to the existence of free electrons, which are commonly referred to as plasmons. When tackling plasmonic structures, it is not uncommon to adapt Maxwell's equations to accommodate the conduct of these collective electron oscillations.

One of the fundamental alterations required pertains to the introduction of supplementary clauses to the constitutive relationships. These clauses delineate the correlation between electric displacement and magnetic field strength with respect to the electric field and magnetic flux density within a given medium. These supplementary clauses are necessary to account for the various interactions that occur between the electromagnetic field and the collective electron oscillations. One potential alteration could be the integration of dispersion effects, which elucidate the manner in which the characteristics of the plasmonic substance fluctuate in correlation with the frequency of the electromagnetic waves. As a result of their resonant conduct at distinct frequencies, plasmonic materials possess the capacity to showcase pronounced dispersion.

Maxwell's equations rely on a quartet of vectors when characterizing the electromagnetic field:

$$\nabla . D = \rho \tag{1.6a}$$

$$\nabla . B = 0 \tag{1.6b}$$

$$\nabla \times E = -\frac{\partial B}{\partial t} \tag{1.6c}$$

$$\nabla \times H = J + \frac{\partial D}{\partial t} \tag{1.6d}$$

where:

- "D" is the dielectric displacement
- "B" is the magnetic flux density
- "E" is electric field
- "H" is electric field
- "ρ" is the external charge
- "J" is the current densities

The interconnection of the four macroscopic fields is established through the mediation of the polarization P and magnetization M by [6]:

$$D = \varepsilon_0 E + P \tag{1.7a}$$

$$H = \frac{1}{\mu_0} B - M \tag{1.7b}$$

In the present discourse, our focus shall be confined to the elucidation of the characteristics exhibited by media that are linear, isotropic, and non-magnetic. Forthwith, it is possible to establish the constitutive relations that define said media as follow [6]:

$$D = \varepsilon_0 \varepsilon_r E \tag{1.8a}$$

$$B = \mu_0 \mu_r H \tag{1.8b}$$

1.3.2 Physical characteristics of SPP

To investigate the physical traits of SPPs, one needs to employ Maxwell's equations 1.6 at the level interface of a conductor and a dielectric.

To add further clarity, it is imperative to note that the equations that govern the guidance of an electromagnetic wave are presented in an extremely exhaustive and all-encompassing manner, covering every conceivable variance and instance of the wave equation. When merging equations 1.6c, 1.6d with no current densities or external charges, we get [6]:

$$\nabla \times \nabla \times E = -\frac{\mu_0 \partial^2 D}{\partial t^2} \tag{1.9}$$

can be written as:

$$\nabla(-\frac{1}{\varepsilon} E.\nabla_\varepsilon) - \nabla^2 E = -\mu_0 \varepsilon_0 \varepsilon \frac{\partial^2 E}{\partial t^2} \tag{1.10}$$

using the identities :

$$\nabla \times \nabla \times E \equiv \nabla(\nabla.E) - \nabla^2 E \tag{1.11a}$$

$$\nabla.(\varepsilon E) \equiv E.\nabla_\varepsilon + \varepsilon \nabla.E \tag{1.11b}$$

$$\nabla.D = 0 \tag{1.11c}$$

For cases in which the dielectric profile, denoted by $\varepsilon = \varepsilon(r)$, remains almost constant over distances that are approximately equivalent to one optical wavelength, it can be considered to exhibit negligible variation, the equation 1.10 simplifies to [6]:

$$\nabla^2 E - \frac{\varepsilon}{c^2}\frac{\partial^2 E}{\partial t^2} = 0 \tag{1.12}$$

In practice, it is imperative to address the task of solving the equation independently in distinct regions characterized by constant ε. Subsequently, the solutions procured from each region need to be harmoniously integrated by employing suitable boundary conditions.

Assuming that all generality a harmonic time dependence of the electric field $E(r,t) = E(r)e^{-i\omega t}$; equation 1.12 will simplified to [6]:

$$\nabla^2 E + k_0^2 \varepsilon E = 0 \tag{1.13}$$

and this equation is known as the Helmholtz equation.

By using $E(x,y,z) = E(z)e^{i\beta x}$ and knowing that $\beta = k_x$ and $k_0 = \frac{\omega}{c}$ as complex parameter of the propagation constant of the traveling waves and corresponds to the component of the wave vector in the direction of propagation and wave vector of the propagating wave in vacuum, equation 1.13 yields the desired form of the wave equation [6]:

$$\frac{\partial^2 E(z)}{\partial z^2} + (k_0^2 \varepsilon - \beta^2)E = 0 \tag{1.14}$$

The equation denoted as 1.14 is the initial step towards the comprehensive examination of guided electromagnetic modes present in waveguides. A meticulous and elaborate discourse on its characteristics and utilities can be perused in [11] and in analogous discussions pertaining to photonics and optoelectronics.

1.4 Plasmons types

Plasmonics refers to the study of many types of plasmons that may be categorised according to their spatial distribution, dispersion characteristics, and the materials involved. The following are some of the most widely investigated plasmonic types.

1.4.1 Surface Plasmon polariton

Surface plasmons are electron oscillations that occur at the interface of two materials as seen in figure 1.2. Under particular conditions, such as the right combination of materials and incident light, are fulfilled, electrons at the interface can be stimulated, resulting in the creation of surface plasmons. These plasmons are distinguished by their capacity to restrict and propagate electromagnetic energy along the interface, providing novel options for nanoscale light manipulation. The strong interaction between the free electrons and the input electromagnetic field causes these excitations,

which result in the creation of surface plasmon polaritons (SPPs). SPPs are defined by their capacity to restrict electromagnetic energy to subwavelength dimensions, allowing for nanoscale light manipulation. The dielectric properties of the materials involved, as well as the geometry and topography of the contact, determine the parameters of SPPs such as dispersion, propagation length, and localization. The SPP wave is a surface-bound EM wave with properties distinct from both free-space light waves and electron oscillations within the bulk of a material. SPPs, unlike regular light waves, are restricted to the interface and decrease exponentially in the perpendicular direction to the interface. The interaction between the free electrons in the metal and the evanescent electromagnetic field that penetrates the dielectric causes this confinement. The propagation length of the SPP wave is determined by several parameters, including the material qualities and the wavelength of the incident light. The energy of the surface plasmon polariton assuming the Drude model is [20]:

$$E_{SPP} = \frac{\hbar\omega_p}{\sqrt{2}}. \tag{1.15}$$

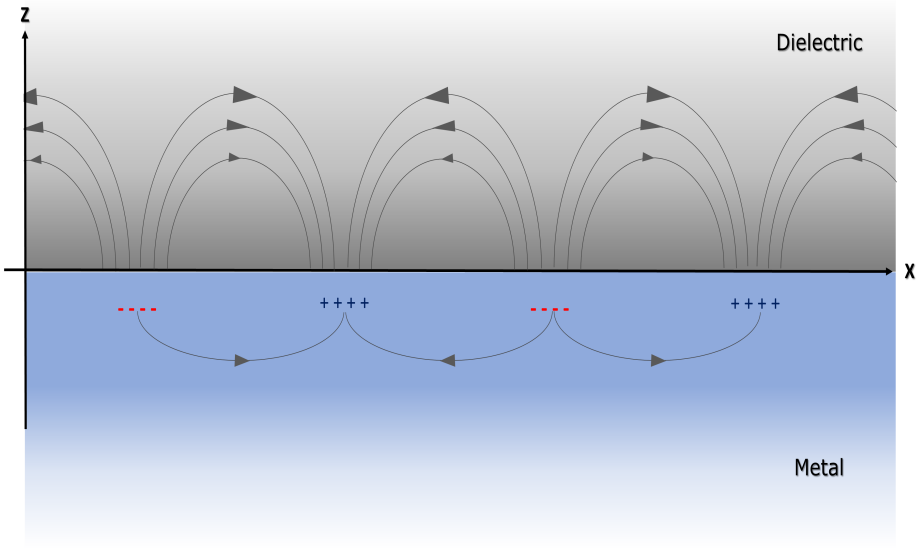

Figure 1.2: Surface plasmon polariton.

1.4.2 Localized surface Plasmons

The collective oscillations of electrons contained to metallic nanoparticles or nanostructures are referred to as localized surface plasmons (LSPs) figure 1.3. LSPs are often activated by incoming light, resulting in significant electromagnetic field amplification surrounding the nanoparticles, allowing for applications such as surface-enhanced spectroscopy and sensing. Consider a metallic nanoparticle, such as gold or silver, with a free electron gas on its surface to better comprehend LSPR. When light interacts with a nanoparticle, the electric field component of the incident light causes the conduction electrons to move. These electrons collectively oscillate, resulting in plasmon resonance. The plasmon resonance frequency is determined by the nanoparticle's size, shape, and composition. The plasmon resonance occurs as an outcome of a strong coupling between the incident light's electric field and the collective electron oscillations. When the frequency of the incident light matches the natural frequency of the plasmon, this coupling is strengthened. As a result, the nanoparticle can absorb and scatter light efficiently at the resonance frequency. The LSPR resonance wavelength is affected by a number of parameters, including the form of the nanoparticle. Spherical nanoparticles, for example, show dipolar LSPR, in which the plasmon oscillations mimic the behavior of a dipole antenna. The Mie theory determines the resonance wavelength for a dipolar mode, which is dependent on the nanoparticle size and refractive index of the surrounding medium. In addition to size and form, the composition of nanoparticles is an important element in defining the parameters of localized surface plasmon resonance (LSPR). Because of differences in their electronic structures, different metals exhibit distinct LSPR features. Gold nanoparticles, for example, often exhibit plasmon resonance in the visible range, whereas silver nanoparticles have a larger resonance that extends into the ultraviolet. LSPR has been extensively researched and used in a variety of domains, including nanophotonics, biosensing, and surface-enhanced spectroscopy. The powerful local electric fields generated by LSPR at the nanoparticle surface improves interactions between light and matter, leading in high sensitivity to changes in the surrounding environment. This sensitivity allows for label-free detection of biological molecules such as proteins and DNA, as well as ultrasensitive chemical sensing via surface-enhanced Raman spectroscopy (SERS).

The energy of a localized surface plasmon at a nano metalic sphere assuming the Drude model is [20]:

$$E_{LSP} = E_{SPP} = \frac{\hbar\omega_p}{\sqrt{3}}. \tag{1.16}$$

1.4.3 Bulk Plasmons

Bulk plasmons, also known as volume plasmons, are collective electron

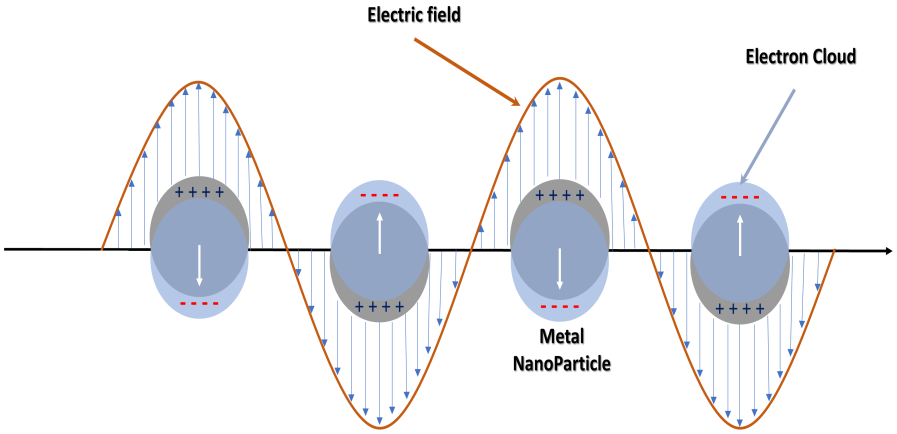

Figure 1.3: Localized surface plasmon.

oscillations that occur in a conducting material's bulk as depicted in figure 1.4. They do not involve a contact, as opposed to surface plasmons, but rather the complete material. Bulk plasmons are often stimulated at longer wavelengths, and their characteristics are determined by the material's electrical structure. To better understand the idea, Consider a simple model of a metal with a homogenous electron gas. The metal's valence electrons can be modeled in this model as a free electron gas that travels independently of the ionic lattice. An external electric field supplied to the metal interacts with the electrons, causing them to oscillate collectively. The behavior of bulk plasmons is determined by the material's dielectric characteristics. The plasma frequency in metals, where the real part of the dielectric function is negative, is in the visible or ultraviolet range, resulting in considerable absorption and reflection of light at those frequencies. This effect is responsible for metals' reflecting qualities and the appearance of metallic sheen. Bulk plasmon theory has found widespread use in domains such as condensed matter physics, nanoscience, and plasmonics. It sheds light on metal optical characteristics, electron behavior in solids, and light interaction with nanostructured materials. Understanding and regulating bulk plasmons allows for the development of innovative optical devices including plasmonic sensors, waveguides, and improved spectroscopies.

The energy of the plasmon [20]:

$$E_{bulk} = \hbar\omega_p. \tag{1.17}$$

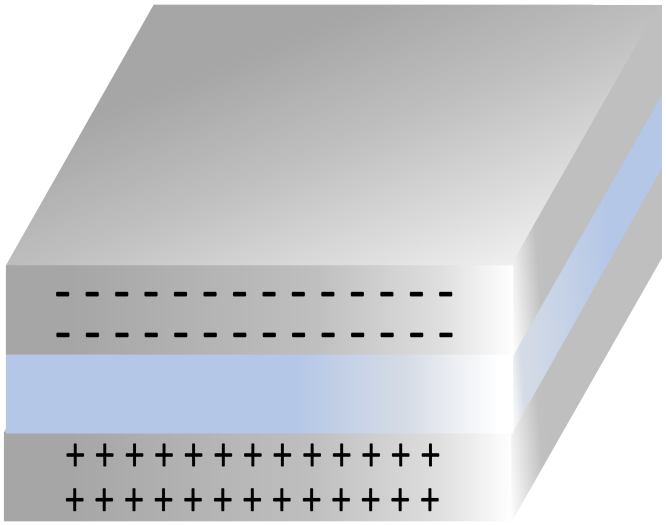

Figure 1.4: Bulk plasmon.

These are only a few examples of plasmonic types, and the area of plasmonics is constantly evolving as new materials, structures, and phenomena are discovered. The precise type of plasmon examined and used is determined by the desired application and the features necessary for the plasmonic device or system to work.

1.5 Surface plasmon polaritons characteristics

Surface plasmon polaritons (SPPs) have three key characteristics that influence their behavior and applications: the evanescent field in the dielectric, the evanescent field in the metal, and the propagation length as depicted in figure1.5. These parameters work together to give SPPs their distinct properties and increased light-matter interactions.

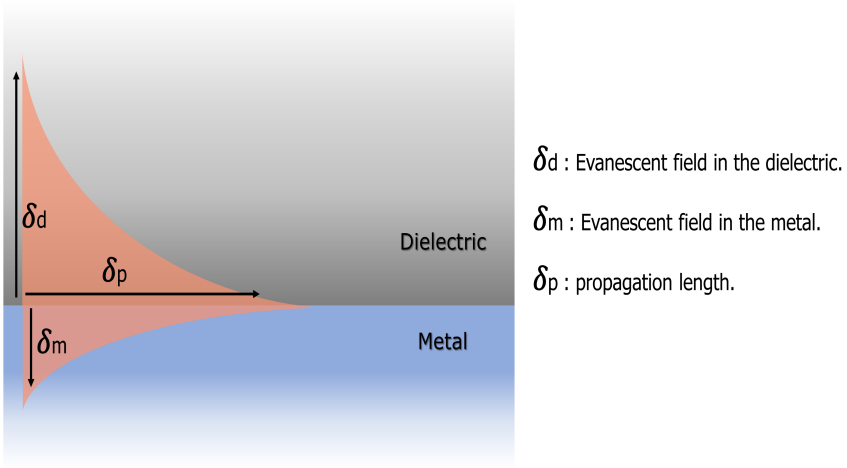

Figure 1.5: Surface plasmon characteristics.

1.5.1 Evanescent field in the dielectric

When SPPs are stimulated at the metal-dielectric interface, the electromagnetic field that extends into the adjacent dielectric material is referred to as the evanescent field in the dielectric. This evanescent field decays exponentially away from the interface, restricting the SPP energy near the interface. This confinement generates a highly confined and strong electromagnetic field, allowing for efficient interaction with adjacent objects like molecules or nanoparticles. This characteristic is used in a variety of applications, including surface-enhanced spectroscopies, in which the evanescent field amplifies the signal from analytes close to the interface.

The evanescent filed in the dielectric can be defined using the equation (1.18).

$$E_d = \frac{\lambda}{2\pi} \left(\frac{| \varepsilon_m^{'} + \varepsilon_d |}{\varepsilon_d^2} \right)^{1/2} \tag{1.18}$$

1.5.2 Evanescent field in the metal

Similarly, the interaction between the SPP wave and the metal's free electrons produces the evanescent field. This field penetrates the metal and exponentially decays away from the interface. The evanescent field in the metal is responsible for energy absorption and dissipation, resulting in atten-

uation of the SPP wave as it propagates along the contact. The evanescent field in the metal effects SPP propagation length, which is the distance an SPP wave can travel before its energy is severely dampened. Improving propagation length is an important problem in SPP-based applications, and it can be accomplished through careful material selection, optimal interface design, and the introduction of plasmonic nanostructures. The evanescent field in the metal can be described using the equation 1.19.

$$E_m = \frac{\lambda}{2\pi} \left(\frac{\mid \varepsilon_m^{'} + \varepsilon_d \mid}{\varepsilon_m^{'\,2}} \right)^{1/2} \tag{1.19}$$

1.5.3 Propagation length

The propagation length represents the distance over which the SPP wave can travel along the metal-dielectric interface before its energy significantly attenuates to $1/e$. A long propagation length is advantageous because it allows the SPP wave to travel over greater distances, allowing for more efficient information or energy transmission. Achieving a long propagation length is critical for SPP-based applications requiring low-loss propagation, such as plasmonic waveguides or interconnects. SPP propagation duration is determined by the balance of energy loss mechanisms like as absorption and scattering, as well as energy confinement at the interface. Materials having lower absorption and scattering losses, as well as higher field confinement, have longer propagation lengths in general. Researchers use a variety of ways to increase the propagation length of SPPs. These include choosing materials with low intrinsic losses, improving the quality of the dielectric-metal interface, and designing plasmonic structures that enable efficient energy confinement while minimizing energy dissipation. Surface roughness and flaws can also affect propagation length by introducing scattering or leakage loss; Hence, Researchers can overcome restrictions associated with conventional optical devices and leverage the unique features of SPPs for advanced nanophotonic applications by expanding the distance over which SPPs can travel with minimum energy loss. The propagation length is determine by equation (1.20)

$$L_{spp} = \frac{1}{2\kappa_{spp}^{''}} = \frac{\varepsilon_m^{'\,2}}{\kappa_0 \varepsilon_m^{''}} \left(\frac{\varepsilon_m^{'} + \varepsilon_d}{\varepsilon_m^{'} \varepsilon_d} \right)^{3/2} \tag{1.20}$$

In summary, the evanescent fields in the dielectric and metal, as well as the propagation length, are critical characteristics that dictate the behavior of SPPs. Understanding and exploiting these parameters paves the door for the creation of game-changing technologies that take use of the increased light-matter interactions and subwavelength confinement provided by SPPs.

1.6 Surface Plasmon waves (SPWs) characteristics

The electromagnetic (EM) waves associated with surface plasmons have several distinct characteristics that differentiate them from conventional electromagnetic waves. Here are some essential properties of surface plasmon EM waves:

1.6.1 Subwavelength confinement

Surface plasmon waves (SPWs) exhibit an exceptional capability to confine electromagnetic energy to areas that are smaller than the diffraction limit of standard optics. This confinement is accomplished through the interaction between the propagating SPW and the metal-dielectric interface. By capitalizing on this property, SPWs facilitate the manipulation and management of light at the nanoscale, thereby transforming applications in nanophotonics, subwavelength imaging, and sensing. Researchers can surmount the limitations of conventional optics by utilizing SPWs, thus achieving superior resolution and sensitivity in nanoscale imaging and sensing applications. The subwavelength confinement of SPWs offers intriguing prospects for examining and exploiting light-matter interactions at the tiniest scales, thereby paving the way for unparalleled advancements in various scientific and technological domains.

1.6.2 Strong field enhancement

Surface plasmon waves (SPWs) significantly increase the electric field at the metal-dielectric contact. This enhancement is caused by the interaction of the SPW and the incident light, which results in a concentration of electromagnetic energy near the interface. The electric field associated with SPWs can be considerably increased, especially at sharp features such as nanoscale tips or gaps. This characteristic allows for improved light-matter interactions, making SPWs useful in applications such as surface-enhanced spectroscopy, where the amplified field amplifies the signal of molecules in close proximity to the metal surface. Additionally, the intensified field of SPWs finds utility in sensing applications, allowing for highly sensitive detection of analytes. Moreover, SPWs play a crucial role in nonlinear optics, as the amplified field facilitates nonlinear optical phenomena at the nanoscale, enabling the manipulation of light for various technological advancements.

1.6.3 Localized field distribution

Surface plasmon waves (SPWs) create electromagnetic fields that are tightly confined near the metal-dielectric contact, typically within a few

nanometers of the surface. This exceptional localization capability allows for precise manipulation and control of light at the nanoscale, enabling interactions with nearby objects or molecules. This confined field region enhances sensitivity in sensing applications, making SPWs valuable for detecting even small changes in the environment. Moreover, the localized electric fields generated by SPWs exponentially decay away from the interface, resulting in a highly concentrated and intensified region of field strength. This localization facilitates accurate control over light-matter interactions on the nanoscale. For instance, in surface-enhanced Raman spectroscopy (SERS), molecules situated on the metal surface experience highly intense fields, resulting in enhanced Raman scattering signals. Overall, the ability of SPWs to confine electromagnetic fields near the metal-dielectric interface empowers nanoscale light manipulation, boosts sensing capabilities, and facilitates efficient energy transfer in plasmonic devices..

1.6.4 Dispersion relation

Likewise, surface plasmon waves (SPWs) possess an inherent dispersion relation that governs their propagation. The dispersion relation delineates the correlation between the wavevector, which reflects the momentum of the SPW, and its associated frequency. This correlation is contingent on attributes such as the dielectric constant of the proximal medium and the magnitude of the dielectric layer.

The dispersion relation of SPWs is especially responsive to the parameters of the metal-dielectric interface. Minute variations in factors such as the dielectric constant or the thickness of the dielectric layer can substantially influence the excitation conditions, propagation length, and frequency response of SPWs.

Understanding and controlling the dispersion relation of SPWs is essential for optimizing their behavior in various applications. It allows for precise control over the wavelength, propagation length, and mode confinement of SPWs, enabling tailored and efficient manipulation of light at the nanoscale.

1.6.5 Strong absorption and scattering

Surface plasmons and SPWs possess the remarkable ability to absorb and scatter incoming light, making them valuable in various applications. The absorption of energy from incident light occurs due to the resonant interaction between the electromagnetic field and the collective electron oscillations in the metal. This absorption phenomenon finds utility in photodetection, photothermal treatment, and light harvesting.

Moreover, SPWs can induce strong absorption and scattering of incident light through their interaction with the surrounding dielectric medium. The absorption and scattering characteristics of SPWs are influenced by several

factors, including the wavelength of the incident light, the material properties of the metal, and the conditions at the interface.

For instance, plasmonic nanostructures like nanorods or nanospheres exhibit strong absorption or scattering effects upon exciting SPWs. These effects have significant implications in diverse fields such as solar cells, photothermal therapy, and optical sensors. In solar cells, SPWs enhance light absorption, enabling more efficient conversion of sunlight into usable energy. In photothermal therapy, SPWs contribute to targeted heating of tissues, providing a promising avenue for cancer treatment. Additionally, in optical sensors, SPWs play a crucial role in achieving ultra-sensitive detection through enhanced light-matter interactions.

1.6.6 Sensitivity to interface conditions

Surface plasmon characteristics exhibit extreme sensitivity to the metal-dielectric interaction, with properties such as resonance wavelength, field enhancement, and propagation length being significantly influenced by several factors. Metal selection plays a crucial role, as different metals possess distinct plasmonic behaviors due to variations in electron density, band structure, and energy loss mechanisms. Noble metals like gold and silver are commonly preferred for their strong plasmonic responses in the visible and near-infrared regions. The dielectric material adjacent to the metal also affects plasmonic interactions, with the refractive index of the dielectric influencing the resonance wavelength. By choosing different dielectric materials, the plasmonic response can be tailored to specific applications and wavelengths. Additionally, interface roughness at the metal-dielectric interface can have a substantial impact, as surface irregularities scatter plasmons and increase energy loss, affecting propagation length and field enhancement. Minimizing interface roughness is essential for optimizing plasmonic performance. Furthermore, the dielectric constant of the surrounding medium significantly influences resonance conditions and field enhancement. Changes in the dielectric constant alter the effective refractive index experienced by the plasmonic field, thereby affecting the resonance wavelength and mode confinement. Through manipulation of the dielectric constant, it is possible to precisely adjust the plasmonic properties to fulfill the specific needs of designed applications. The plasmonic resonance is easily influenced by a variety of factors, such as the choice of metal, the dielectric material, the roughness of the interface, and the dielectric constant, thus allowing for the customization and optimization of plasmonic devices and structures to meet the demands of specific applications.

Overall, the electromagnetic waves associated with surface plasmons exhibit unique properties, such as subwavelength confinement, strong field enhancement, and sensitivity to interface conditions.

1.7 The metal choise

The choice of metal plays a significant role in surface plasmon polariton (SPP) phenomena and their applications. Different metals have distinct optical and plasmonic characteristics that influence the behavior of SPPs at the metal-dielectric contact. The permittivity, conductivity, and surface roughness of a metal can all have a major impact on the excitation, propagation, and confinement of SPP waves. Gold (Au), silver (Ag), and aluminum (Al) are common metals used in plasmonic. Gold is frequently preferred because of its excellent plasmonic qualities in the visible and near-infrared spectral ranges, such as its low losses and strong interaction with light. Silver has stronger plasmonic effects than gold, especially in the visible range, but it is more prone to oxidation and has higher losses. Aluminum, on the other hand, has plasmonic capabilities in the ultraviolet to visible range and, due to its low cost and compatibility with complementary metal-oxide-semiconductor (CMOS) technology, can be an appealing alternative for some applications. The appropriate metal is chosen based on the application's specific requirements. Gold or silver, for example, may be favoured for low-loss propagation over long distances due to their superior plasmonic characteristics and reduced intrinsic losses. Aluminum, on the other hand, may be a good option if cost-effectiveness or compatibility with specific production procedures is a priority. It is worth mentioning that the choice of metal also influences other SPP parameters, such as the resonance wavelength, field confinement, and energy dissipation. The optical properties of metals can be accurately described by models such as the Drude or Drude-Lorentz models, which take into account the metal's permittivity and conductivity as a function of frequency figure 1.6. If a substance possesses these two properties, we will categorize it as a good plasmonic metal.

$$Re\varepsilon_m < 0, Im << -Re\varepsilon_m. \tag{1.21}$$

The quality factor is another crucial parameter that influences the selection of the metal. It determines the number of optical periods required for the field to decay, thereby affecting the frequency of free surface plasmon oscillations. The quality factor can be define using the equation [22]:

$$Q = \frac{\omega}{2\gamma} \approx \frac{\omega \frac{\partial Re\varepsilon_m(\omega)}{\partial(\omega)}}{2Im\varepsilon_m(\omega)}. \tag{1.22}$$

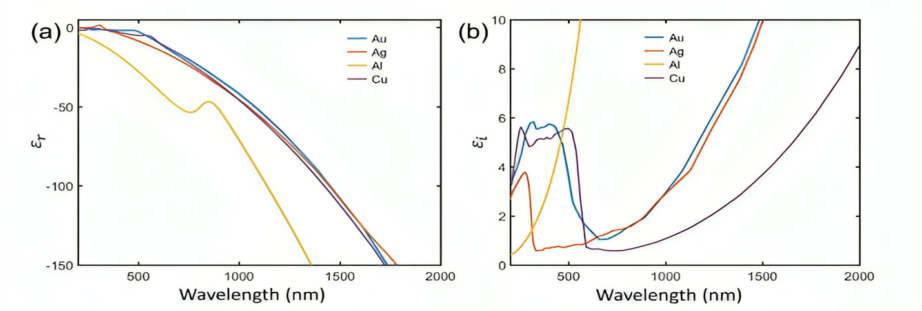

Figure 1.6: (a) Real and (b) imaginary parts of permittivity as a function of wavelength for Au, Ag, Al, and Cu as obtained experimentally [21].

It is worth noting that another popular definition of the quality factor is

$$Q = \frac{-Re\varepsilon_m(\omega)}{Im\varepsilon_m(\omega)}. \tag{1.23}$$

The SP quality factors Q calculated according to equation (1.22) and equation (1.23) are shown in figure 1.7.

The transitions occurring between energy bands are acquired from electrons that possess lower energy compared to those that are free, and their effect can only be significantly observed when the incident energy is at an elevated level.

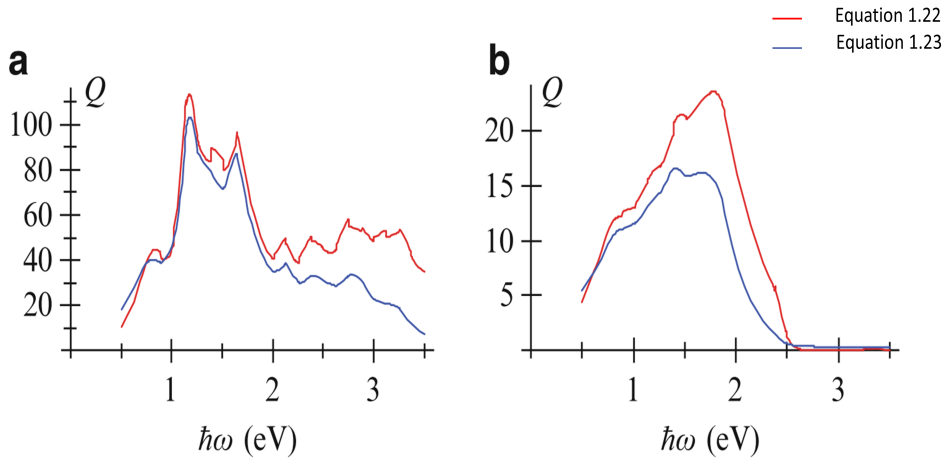

Figure 1.7: Quality factor for (a) silver and (b) gold as a function of ω [22].

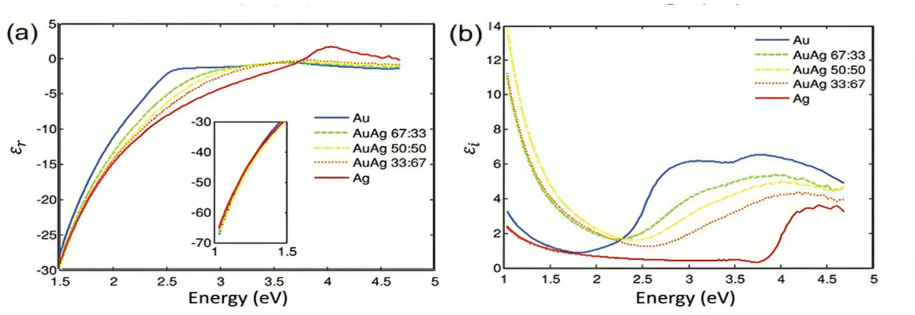

Figure 1.8: (a)Real and (b) imaginary part of dielectric constants of Au, Ag, and Au/Ag as a function of energy [21].

It's quite unimpressive that inter-band transition energies, like 3.9 eV for Ag, 2.4 eV for Au, and 2.1 eV for Cu, cannot realistically be achieved figure 1.8 [21].

1.8 Surface Plasmons excitation types

The technique for stimulating Surface Plasmon Polaritons (SPP) through the utilization of free propagating Electromagnetic (EM) waves that move through a dielectric medium demands the attainment of momentum consistency between the incident EM wave and ($Kspp$). However, it is paramount to acknowledge that the instant ($Kspp$) of SPP is consistently greater than that of light in unrestricted space $Kspp$ for the same frequency w. This arises from the fact that the scattering curve of SPPs is persistently located on the right-hand side of the scattering curve of the dielectric light line as illutrated in figure 1.9. As a result of this momentum disparity, SPPs are unable to radiate effortlessly into free-space, thus highlighting their bound or non-radiative nature. This characteristic is highly desirable for the purpose of transmitting or guiding SPP waves through plasmonic components.

SPPs are readily excited at a frequency of :

$$\omega_{spp} = \frac{\omega_p}{\sqrt{1+\varepsilon_d}} \tag{1.24}$$

under the condition:

$$\varepsilon_d + \varepsilon_m = 0 \tag{1.25}$$

in order to overcome the mismatch between the metal and the dielectric.

Surface plasmons can be stimulated in a variety of ways and combinations. Here are some examples of surface plasmon excitation methods that are regularly used.

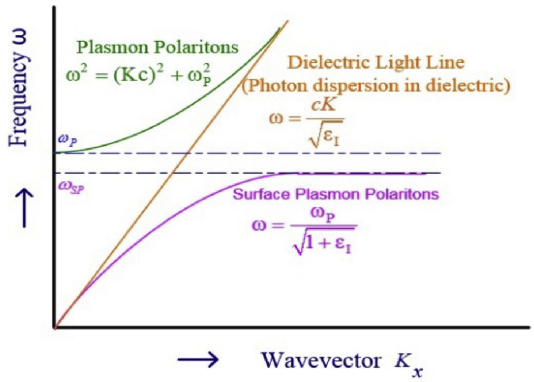

Figure 1.9: SPPs Dispersion curve on metal-dielectric interface [23].

1.8.1 Prism coupling

Surface plasmon polaritons on a flat metal/dielectric interface cannot be directly excited by light beams due to the fact that $\beta > k$, where k represents the wave vector of light on the dielectric side of the interface. Consequently, the projection along the interface of the momentum k of photons impinging under an angle θ to the surface normal is always smaller than the propagation constant θ of SPP, even at grazing incidence, which prohibits phase-matching. There are two configurations of prism coupling: the Kretschmann configuration and the Otto configuration.

Kretschmann configuration

The Kretschmann configuration, which was developed by R. Kretschmann, represents a widely utilized prism coupling technique recognized as attenuated total reflection (ATR) for the purpose of exciting surface plasmons. This configuration entails the placement of a narrow metallic layer, typically made up of gold or silver, directly onto a dielectric substrate's surface, such as glass or a prism. Through the guidance of darkness onto the prism at an unspecific angle, designated as the angle of partial external reflection, the incident light separates from surface plasmons at the metal-dielectric interface. The Kretschmann configuration enjoys significant popularity in surface plasmon resonance (SPR)-based biosensing and surface analysis applications, given its capacity to enable the detection of changes in the refractive index of the surrounding medium by monitoring the resonance condition. This configuration offers enhanced sensitivity and has proven to be an effective method for studying plasmonic phenomena and interactions with the surrounding environment.

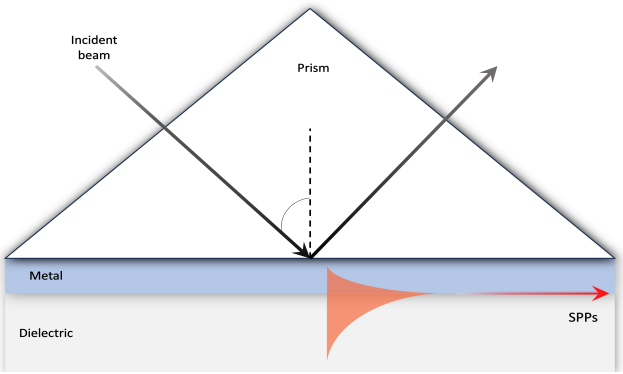

Figure 1.10: Kretschmann configuration.

Otto configuration

The Otto arrangement, originally described by A. Otto, involves the insertion of a slim metallic sheet between two dielectric layers, and the placement of a prism with a higher refractive index on the topmost part of the metal layer. By manipulating the polarization and angle of incidence of incoming light, it can be coupled into surface plasmons. This setup provides greater adaptability in regulating the excitation conditions, making it widely utilized in spectroscopic research and sensing applications. The incident light on the prism generates an evanescent field that expands into the metal film via multiple reflections, thus stimulating surface plasmons. The Otto configuration is especially useful in exploring plasmonic characteristics and surface sensing applications, enabling extensive research into the actions and connections of surface plasmons.

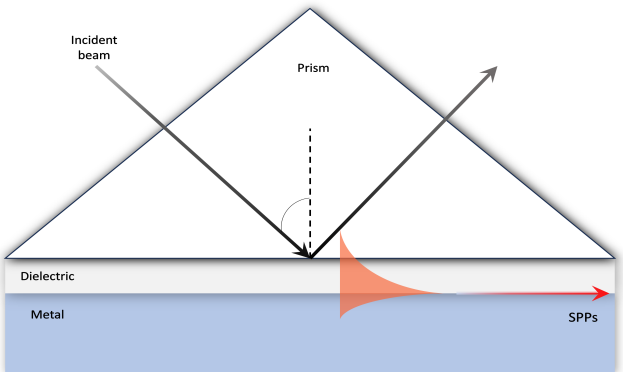

Figure 1.11: Otto configuration.

1.8.2 Grating-coupled excitation

Grating-coupled excitation is a fascinating technique that efficiently connects incident light with surface plasmons in plasmonic structures using a diffraction grating. The periodic structure of the grating introduces fluctuations in the refractive index, enabling effective coupling of specific light wavelengths to the desired surface plasmon mode. This approach offers precise control over the excitation conditions and finds applications in fields such as sensing and spectroscopy. The interaction between the incident light and the diffraction grating generates distinct diffraction orders, with the grating-coupled order being responsible for coupling energy to the surface plasmon mode. The efficiency of this coupling and the resonant wavelength depend on the grating's period, which can be adjusted by modifying the incident angle or altering the grating's characteristics. This technique's simplicity, tunability, and broad wavelength range coupling make it highly valuable for plasmonic research, facilitating device design and the exploration of various plasmonic resonances.

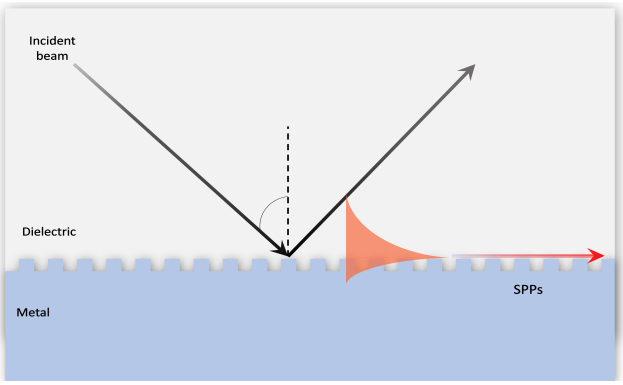

Figure 1.12: Diffraction grating.

1.8.3 Near-field optical microscopy

The excitation of surface plasmon polaritons (SPPs) using near-field techniques necessitates the usage of a localized electromagnetic field to interact with the SPP mode on a metal-dielectric interface. Near-field techniques allow for the manipulation and control of light at subwavelength scales, enabling efficient coupling of light to SPPs. To comprehend the activation process, let us consider a customary configuration in which a metal film is positioned at the base of a dielectric material. The metal film can uphold SPP modes. These SPP modes can be stimulated by incident light. Nearby-field methods use the evanescent light field, which can transmit light beyond the diffraction limit. Although this evanescent field rapidly decays away from the source, it poses a challenge in terms of directly coupling with

the SPPs. Nevertheless, with the introduction of a subwavelength-sized probe or antenna in close proximity to the metal-dielectric interface, the evanescent field can be amplified and effectively coupled to the SPP mode.

One commonly used technique is called aperture-based excitation figure 1.13(a). It implies placing a small aperture, such as a subwavelength-sized hole or a sharp tip wish is mush smaller than the wavelength, in close proximity to the metal surface by 50 to 100 nm. When light is incident on the aperture, the evanescent field leaks through the aperture and interacts with the metal surface, generating SPPs.

Another approach involves the implementation of plasmonic nanostructures, particularly nanoparticles or nanowires, which serve as proficient antennas for light-SPP coupling figure 1.13(b). These nanostructures possess localized surface plasmon resonances that can be adjusted to correspond with the energy of the SPP mode, but when light is introduced, the localized surface plasmon resonance stimulates the SPP mode, which results in the propagation of SPPs along the metal-dielectric interface.

Both times, the efficient excitation of SPPs is made possible by the near-field approaches, which rely on the improved interaction between the evanescent field and the SPP mode. These techniques enable the manipulation and control of light at the nanoscale and have extensive applications in plasmonics, nanophotonics, and surface-enhanced spectroscopies.

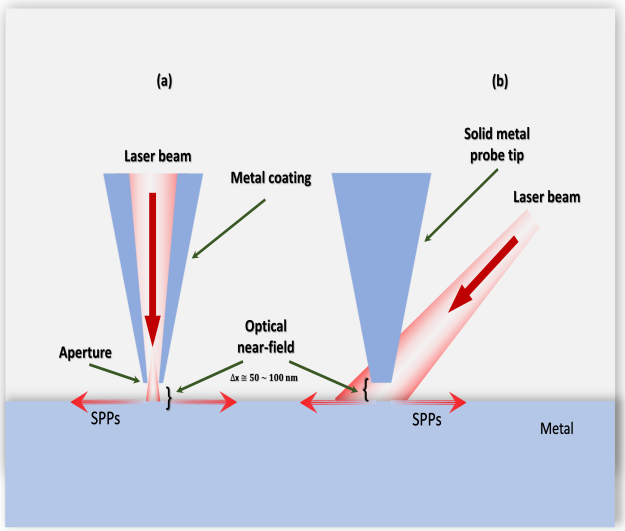

Figure 1.13: Near-Field optical microscopy (a) aperture, (b) aperture-less, excitation of SPPs.

1.9 Conclusion

Plasmonics is a fast expanding area that investigates the distinct features and uses of surface plasmons. The capacity of surface plasmons to restrict and alter light at the nanoscale offers up new possibilities in sensing, imaging, energy conversion, and information processing. Surface plasmon excitation modes including the Kretschmann configuration, grating coupling, scanning near-field microscopy, and the Otto configuration provide a variety of approaches for harnessing and manipulating these collective electron oscillations. Surface plasmons' significant field enhancement, subwavelength confinement, and sensitivity to interface conditions open up new opportunities for enhancing nanophotonics and building high-performance plasmonic devices. As novel phenomena and materials are discovered, plasmonics has immense potential for changing technology and offering unprecedented control over light-matter interactions at the nanoscale.

Chapter 2

Light Polarization and Plasmonic Applications

2.1 Introduction

The polarization of light, an inherent characteristic of electromagnetic waves, holds a pivotal position in a myriad of optical phenomena and technological progressions. Its manipulative prowess has significantly broadened the horizons within the domain of photonics and plasmonics, paving the way for innovative device creation and diverse applications. Plasmonic waveguides, exploiting the coordinated oscillations of electrons on metal surfaces, stand as a highly promising framework for guiding and modulating light at an unprecedented nanoscale. The convergence of light polarization control with plasmonic waveguides presents distinctive prospects in augmenting interactions between light and matter, and precisely tailoring light attributes at the sub-microscopic scale. Throughout this chapter, we embark on an exploration encompassing the essence of light polarization, the fundamental tenets of plasmonic waveguides, and their symbiotic applications. Our objective is to elucidate the immense potential of this interdisciplinary sphere in reshaping contemporary optical technologies.

2.2 Polarization of incident light

In the alluring realm of plasmonics, a discipline dedicated to exploring the behavior of light at the nanoscale, two distinctive polarization modes have emerged as prominent: TE and TM. These modes serve as crucial players in shaping the manner in which light interacts with metal surfaces and nanostructures, presenting unparalleled prospects for the manipulation and amplification of light-matter interactions.

2.2.1 TE-polarization

TE polarization in plasmonics is characterized by the oscillation of the electric field (E-field) parallel to the metal's surface, In the meantime, the magnetic field (H-field) is aligned perpendicular to the surface. TE polarization typically cannot excite surface plasmons because it lacks an electric field component along the direction of propagation.

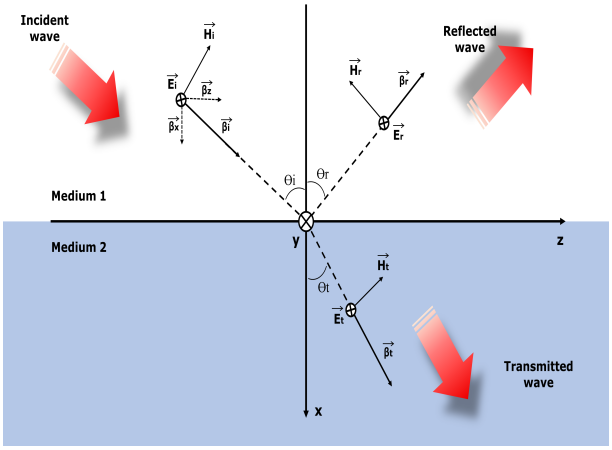

Figure 2.1: TE polarization.

2.2.2 TM-polarization

On the opposite, whilst taking into account TM polarization, the E-field experiences oscillations perpendicular to the metal surface, whereas the H-field experiences oscillations parallel to the metal surface. In the realm of plasmonic devices, it is of utmost importance to utilize TM polarization as it enables incident light to efficiently couple to surface plasmons. In practical terms, TM polarization manifests itself in plasmonic waveguides, nanoscale antennas, and sensors where the ability to concentrate and manage light at the nanoscale is indispensable.

2.3 Existence of SPP in which mode

In the pursuit of utilizing the wave equation as a tool for ascertaining the spatial field profile and dispersion of propagating waves, it becomes incumbent upon us to procure explicit expressions for the various field components of electric and magnetic fields, denoted by E and H, respectively.

For the purpose of analyzing harmonic time dependence($\frac{\partial}{\partial t} = -i\omega$), we are led to the derivation of the ensuing set of coupled equations [6].

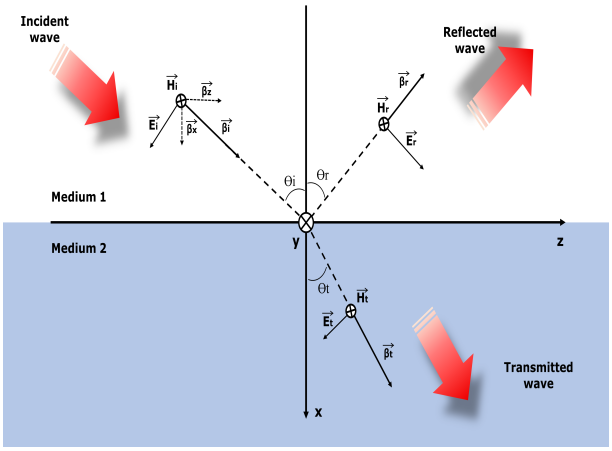

Figure 2.2: TM polarization.

$$\frac{\partial E_z}{\partial y} - \frac{\partial E_y}{\partial z} = i\omega\mu_0 H_x \tag{2.1a}$$

$$\frac{\partial E_x}{\partial z} - \frac{\partial E_z}{\partial x} = i\omega\mu_0 H_y \tag{2.1b}$$

$$\frac{\partial E_y}{\partial x} - \frac{\partial E_x}{\partial y} = i\omega\mu_0 H_z \tag{2.1c}$$

$$\frac{\partial H_z}{\partial y} - \frac{\partial H_y}{\partial z} = -i\omega\varepsilon_0\varepsilon E_x \tag{2.1d}$$

$$\frac{\partial H_x}{\partial z} - \frac{\partial H_z}{\partial x} = -i\omega\varepsilon_0\varepsilon E_y \tag{2.1e}$$

$$\frac{\partial H_y}{\partial x} - \frac{\partial H_x}{\partial y} = -i\omega\varepsilon_0\varepsilon E_z. \tag{2.1f}$$

this equation is simplifies to:

$$\frac{\partial E_y}{\partial z} = -i\omega\mu_0 H_x \tag{2.2a}$$

$$\frac{\partial E_x}{\partial z} - i\beta E_z = i\omega\mu_0 H_y \tag{2.2b}$$

$$i\beta E_y = i\omega\mu_0 H_z \tag{2.2c}$$

$$\frac{\partial H_y}{\partial z} = i\omega\varepsilon_0\varepsilon E_x \tag{2.2d}$$

$$\frac{\partial H_x}{\partial z} - i\beta H_z = -i\omega\varepsilon_0\varepsilon E_y \tag{2.2e}$$

$$i\beta H_y = -i\omega\varepsilon_0\varepsilon E_z. \tag{2.2f}$$

for ($\frac{\partial}{\partial_x} = i\beta$) i.e the propagation is along the X-direction as seen in figure 2.3 and homogeneity in the y-direction ($\frac{\partial}{\partial_y} = 0$).

For transverse magnetic (TM) modes, it can be observed that the system of governing equations 2.2 can be simplified to the expression of :

$$E_x = -i\frac{1}{\omega\varepsilon_0\varepsilon}\frac{\partial H_y}{\partial_z} \tag{2.3a}$$

$$E_z = -\frac{\beta}{\omega\varepsilon_0\varepsilon}H_y \tag{2.3b}$$

and the wave equation for TM modes is

$$\frac{\partial^2 H_y}{\partial z^2} + (k_0^2\varepsilon - \beta^2)H_y = 0. \tag{2.3c}$$

For transverse electric (TE) modes, the equation reduces to:

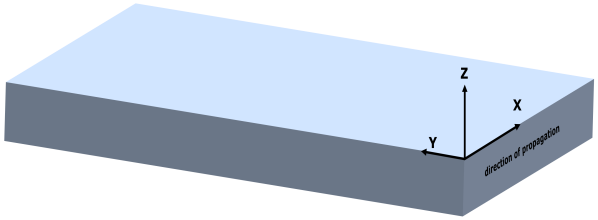

Figure 2.3: Planar waveguide geometry.

$$H_x = i\frac{1}{\omega\mu_0}\frac{\partial E_y}{\partial_z} \tag{2.4a}$$

$$H_z = \frac{\beta}{\omega\mu_0}E_y \tag{2.4b}$$

and the wave equation for TE modes is

$$\frac{\partial^2 E_y}{\partial z^2} + (k_0^2\varepsilon - \beta^2)E_y = 0. \tag{2.4c}$$

With the mathematical equations that have been made available to us, we have now attained the necessary means to commence our elucidation of surface plasmon polaritons existence modes.

Using the equation 2.3 considering a metallic character which implies that $R_e[\varepsilon_1] < 0$, the equation yields [6]:

for $z > 0$

$$H_y(z) = A_2 e^{i\beta x}e^{-k_2 z} \tag{2.5a}$$

$$E_x(z) = iA_2\frac{1}{\omega\varepsilon_0\varepsilon_2}k_2 e^{i\beta x}e^{-k_2 z} \tag{2.5b}$$

$$E_z(z) = -A_1\frac{\beta}{\omega\varepsilon_0\varepsilon_2}k_2 e^{i\beta x}e^{-k_2 z} \tag{2.5c}$$

for $z < 0$

$$H_y(z) = A_1 e^{i\beta x}e^{k_1 z} \tag{2.6a}$$

$$E_x(z) = -iA_1\frac{1}{\omega\varepsilon_0\varepsilon_1}k_1 e^{i\beta x}e^{k_1 z} \tag{2.6b}$$

$$E_z(z) = -A_1\frac{\beta}{\omega\varepsilon_0\varepsilon_2}e^{i\beta x}e^{k_1 z} \tag{2.6c}$$

Where A_1 and A_2 are the amplitude of magnetic and electric fields in the dielectric and metal, respectively. For $z < 0$, $k_i \equiv k_{z,i}(i = 1, 2)$ is the wave vector's component vertical to the two media's. $z = 1/|k_z|$, pertains to the evanescent decay length of the fields which are oriented perpendicular to the interface. Continuity of H_z and $\varepsilon_i E_z$ requires that $A1 = A2$ and

$$\frac{k_2}{k_2} = -\frac{\varepsilon_2}{\varepsilon_1}. \tag{2.7}$$

Combining $k_1^2 = \beta^2 - k_0^2\varepsilon_1$ and $k_2^2 = \beta^2 - k_0^2\varepsilon_2$ with equation 2.7 gives the dispersion relation of SPP:

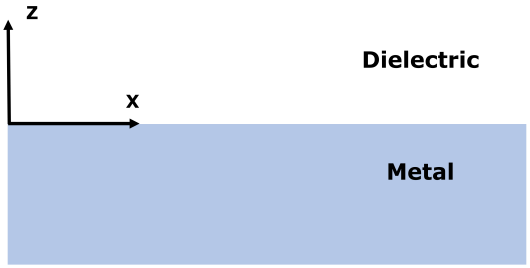

Figure 2.4: Single interface SPP propagation Geometry.

$$\beta = k_0 \sqrt{\frac{\varepsilon_1 \varepsilon_2}{\varepsilon_1 + \varepsilon_2}} \tag{2.8}$$

Using equation 2.4 yielding:
for $z > 0$

$$E_y(z) = A_2 e^{i\beta x} e^{-k_2 z} \tag{2.9a}$$

$$H_x(z) = -iA_2 \frac{1}{\omega \mu_0} k_2 e^{i\beta x} e^{-k_2 z} \tag{2.9b}$$

$$H_z(z) = A_2 \frac{\beta}{\omega \mu_0} e^{i\beta x} e^{-k_2 z} \tag{2.9c}$$

for $z < 0$

$$E_y(z) = A_1 e^{i\beta x} e^{k_1 z} \tag{2.10a}$$

$$H_x(z) = iA_1 \frac{1}{\omega \mu_0} k_1 e^{i\beta x} e^{k_1 z} \tag{2.10b}$$

$$H_z(z) = A_1 \frac{\beta}{\omega \mu_0} e^{i\beta x} e^{k_1 z} \tag{2.10c}$$

The continuity of E_y and H_x leads to $A1(k_1 + k_2) = 0$ and the fulfillment of the condition for confinement to the surface necessitates $Re[k_1] > 0$ and $Re[k_2] > 0$. It is notable that this condition is solely satisfied in the event of A_1 being equivalent to 0, thereby leading to $A_2 = A_1 = 0$ as well. Accordingly, it can be deduced that the absence of surface modes is a characteristic feature of TE polarization [6]. Thus, *Surface plasmon polaritons only exist for TM polarization* as depicted in figure 2.5.

2.4 Plasmonic waveguides

The transmission of data over short distances on chip-integrated electronic circuits has been limited by the time delay of nanoscale metal connections. However, optical fiber communications present a considerable potential for transmitting vast amounts of data across enormous distances and with considerable bandwidth. To address the problem of low data transmission rates for electronic circuits, waves of light can be utilized as data carriers on nano-chip circuits. The principle subject to conventional dielectric waveguides (DWs) that direct light in the presence of a high refractive index region surrounded by a low-intensity beam is the total internal reflection, which is extracted through Snell's law. Despite this, the light diffraction limit in optically photonic waveguides has been an obstacle to miniaturized photonic waveguides, where the light waves cannot be pressed into a range with dimensions less than half their wavelength in this medium. Unlike Nanophotonics, Plasmonic overcome the light's diffraction limit, Plasmonic waveguides receive a significant interest as they enable light's conversion at sub-wavelength scale at metal-dielectric or metal-dielectric interface. Possible options for the development of a new generation of true nanoscale ultra-small devices that exhibit a large bandwidth operation of photonics include PWs. Let us move on from single interface to multiple interface systems. The coupled system of SPP is created when two metal/dielectric interfaces are placed close to one another and the SPPs associated with each individual interface begin to interact. We can either have a thin metal layer sandwiched between two layers of dielectrics or a thin dielectric layer surrounded by metals, taking into account the SPP modes associated with two metal/dielectric interfaces.

Different waveguide structures for SPPs have been proposed in order to utilize waveguide components of SPPs at the nanoscale. Loss and confinement, despite PWs' significant characteristics, are a significant challenge.

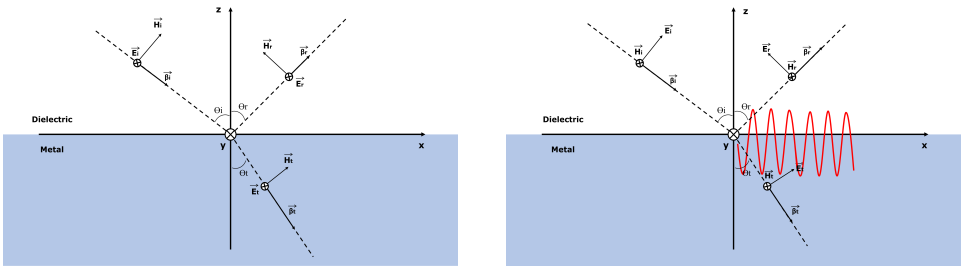

(a) (b)

Figure 2.5: Wave vectors and associated fields for (a) TE mode and (b) TM mode.

2.4.1 Insulator-Metal-Insulator Plasmonic waveguide

An Insulator-Metal-Insulator (IMI) Plasmonic Waveguide is like an optical pathway made of three layers: it's got two outer layers made of insulating material, kind of like the bun of a sandwich, and in the middle, there's a layer of metal figure 2.6. This unique design allows it to do something pretty cool: it can guide light in a way that's smaller and more focused than what traditional materials can achieve [24].

Imagine the insulating layers as walls that keep the light contained within the metal layer. This setup lets us manipulate light at incredibly tiny scales, much smaller than what regular optical materials can manage. It's a bit like a tunnel for light, and it's super useful for creating compact and powerful optical devices, especially in the world of nanophotonics.

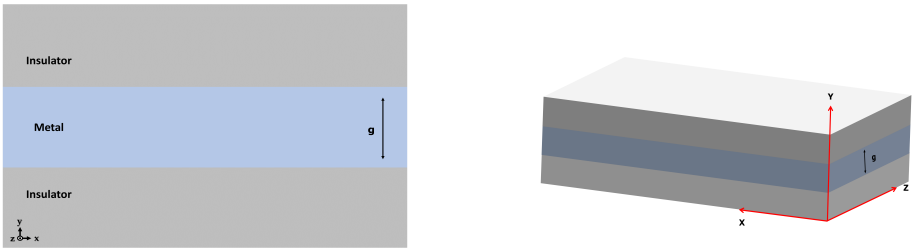

(a) (b)

Figure 2.6: IMI plasmonic waveguide (a) 2D (b) 3D structure.

2.4.2 Metal-Insulator-Insulator Plasmonic waveguide

A Metal-Insulator-Metal (MIM) Plasmonic Waveguide can be likened to a specialized optical conduit characterized by a trilayered composition. This structure comprises two outer metallic layers, akin to the crusts of a sandwich, flanking a central insulating (dielectric) layer [24], analogous to the filling figure 2.7.

This distinctive configuration is distinguished by its capacity to facilitate the guided propagation of Surface Plasmon Polaritons (SPPs) exclusively along the interface shared by the two metallic layers. These SPPs represent a means of channeling and concentrating electromagnetic energy at spatial scales substantially below the diffraction limit, a feat that standard optical materials typically cannot accomplish.

In the realm of nanophotonics, the MIM plasmonic waveguide stands as a pivotal component, affording the development of diminutive yet highly efficacious optical devices. Its role is especially significant in the context of subwavelength optical circuitry and the realization of compact, high-performance photonic systems.

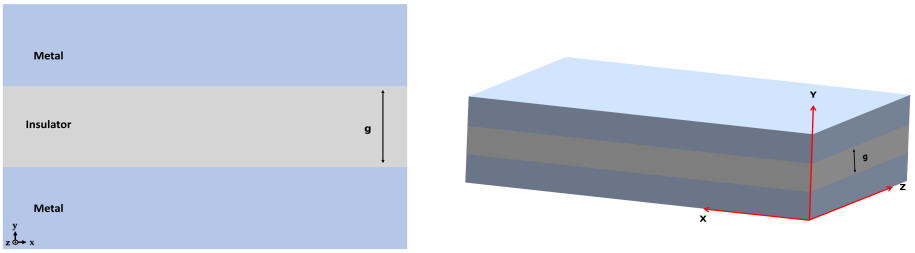

(a) (b)

Figure 2.7: MIM plasmonic waveguide (a) 2D (b) 3D structure.

Comparison between IMI and MIM PWs

Geometries and materials for sub-wavelength surface plasmon modes discusses the properties of plasmonic waveguides and the trade-off between propagation and confinement for surface plasmons. The metal-insulator-metal (MIM) geometry is required to achieve subwavelength pitches with higher confinement factors and smaller spatial extent compared to conventional insulator-metal-insulator (IMI) structures . The propagation lengths for both MIM and IMI waveguides approach that of a single Au-air interface, but the spatial extent and confinement factor are significantly better for MIM geometries . The MIM geometries are better suited for propagating light in subwavelength modes and achieving higher packing densities in nanophotonics applications [24].

2.4.3 Slot waveguide

Slot waveguide is a type of waveguide structure that consists of a narrow slot or gap in a metallic film, surrounded by dielectric material. The primary aim is to assist in the guidance and confinement of electromagnetic waves, specifically plasmonic waves, at scales below the wavelength of the radiation under consideration [25].

symmetric plasmonic slot waveguide

symmetric plasmonic slot waveguide is a structure composed of a slot in a thin metallic film, with a dispersion relation and propagation length that depend on the slot width and height figure 2.8.

Asymmetric plasmonic slot waveguide

An asymmetric plasmonic slot waveguide is a variation of the slot waveguide with different dielectric media above and below the slot, resulting in different effective indices and modal characteristics figure 2.9.

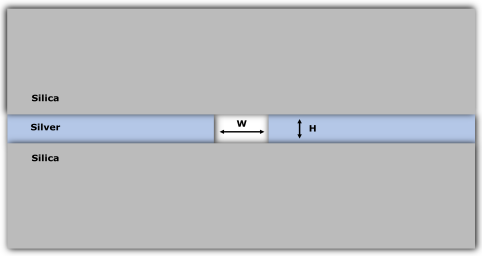

Figure 2.8: Symmetric slot waveguide.

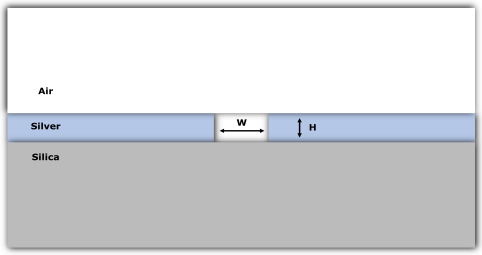

Figure 2.9: Asymmetric slot waveguide.

Plasmonic slot waveguides are compared to other plasmonic waveguide geometries, such as plasmonic strip waveguides, and found to have a larger propagation length for a specific modal size [25].

These findings highlight the potential of slot waveguides for guiding and manipulating plasmonic waves at sub-wavelength scales, with implications for applications in nanophotonics and subwavelength optics.

2.4.4 Metal strip waveguides

Plasmonic stripe waveguides are optical waveguides designed to guide and manipulate surface plasmon polaritons (SPPs) at sub-wavelength scales. They consist of a metallic stripe placed on a dielectric substrate figure 2.10, engineered to match the wavelength of light. These SPPs, generated by the interaction between the electromagnetic field and the metal-dielectric interface, are crucial in nanophotonics, biosensors, photodetectors, and integrated optical circuits.

Strip waveguides offer several advantages in the field of photonics and plasmonics [26].

- One advantage is their ability to support deep sub-wavelength confinement of light, allowing for the manipulation and control of light at the nanoscale.
- They can be used to construct integrated photonic devices with high performance, such as directional couplers, sharply bent waveguides,

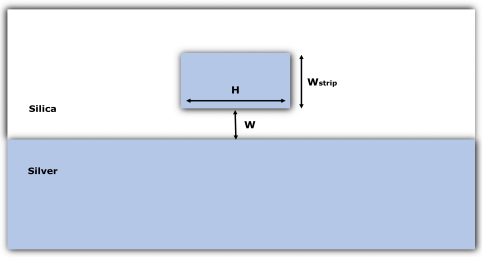

Figure 2.10: Strip waveguide.

and ring resonators, with low insertion losses and nearly zero radiation losses.

- Strip waveguides are compact and simple to fabricate, making them suitable for integration into planar lightwave circuits.
- They have the potential for efficient coupling with dielectric waveguides, enabling the focusing of optical guided waves to nanoscale surface plasmon spots.
- Strip waveguides can be compatible with semiconductor materials and fabrication technologies, allowing for the integration of plasmonic waveguides with other semiconductor devices.
- They offer the possibility of single lateral mode operation and high confinement-to-loss figure of merit, making them attractive for applications in lasers and other photonic devices.
- Strip waveguides can be used for the propagation of bound plasmon-polariton modes with deep subwavelength mode confinement, enabling radiation nanofocusing in air using tapered metal strips.

2.4.5 Plasmonic coaxial waveguides

Plasmonic coaxial waveguides are a type of optical waveguide made of noble metals and filled with glass and air. These waveguides adopt a coaxial cable-like structure, featuring a central rod enveloped by a metallic shell, which can take on various geometries, including annular or elliptic cross-sections. Notably, they possess nanoscale cross-sectional dimensions, enabling the support of low-loss modes characterized by phase velocities approximating the speed of light, with fields primarily localized outside the metal shell. Coaxial plasmon waveguides crafted from noble metals exhibit reduced attenuation of the TEM-like mode in comparison to hollow plasmon waveguides of equivalent dimensions. This mode boasts a symmetric field distribution and lacks a cutoff, permitting superenhanced light transmission. The excitation of these coaxial modes can be achieved through

dipole-like sources, allowing for a comparison of their properties with conventional coaxial waveguides. Plasmonic coaxial waveguides hold promise for applications in miniaturized optical components and nanotechnologies, offering the potential for facilitating light propagation over short distances with minimal losses [27].

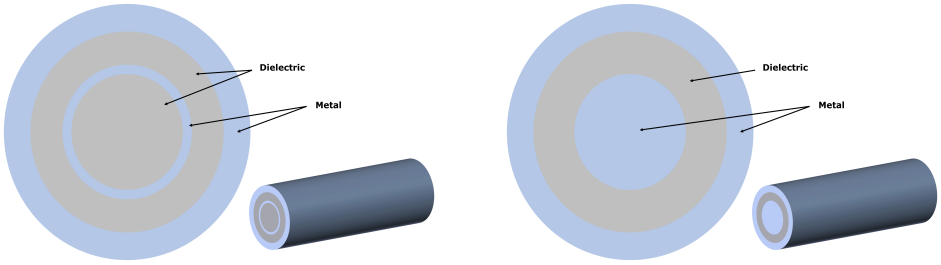

(a) (b)

Figure 2.11: Schematic view of the coaxial waveguide with (a)The coaxial waveguide consisting of two nano-sized metal tubes (b) The coaxial waveguide with bulk inner rod.

2.4.6 Hybrid plasmonic waveguide

The Hybrid Plasmonic Waveguide presents an intriguing confluence of two prominent optical paradigms: surface plasmon polaritons (SPPs) and dielectric waveguides.

The very essence of this innovation resides in its structural composition, a metal cap sheathing a silicon-on-insulator (SOI) platform, interspersed with a minuscule stratum of low-index material as depicted in figure 2.12. This inconspicuous nano-layer serves as the linchpin, orchestrating a remarkable phenomenon characterized as sub-wavelength confinement of light. In layman's terms, it allows us to confine light within spatial scales smaller than the wavelength itself, akin to peering through a microscope with heightened resolution [28].

Furthermore, this hybrid waveguide boasts an attribute of significant import, its propensity for extended optical propagation. This is notably attributable to its exceptionally low loss characteristics, a phenomenon akin to achieving prolonged endurance in a marathon. It enables the waveguide to accommodate optical signals over considerable distances with minimal signal attenuation.

One cannot understate the allure of simplicity, especially within the realm of photonic integration. The fabrication of the hybrid plasmonic waveguide capitalizes on standard planar light wave circuit technology, affording a degree of manufacturing convenience hitherto unseen in analogous

optical configurations. This ease of integration holds profound implications for scalability and practical application.

Of particular note is the confluence of these attributes in the context of optical modulators. These devices function as the arbiters of optical signal modulation, akin to interpreters in a dynamic conversation. The hybrid plasmonic waveguide is uniquely poised for such applications, given its capacity for low-voltage operation and compact form factor, a quality analogous to possessing a versatile tool in a compact toolkit. This aspect bears considerable promise for the development of miniature, energy-efficient optical modulators, a frontier poised to transform the landscape of data communication and optical computation.

In summation, the Hybrid Plasmonic waveguide stands as an exemplar of interdisciplinary ingenuity within photonics. By unifying the advantageous attributes of SPPs and dielectric waveguides, it furnishes an optical platform that transcends conventional boundaries. Its sub-wavelength confinement, extended propagation potential, facile fabrication, and pertinence in optical modulation underscore its transformative potential. As our academic inquiry progresses, it is conceivable that we shall witness the progressive proliferation of nuanced photonic devices, redefining the contours of modern optics.

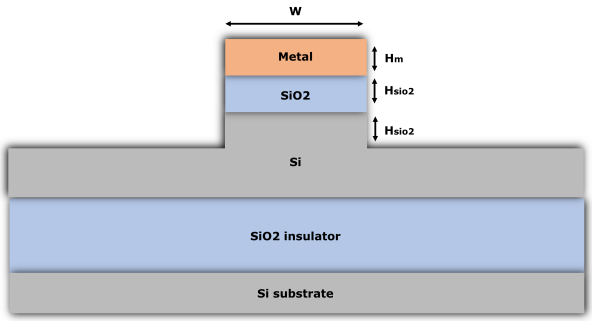

Figure 2.12: Hybrid plasmonic waveguide.

2.5 Performance parameter of PWs

2.5.1 Constituent materials

The process of selecting appropriate components for constructing plasmonic waveguides assumes paramount significance, as it exerts a direct and profound influence on the overarching efficacy and operational efficiency of these waveguides. At the heart of this selection procedure lies the meticulous choice and subsequent integration of constituent materials, with particular emphasis placed on the metal and nonlinear dielectric materials. These

materials are not mere ingredients but, rather, pivotal determinants that significantly shape the performance and functionality of plasmonic waveguides.

The selection of these materials is fundamentally predicated upon their distinct linear and nonlinear properties, which, in turn, exert a discernible influence on the collective behavior and characteristics of the waveguide. In this regard, it is imperative to underscore that the linear properties govern aspects such as propagation loss, dispersion characteristics, and the confinement of optical modes. Conversely, the nonlinear properties are instrumental in modulating the interaction of light with the waveguide, thereby enabling functionalities such as signal amplification and all-optical signal processing[29].

Furthermore, the cogent consideration of the compatibility of the chosen materials with the intended mode characteristics cannot be understated. Mode confinement, dispersion management, and polarization properties are all facets that hinge upon the judicious selection of materials. In essence, the endeavor of determining the appropriate metal and nonlinear dielectric materials transcends mere material selection; it encapsulates an intricate evaluation of how these materials harmonize with the targeted operational objectives of the waveguide.

Hence, it becomes evident that the judicious and informed selection of metal and nonlinear dielectric materials is a pivotal determinant that indelibly shapes the performance and functionality of plasmonic waveguides. This process, akin to a meticulous orchestration, underscores the quintessential role that material choice plays in shaping the capabilities and limitations of these optical structures, heralding a realm of tailored design and performance optimization within plasmonic photonics.

Table 2.1: Properties of different plasmonic materials [21].

Materials	Mechanism	Examples	LSPR range	Advantages	Comments
Metallic nanostructures	Free electrons	Au, Ag, Cu and their alloys	UV–visible	Mature theory of optical properties, various structures, controllable synthesis methods, strong plasmonic effects	Costly, limited permittivity
Semiconductor nanocrystals	Free holes	$Cu_{2-x}S$, $Cu_{2-x}Se$, ITO, TiN	Visible-NIR	smaller size (¡10 nm), broader NIR absorbance	Difficult to dope
2D materials	Electrons and holes	Graphene, MoS_2	NIR	strong plasmonic effect	Tedious synthesis processing, highdemanding synthesis instrument
Conductive polymers	Polaronic charge carriers	poly(3,4-ethylenedioxythiophene:sulfate)	NIR	Switchable state, low cost, flexibility, biocompatibility	Limited to fundamental study, low electrical conductivity, high defect density

2.5.2 Subwavelength confinement

Subwavelength confinement refers to the ability to confine light to spot sizes smaller than the wavelength of light itself. In [30], efficient subwavelength confinement is achieved using surface plasmon polaritons (SPP) in tapered optical fibers, the light propagating along the taper is combined with the excitation of SPP at the tip of the fiber, resulting in high transmission efficiency and the ability to confine light to sub-wavelength spot sizes. In essence, there is a link between creating ephemeral fields beyond the waveguide's core and the confinement of light at subwavelengths in plasmonic waveguides. The optical field constraint of the waveguide can reach a deep sub-wavelength level under the optimal operating wavelength[31]. PWs with highly restricted SPPs quickly developed, demonstrating their capacity to match the subwavelength of traditional DWs[32].

2.5.3 Waveguide geometry

Waveguide geometry can have a significant effect on the performance parameters of a plasmonic waveguide. Here are some key points to consider:

The size and shape

The size and shape of a plasmonic waveguide are crucial factors that profoundly affect its optical behavior and performance. These parameters determine how light is confined within the waveguide, impacting properties such as mode confinement, propagation characteristics, and losses. Properly designing the size and shape allows for optimized performance, efficient coupling of light, and tuning of plasmon resonance frequencies. Additionally, these factors can influence polarization dependence and the ability to match modes with input and output components, making them essential considerations for tailoring plasmonic waveguides to specific applications.

The waveguide geometry in [33] affects the performance parameter of the plasmonic waveguide by increasing the sensitivity of the device by 223.07%.

The coupling interface

The coupling interface affect the plasmonic waveguide In a number of ways, some of them can be mentioned as follows [34] :

- The coupling interface in plasmonic waveguides plays a crucial role in the efficient and flexible manipulation of electromagnetic waves using metasurfaces.
- Introducing a meta-coupling effect in plasmonic waveguides can provide further physical insights into electromagnetic wave control.

- A reflection-type coupling system composed of two identical linear resonances in a metal-insulator-metal configuration can be used to demonstrate the coupling effect in plasmonic waveguides.
- The coupling effect in plasmonic waveguides can be tuned by changing the relative distance or rotation of the resonators, allowing for control over the phase diagram.
- By efficiently engineering the reflection phase shift around the working frequency, the dimensions of the resonators in plasmonic waveguides do not need to be changed.

Plasmon resonance

The resonance wavelength of a waveguide structure is highly susceptible to modification through adjustments to its geometric parameters, notably the gap width and the effective refractive index of the gain medium. These geometric parameters play a pivotal role in influencing various characteristics of the waveguide structure, including mode characteristics, quality factor, and gain threshold, all of which directly impact the resonance wavelength. Furthermore, the length of the resonator and the reflectivity of the end face also exert substantial influence on the effective mode area, thereby further contributing to the determination of the resonance wavelength. In sum, the geometry of the waveguide structure, encompassing parameters such as gap width, effective refractive index, length, and reflectivity, emerges as a critical determinant in shaping the resonance wavelength [31].

2.5.4 Figure of merit

It was thought crucial that the definitions of the figures of merit be clear, understandable, and uncontroversial as well as straightforward to compute given modal quantities. The definitions are based on concepts from economics, specifically the "benefit-to-cost" ratio that consumers construct while evaluating comparable goods made by various manufacturers. The figures of merit are defined as the ratio of a confinement measure to attenuation for a specific mode in the context of SPP waveguides, where the benefit is confinement and the cost is attenuation [35]. Mainly, we can describe the FOM with these equation [36]:

$$FOM_{conf} = \frac{\lambda_0}{\delta} \tag{2.11}$$

Where δ is the skin depth which is the distance over which the amplitude of an electromagnetic wave decays to $1/e$ of its original value due to the absorption of the medium. The skin depth is inversely proportional to the

imaginary part of the wave vector $\delta = 1/Im[K_1]$ which represents the attenuation of the wave.

$$FOM_{prop} = \frac{L_p}{\lambda_{spp}} \tag{2.12}$$

Where the L_p is the ratio of the propagation length and λ_{spp} is the wavelength of the surface plasmon polariton.

A higher FOM indicates a stronger confinement of the electromagnetic field and a better performance of the plasmonic device [36].

2.5.5 Attenuation length

The attenuation length, a pivotal parameter in the realm of plasmonic waveguides, delineates the distance over which surface plasmon polaritons (SPPs) can travel before experiencing a notable reduction in their intensity. This critical metric is contingent upon a multitude of factors, including material selection, operating wavelength, surface quality, geometric configuration, frequency-dependent material characteristics, and the local environment. In practical terms, the aim is to optimize these variables to maximize the attenuation length, as it profoundly influences the efficacy of plasmonic waveguides for various scholarly and practical applications, encompassing fields such as sensing and integrated photonics.

The investigation into the attenuation length in plasmonic waveguides has garnered attention in numerous research studies. A particular study introduced a groundbreaking hybrid terahertz plasmonic waveguide architecture known as the silicon metal silicon (SMS) waveguide, which exhibited a propagation length surpassing 14 mm [37]. Another analysis was conducted to examine an electro-optical switch that depends on a plasmonic waveguide structure in the shape of a T. This specific switch has the capability to serve as a variable optical attenuator, facilitating the decrease in the power of a light beam from 6 dB to 30 dB [38]. A proposal was put forth for a hybrid plasmonic waveguide structure based on a grating at the centimeter scale. This structure demonstrated a remarkable propagation length of up to 3.6 cm while maintaining low levels of loss [39].

2.6 Advantages and disadvantages of Plasmonics

The field of plasmonics offers remarkable capabilities for the precise control and manipulation of electromagnetic waves at the nanoscale, with diverse applications across various domains.

2.6.1 Advantages of Plasmonics

Plasmonics for manipulating light

- Plasmonics allows for spatial and temporal control of electromagnetic waves.
- Digital technology combined with meta-materials enables digital coding and modulation of surface plasmons at the deep-subwavelength scale.
- Plasmonic meta-surfaces offer tunable conformal designs with high modulation depth.
- Active dispersion engineering allows for dynamic switching between different dispersion states, enabling digital modulations of both amplitude and phase of surface waves.
- Potential for subwavelength integrated plasmonic circuits with applications in nanophotonics and information processing [40].

Applications of Plasmonics in Photonic components

- Plasmonic materials and meta-materials enable precise control of light at the nanoscale, leading to the development of on-chip lasers, modulators, detectors, and molecular sensors.
- Plasmonics allows for sub-diffraction-limited optical microscopies, improving imaging capabilities.
- Plasmonic devices concentrate light into small volumes, enabling sensitive molecular sensors and improved photovoltaic devices.
- Applications in rapid medical diagnostics, hot-carrier-based devices, and communication systems.
- Metasurfaces in plasmonics promise planar on-chip optics, sensing, imaging, and communications, enhancing light-matter interactions.

Plasmonics in bio-sensing

- Plasmonic resonance techniques offer label-free, signal enhanced, and real-time sensing for bioparticles and bioprocesses at the molecular level.
- Plasmonics-based biosensors extensively explored using synthesized nanoparticles and manufactured nano-patterns in thin films [41].

- Plasmonic biosensors with nanovoids in thin films have the potential to achieve integrated lab-on-a-chip devices capable of transporting and detecting multiple bio-analytes with high sensitivity, selectivity, multi-channel capabilities, and dynamic monitoring [41].
- Overall advantages in biosensing, including label-free detection, signal enhancement, real-time sensing, and the potential for integrated lab-on-a-chip devices with high sensitivity and selectivity

Plasmonics in quantum optics

- Plasmonics enables ultimate miniaturization of photonic components for quantum optics, allowing for the development of smaller and more efficient devices.
- Plasmonic modes offer broadband and extreme mode confinement, along with enormous field enhancement through metal nanostructures.
- Facilitates ultra-strong coupling to quantum emitters, enhancing the interaction between light and matter.
- Placing quantum emitters in optical resonators with high-quality factors and small volumes enhances spontaneous emission, leading to improved performance in quantum technologies.
- Plasmonics can promote electrodynamics beyond the accurate description of local-response approximation, potentially leading to breakthroughs in understanding light-matter interactions.

2.6.2 Disadvantages of Plasmonics

Challenges in efficient coupling and control

- Challenge in achieving efficient coupling between free-space light and surface plasmons, leading to significant losses and limited transmission distances.
- Sensitivity of plasmonic devices to fabrication imperfections and material losses, potentially degrading performance and reliability.
- Plasmonics research is in early stages, necessitating further exploration and development of practical applications and scalable manufacturing techniques [40].

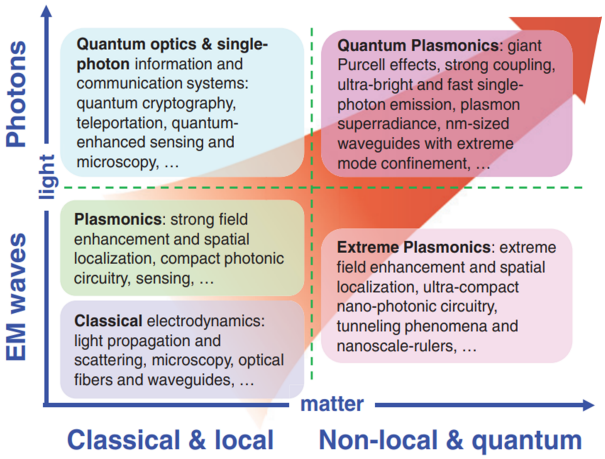

Figure 2.13: Quantum plasmonics explores quantum nonlocal response of matter and quantized light fields, paving the way for emerging quantum technologies that harness the quantum concert of light and matter [42].

Material limitations and fabrication challenges

- Plasmonic devices predominantly use noble metals with high optical loss and limited tunability, posing challenges in standard semiconductor fabrication and integration, preventing full CMOS compatibility and widespread utilization.
- Key challenge in finding novel materials to replace traditional plasmonic metals.
- Specialized fabrication techniques required for plasmonic device manufacturing, potentially limiting scalability and practical implementation.

Energy loss and limitations in light-matter Interactions

- Plasmonic modes associated with energy loss in metals due to radiation absorption, potentially limiting overall efficiency and performance of plasmonic devices [42].
- Balancing the unique features of plasmonic modes, like extreme mode confinement and field enhancement, with energy loss to avoid detriment to performance.
- Exploration of fundamental limits in light-matter interactions involving trade-offs and conflicting tendencies that need careful analysis and

assessment [42].

2.7 Plasmonic applications

Due to its distinct attributes and capabilities, plasmonics, which refers to the examination and implementation of the interaction between an electromagnetic field and unrestricted electrons within a metallic material, exhibits a diverse range of applications across multiple domains. The subsequent enumeration outlines several significant sectors wherein the utilization of plasmonics prevails.

2.7.1 Plasmonic waveguides and modulators

A possible alternative for high-performance nanoscale communication photonic devices is plasmonic waveguides and modulators. These devices control the amplitude or phase of the propagating plasmons using the interaction between light and free electrons on a metal surface [43]. Plasmonic modulators can be made more efficient by incorporating plasmonic modes and electrical signals to guide the optical phase delay, enabling efficient electro-optic modulation. Additionally, plasmonic-organic hybrid (POH) waveguides, which combine nonlinear organic electro-optic materials and surface plasmon polaritons, have been developed to achieve light modulation in devices with micron-scale lengths[44], and these devices have the potential for optimization through computational modeling, which allows researchers to experiment with different device parameters and inform the fabrication of actual test devices, furthermore, the integration of phase-change materials into metal-insulator-metal (MIM) waveguide systems has enabled the realization of chip-scale plasmonic modulators and switches with excellent modulation depth and fast response times.

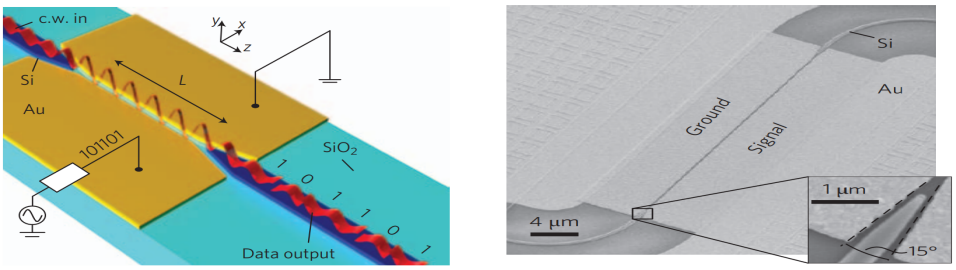

(a) (b)

Figure 2.14: Plasmonic modulator (a) plasmonic phase modulator Schematic (b) plasmonic phase modulator picture from scanning electron microscopy [45].

Surface-enhanced spectroscopy

Plasmonic surface-enhanced spectroscopies (SES) are powerful techniques for enhancing the signal and detecting surface trace species. These techniques utilize plasmonic metallic nanoparticles or graphene substrates to enhance conventional Raman or infrared spectroscopy signals. SES has been applied in various fields such as on-site detection, food inspection, environmental monitoring, and surface analysis. The development of robust substrates and the optimization of parameters such as particle length and cluster size have led to significant enhancements in signal intensity and reproducibility [46][47]. SES has been used in time-resolved spectroscopies to study reaction mechanisms and developing of new plasmonic spectroscopies for in situ surface species detection and catalytic process monitoring, these techniques show great potential for both fundamental research and practical applications [48][49].

Plasmonic antennas

Plasmonic antennas have been extensively studied for their potential applications in next-generation networks. These antennas offer unique features that can be exploited for tailoring and tuning light radiation and propagation properties at nanoscale dimensions. Plasmonic antennas exhibit great potential as a viable framework for diverse applications. The optimization of light-matter interaction heavily relies on the intricate design of plasmonic nanocavities [50]. In partticular, plasmonic nanoantennas have shown promise enhanced and controllable light-matter interaction and strong coupling between far-field radation and localized sources at the nanoscale [51]. Wideband plasmonic optical fractal patch antennas have also been suggested for usage in optical interconnects, providing potential remedies for interconnect density, power consumption, and data rate restrictions. In [52], The proposed system allows for the transmission of spin up and spin down signals, as well as the formation of a flip flop (clock) signal, achieving transmission bit rates of $\sim$ 40.000 $Tbit\ s^{-1}$ (40 $Pbit\ s^{-1}$) using spin projection modulation control. Overall, plasmonic antennas hold great potential for the development of next-generation networks, offering improved performance and capabilities in various applications

2.7.2 Sensing and detection

Plasmonic sensors are types of optical sensors that utilize surface plasmon resonance (SPR) to detect and analyze various substances. The fundamental principle involves the interaction of the analyte with the plasmonic-sensitive domain, typically overlaid with a thin metallic film, such as gold or platinum. This interaction instigates alterations in the refractive index, which are quantifiable and instrumental in ascertaining the analyte's

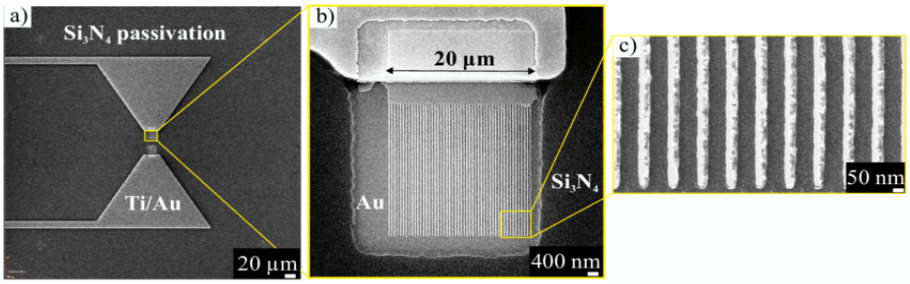

Figure 2.15: SEM images of the fabricated plasmonic photoconductive antenna [53].

existence and concentration. The advancement of plasmonic sensors encompasses a spectrum of material compositions and structural arrangements. The sensors have exhibited exceptional sensitivity and discernment, rendering them appropriate for a wide range of applications such as refractometry, chemical identification, and monitoring of drug dosage.

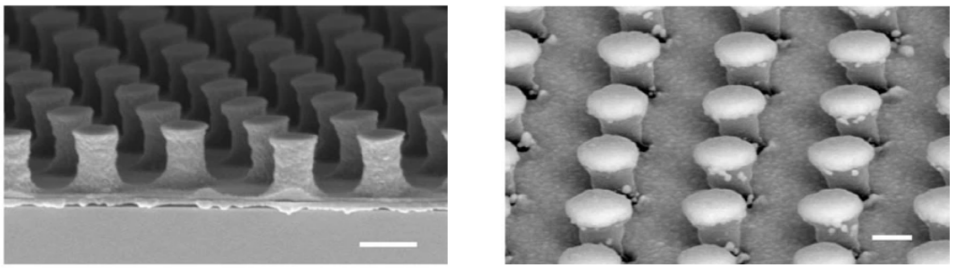

(a) (b)

Figure 2.16: Fabricated gold mushroom array (GMRA), which is characterized by its sensitivity capabilities (a) a periodic array of rounded square photoresist pillars (b) a gold-deposited photoresist array; captured in SEM images [54].

2.7.3 Energy and photovoltaics

Plasmonic photovoltaics (PVs) involve the incorporation of metallic nanoparticles into the photovoltaic active layer to enhance optical absorption and improve the efficiency of PV cells. Different shapes and materials of nanoparticles have been studied for this purpose. In the field of plasmonic solar panels, scientists have been experimenting with different shapes and materials for tiny metallic particles to make them work better in capturing light. These particles, like spheres, rods, nanocoax [55], nanowires [56] and shells, have their own special light responses that can be customized for spe-

cific types of light. Additionally, improved techniques for creating these tiny particles with great precision have made them even more effective in interacting with light. Plasmonic nanoparticles enhance photovoltaic device efficiency by concentrating and trapping light near them. This enhances photon absorption and distribution. Researchers are exploring hybrid approaches, combining plasmonic nanoparticles with other materials for improved light trapping and charge carrier generation. This technology is being explored in combination with anti-reflection coatings and light management strategies. The field of plasmonic photovoltaic continues to evolve [57].

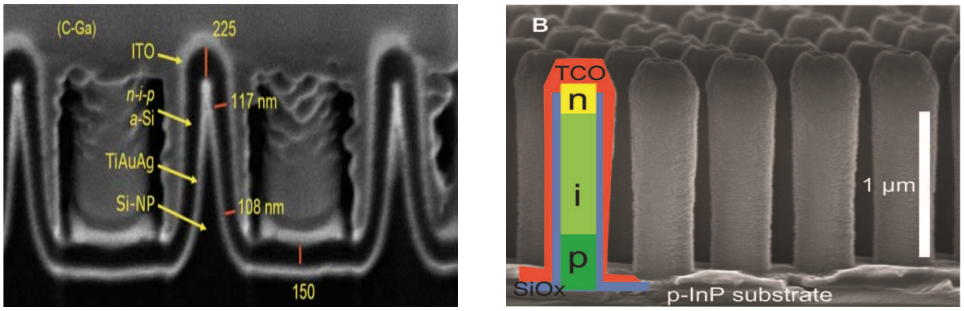

(a) (b)

Figure 2.17: SEM images of (a) nanocoax [55], and (b) nanowires [56], based solar cells.

2.7.4 Plasmonic light-emitting diodes (LEDs)

Recent research has focused a lot of interest on Plasmonic-based light-emitting diodes (LEDs). They offer potential improvements in device performance, such as lower turn-on voltages, higher external quantum efficiencies, and luminance. By incorporating plasmonic nanoparticles, like Au and Ag, along with carbon nanostructures, LEDs can achieve enhanced properties and new possibilities for lightweight and flexible devices with better thermal management [58]. Plasmonic structures have shown great potential in increasing the spontaneous emission rates of emitters and improving light extraction efficiency in LEDs. This types of diodes can have a various potential application from the UV to NIR/IR wavelengths as can be seen in figure 2.18.

There are a lot of different types and methods used to fabricate PLEDs. As, for example, in [60], an on-chip electronic-plasmonic transducer capable of both direct plasmon generation and detection at high efficiencies. The structure consists of MIM connected by two wires made of different metals. The PLED structure is depicted in figure 2.19(a) and figure 2.19(b) as it is functioning.

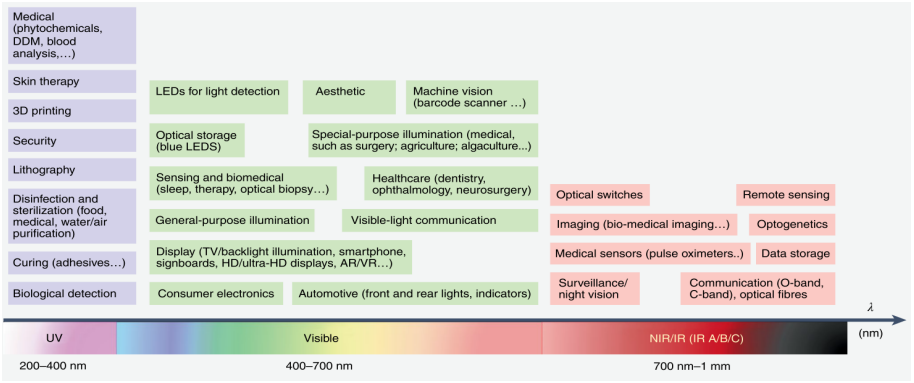

Figure 2.18: Potential application of Plasmonic LED of differentiate wavelengths [59].

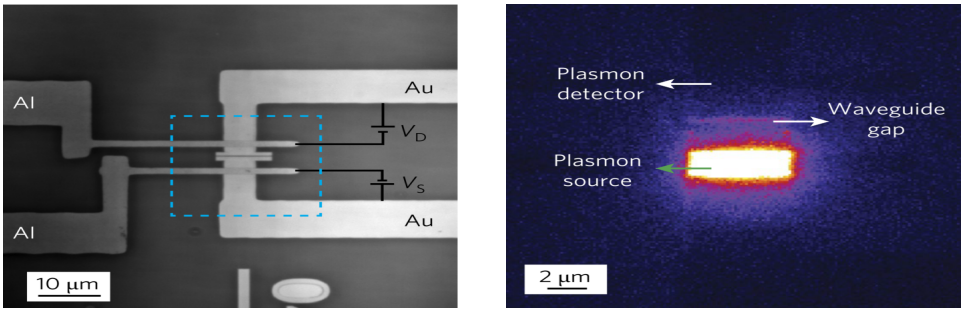

(a) (b)

Figure 2.19: Plasmonic LED in case of (a) inactivity, and in case of (b) interaction [60].

2.7.5 Metamaterials and cloaking devices

Recent research in plasmonic metamaterial cloaking for optical frequencies is gaining traction. Scientists have proposed designs for cylindrical and spherical cloaks using alternating plasmonic and non-plasmonic materials, mimicking an effective epsilon-near-zero material at optical frequencies [61] [62]. Additionally, a significant advancement involves a non-resonant plasmonic metamaterial achieved through transformational optics, enabling broad-bandwidth cloaking [62]. Optical metasurfaces with shaped nanoparticle arrays are emerging as realistic optical mantle cloaks for non-dielectric objects, further advancing potential applications in optical devices [63]. These breakthroughs collectively signify a promising future for integrating plasmonic metamaterial cloaking into optical technologies.

2.7.6 Data storage and information technology

Plasmonic data storage is a promising technology for applications such as color displays, data storage, and information encryption. Various methods have been proposed and demonstrated to achieve plasmonic color generation and data storage. One approach involves utilizing ultra-thin metasurfaces and metallic nanoparticles to generate static colors [64]. Another method involves direct laser writing to create gold plasmonic nanostructures, enabling applications such as text writing, barcodes, and QR codes for message storage [65]. Additionally, 3D Janus plasmonic helical nanoapertures have been fabricated for direction-controlled polarization-encrypted data storage, allowing for the display of different images depending on the incident polarization [66]. Furthermore, a compact plasmonic data storage system has been proposed using nematic liquid crystal layers and nano-silver sheets, enabling high-speed sequential writing and reading with multiple binary states [67]. These advancements in plasmonic data storage offer potential for high-density optical data storage, optical information encryption, and optical information processing.

2.8 Conclusion

In summary, the dynamic interplay between light polarization and plasmonic waveguides has emerged as a captivating avenue, propelling advancements in the realm of photonics. A profound grasp of light polarization enables the strategic design and engineering of plasmonic waveguides, imbuing them with enhanced functionalities tailored to specific applications. The fusion of polarization control with plasmonic waveguides has unshackled the potential to forge highly efficient, compact, and versatile optical components, spanning from sensors to modulators and beyond. Furthermore, the capability to guide and manipulate light at the nanoscale through plasmonic waveguides holds significant promise for pioneering breakthroughs across diverse domains, including nanophotonics, quantum optics, and information technology. As we persist in our exploration of this enthralling realm, continued research endeavors will undoubtedly unravel new dimensions and opportunities, propelling us toward a future where precise manipulation of light polarization via plasmonic waveguides will redefine the modern photonics landscape and revolutionize a myriad of applications.

Chapter 3

Modeling Techniques and Fabrication

3.1 Introduction

3.2 Modeling techniques

Numerical methods are important tools used in engineering practice to find approximate solutions for physical problems when exact solutions are unavailable. They are particularly important in engineering practice, where physical phenomena need to be simulated. Mesh-based approaches and meshless methods can be used to categorize these techniques. Mesh-based methods include the finite element method (FEM), the finite volume method (FVM) and Finite-Difference Time-Domain (FDTD). Meshless methods, such as the element free Galerkin method (EFG) and the smoothed particle hydrodynamics (SPH) method, do not rely on a mesh and instead use particles or other techniques for discretization. These methods have advantages over experimental methods, as they are more cost-effective and provide more detailed information about the model. Differential equations that cannot be resolved analytically are approximated using numerical methods. They are used widely in engineering, mathematical physics, and linear algebra.

3.2.1 FDTD

The Finite Difference Time Domain (FDTD) method is like a virtual laboratory for studying how electromagnetic waves behave when they encounter moving objects. It was first discussed in 1966 by Kane Yee [68], then developed by Taflove and Brodwin in 1975 [69]. To do this, it divides the computational area into two types of regions: one with a fine mesh and another with a coarser mesh. This clever division reduces the demand for

heavy-duty computer memory and processing power.

In the past, there was a hitch called the Courant-Friedrichs-Levy (CFL) constraint that insisted on very fine details in some parts. But now, a smart technique called "one-step leapfrog," which is part of the alternately direction-implicit (ADI) FDTD approach, has come to the rescue. It lets us keep things efficient and accurate even in regions with less intricate details.

The FDTD method isn't just theory; it's practical. It helps us understand how objects in motion can tweak the frequency and size of electromagnetic waves that bounce off them. It's handy for exploring classic experiments like the Michelson-Morley experiment, a cornerstone in physics history. Plus, it lets us investigate time delays caused by moving objects. So, it's a powerful tool for figuring out how electromagnetic waves dance with things in motion, and it finds uses in all sorts of places, from physics labs to engineering projects.

The basis of an FDTD (Finite Difference Time Domain) code relies on two equations: the Maxwell-Faraday and Maxwell-Ampère equations in their temporal domain form. The FDTD method allows for the calculation, at each discrete moment in space, of the components of the electromagnetic field in each parallelepiped cell of the three-dimensional volume.

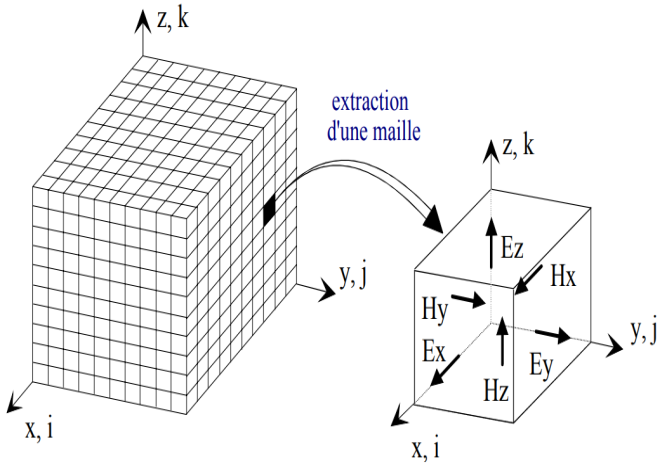

(a)

Figure 3.1: The construction of the Yee cell used in the FDTD method (in 3D) [70].

By using MKS system of units, the Maxwell's equations in the rectangular coordinate system, the Yee algorithm can be described by [69]:

$$\frac{\partial H_x}{\partial t} = \frac{1}{\mu}\left(\frac{\partial E_y}{\partial z} - \frac{\partial E_z}{\partial y}\right) \tag{3.1a}$$

$$\frac{\partial H_y}{\partial t} = \frac{1}{\mu}\left(\frac{\partial E_z}{\partial x} - \frac{\partial E_x}{\partial z}\right) \tag{3.1b}$$

$$\frac{\partial H_z}{\partial t} = \frac{1}{\mu}\left(\frac{\partial E_x}{\partial y} - \frac{\partial E_y}{\partial x}\right) \tag{3.1c}$$

$$\frac{\partial E_x}{\partial t} = \frac{1}{\varepsilon}\left(\frac{\partial H_z}{\partial y} - \frac{\partial H_y}{\partial z} - \sigma E_x\right) \tag{3.1d}$$

$$\frac{\partial E_y}{\partial t} = \frac{1}{\varepsilon}\left(\frac{\partial H_x}{\partial z} - \frac{\partial H_z}{\partial x} - \sigma E_y\right) \tag{3.1e}$$

$$\frac{\partial E_z}{\partial t} = \frac{1}{\varepsilon}\left(\frac{\partial H_y}{\partial x} - \frac{\partial H_x}{\partial y} - \sigma E_z\right) \tag{3.1f}$$

assuming that the dielectric parameters μ, ε and σ are independent of time.

Comparing this method to frequency-domain approaches, there are two advantages. The primary benefit is that complex scatterers may be easily implemented, as each lattice point can have an arbitrary dielectric parameter applied to it. Second, given the large number of interesting scatterers, its memory consumption is not prohibitive. This particular technique exhibits two limitations in comparison to approaches based on the frequency-domain. Initially, its precision is merely approximately 10 percent, which is at minimum one magnitude inferior to that of the alternative techniques. Subsequently, the demanded duration for program execution may surpass the acceptable limit for certain computational budgets [69].

3.2.2 FEM

Over the years, FEM's development has been a fascinating journey marked by major breakthroughs in the field of solid mechanics. It all began in 1941 when FEM emerged as a theoretical framework, laying the essential groundwork for its subsequent evolution into a powerful numerical method. Through the dedicated efforts of researchers and engineers, FEM has grown into the preferred approach for addressing a wide range of solid mechanics problems. Along the way, various innovative model reduction techniques, such as the hyper reduction method, reduced basis method, and the proper generalized decomposition (PGD) based model reduction, inspired by the likes of Oden, Lax, Clough, Wilson, Felippa, Feng, and Stein, have been introduced to expedite simulations and enhance its applicability. This historical journey can be further explored through the insights provided in articles and books by these influential figures, underscoring the dynamic

and evolving nature of FEM in its quest to better understand and solve complex engineering challenges [71].

Application of the FEM for the solution of 2-D Boundary-Value Problems involves essentially the same methods as solving 1-D problems. In particular, the following crucial actions must be taken in order to properly apply the FEM to the solution of 2-D BVPs [72]:

- Domain discretization.
- Interpolation Functions.
- Proper choice of interpolation functions.
- Evaluation of Element Matrices and Vectors.
- Assembly of the global matrix system.
- Imposition of boundary conditions.
- Solution of the global matrix system.
- Post-processing of the results.

The study will use a generic second-order partial differential equation to illustrate the major steps in a 2-D nodal FEM, This generic type partial differential equation can be expressed as [71]:

$$\frac{\partial}{\partial x}\left(\alpha_x \frac{\partial u}{\partial x}\right) + \frac{\partial}{\partial y}\left(\alpha_y \frac{\partial u}{\partial y}\right) + \beta u = g \tag{3.2}$$

where α_x, α_y, β and g are variables that must be specified by the particular application, and u is the main unknown quantity. In the world of numerical simulations, domain discretization is like our trusty map—it helps us break down the computational territory into smaller, more manageable pieces. This is particularly handy when we're dealing with phenomena that are too tricky for the usual equations to handle. By using domain decomposition methods (DDM), you can slice up the domain into smaller sections and then work on each section separately figure 3.2. The beauty of this is that it often speeds up the whole process, making it a favorite approach to getting results faster, especially when compared to the more traditional solver strategies.

A demonstration of the comparison between the solution obtained through the employment of the finite element method and the solution derived from analytical means is visually represented in Figure 3.3.

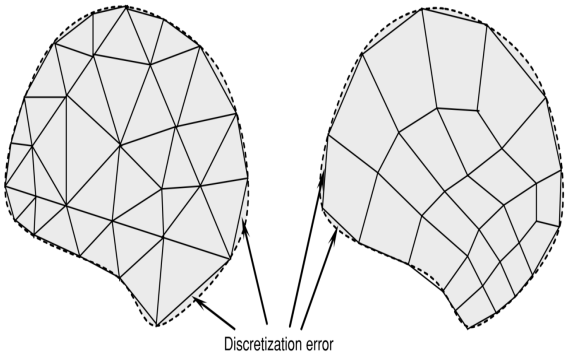

(a)

Figure 3.2: Finite element mesh using (a) triangular and (b) quadrilateral elements [71].

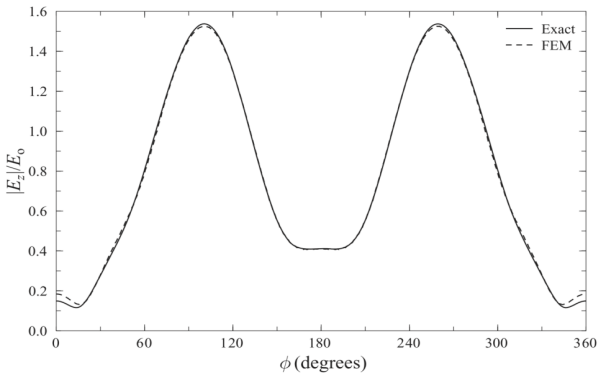

(a)

Figure 3.3: Comparison of electric fields between analytical solution and FEM [72].

3.3 Simulation softwares

3.3.1 Lumerical FDTD

Lumerical FDTD is specialized software meticulously crafted to mimic and scrutinize how light behaves within photonic and optoelectronic devices. This computational technique is a quintessential asset in the vibrant realm of photonics, a scientific discipline dedicated to the art of generating, manipulating, and detecting particles of light, known as photons, for a wide spectrum of practical applications. These applications span across the domains of optical communication, laser technology, photovoltaics, and an array of other captivating fields where harnessing the power of light is paramount. Within its toolbox, Lumerical FDTD wields the FDTD method. This em-

powers a community of researchers and engineers, granting them the artistry to craft and fine-tune an extensive repertoire of photonic instruments. These span the gamut from optical waveguides to photonic integrated circuits, from delicate nanophotonic structures to energy-harvesting photovoltaic cells, all under the benevolent guidance of Lumerical FDTD. The software offers a scripting environment and graphical user interface for creating and executing simulations, along with tools for displaying and evaluating simulation output. In order to create and optimize photonic devices for a range of applications, as well as to further the development of photonics technology, lumierical FDTD is widely utilized in both academia and industry.

3.3.2 COMSOL Multiphysics

A comprehensive and potent software platform, based on FEM method, COMSOL Multiphysics aids scientists, engineers, and researchers in simulating and modeling a variety of physical events and processes in a wide range of fields, including manufacturing, science, and engineering. It's a software for multiphysics simulation that enables the coordinated simulation of several physical events.

In the realm of COMSOL Multiphysics, users find themselves empowered to craft intricate numerical simulations of an extensive array of physical systems, each riddled with their unique complexities. These systems may involve the interplay of heat transfer, fluid dynamics, structural mechanics, electromagnetism, acoustics, and chemical reactions. What makes this software particularly accessible is its intuitive user interface, designed to facilitate the definition of geometries, material properties, the formulation of governing physics equations, as well as the execution of simulations and the scrutiny of ensuing results. It is a valuable instrument in the hands of researchers and engineers, offering a robust means to dissect, analyze, and understand intricate physical phenomena within the bounds of the academic and industrial landscapes.

3.3.3 JCMwave

JCMwave is a computational software package used for the simulation and analysis of electromagnetic and photonic devices. It is based on FEM method and primarily focused on solving Maxwell's equations, which describe the behavior of electromagnetic fields, to model and understand the interactions of light with various structures and materials. JCMwave is commonly employed in the field of photonics, which involves the study and application of light-based technologies.

Researchers and engineers use JCMwave for tasks such as designing and optimizing photonic devices, including photonic crystals, optical waveguides, and nanophotonic structures. It is particularly valuable for solving problems

related to wave propagation, light scattering, and resonance phenomena.

JCMwave offers a user-friendly interface and powerful numerical solvers, making it a valuable tool for simulating and analyzing complex optical and electromagnetic systems in a variety of applications, including telecommunications, optoelectronics, and nanotechnology.

There are a lot of other commercial and non-commercial software tools that are used in the filed of photonics and plasmonics such as $HFSS$ based on FEM method, CST based on FIT method and $MAGMAS$ $3D$ based on $IE - MoM$ [73].

3.4 Softaware comparaison

COMSOL, CST, Lumerical, JCMwave, and HFSS are compared in various papers [73][74][75]. The comparison includes accuracy of results, simulation time, and the ability to simulate complex structures. A lot of studies have conducted a comparison between software tools in many filed, in [74] HFSS and CST Microwave Studio are compared for simulating a circular horn antenna, with results presented in 3D and polar gain plots, In terms of accuracy, the results of the conical horn antenna simulation are nearly identical for both software programs. However, in terms of time, HFSS is superior.

Comparison of Electromagnetic Field Solvers for Plasmonic Nano Antennas have been studied in [75], various frequency domain solvers have been compared for the analysis of plasmonic nano antennas, including $JCMsuite$, $Comsol$, $HFSS$, and $Microwave\ Studio$, with the semi-analytic MMP code that is known for its fast convergence and high accuracy. The JCMwave package is mentioned as providing the best accuracy in the analysis of plasmonic structures, particularly when using a Fourier decomposition of the axi-symmetric geometry with 2% error around the wavelength of 500 nm. The second best package is comsol Multiphysics software with maximum of 6% around the wavelength of 500 nm as can be seen in figure 3.4 (a), it is worth mentioning that both $JCMsuite$ and *comsol* get the same results and the percentage of error is not accurate in the results as witnessed in figure 3.4 (b).

The selection of the field solver can significantly reduce computation time and memory requirements, depending on the specific properties of the problem to be solved. It is important to note that the choice of software depends on the specific requirements and properties of the problem at hand, and software vendors strive to offer general packages that can handle various 2D and 3D problems.

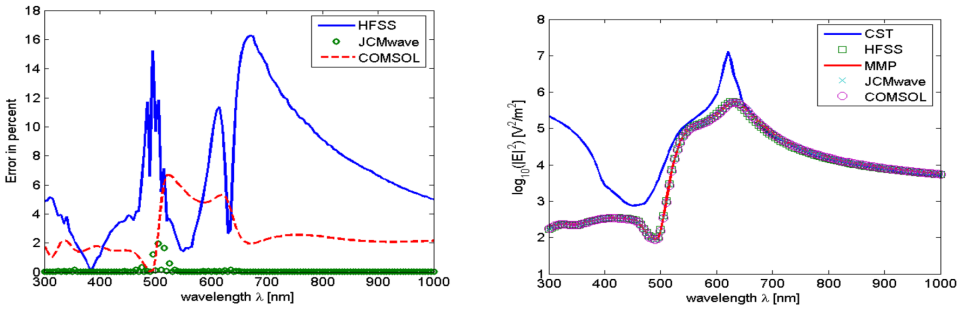

(a) (b)

Figure 3.4: Comparison results of (a) error percentage and (b) the squared electric field according to the wavelength. [75].

3.5 Fabrication techniques

In the realm of plasmonic structures, crafting them requires a set of fabrication steps. Exciting progress in nanofabrication technologies has unlocked the ability to finely tune and control these tiny plasmonic structures at the minuscule nanometer scale. Because of recent advances in nanofabrication technology, control over plasmonic nanostructures at the nanoscale scale is now extremely precise and accurate and various fabrication techniques have been investigated as shown in figure 3.5.

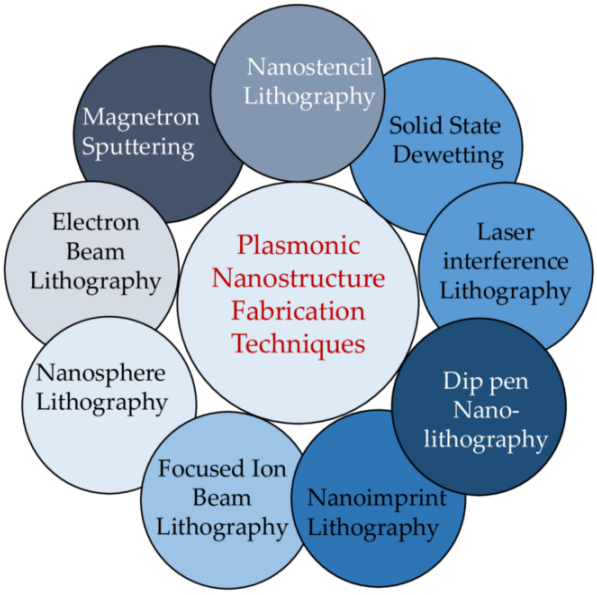

Figure 3.5: Fabrication techniques for plasmonic nano structures [76].

There are mostly two main types Techniques for Fabrication: Lithography and Non-Lithography.

3.5.1 Lithographic techniques

Dip-pen nanolithography

DPN was invented in 1999 by Richard D. Piner, Jin Zhu, Feng Xu, Seunghun Hong and Chad A. Mirkin, wherein Alkanethiols were directly applied to a gold thin film using an atomic force microscope (AFM) tip in a way similar to a dip pen as seen in figure 3.6 [77].

It was carried out in a "single pen" manner in the DPN report's initial version. Despite its high resolution and excellent patterning flexibility, it was criticized for having an incredibly poor throughput. In order to overcome the difficulty, a variety of cantilever tip arrays were used to create parallel DPN (p-DPN). In the array operation, the other tips passively perform the parallel writing while only one of the parallel tips is used to monitor the lithography process via a feedback mechanism. As a result, the number of tips operating concurrently in an array determines how much throughput DPN can handle [78].

In 2000, the p-DPN concept was originally shown using eight tips in an array; in 2005, it was expanded to 250 tips. A 55000-tip array spanning one square centimeter was used in 2006 to accomplish a true large-area DPN parallelization. Because of its extremely high density, this enormous tip array serves as the basis for high-throughput DPN patterning, which is especially helpful for creating combinatorial libraries of features with regular variations in size, spacing, and form [78].

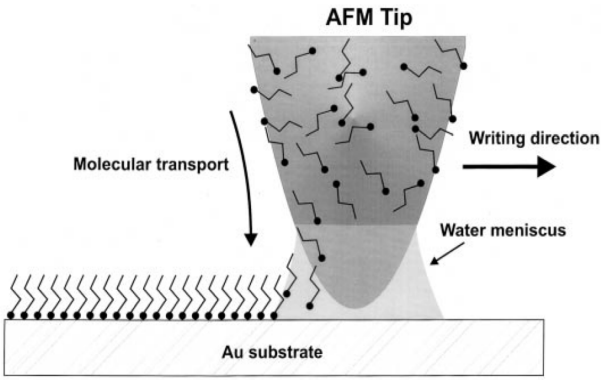

(a)

Figure 3.6: The basic schematic pepresented of DPN in 1999 [77].

Electron beam lithography

Electron beam lithography (EBL) is a high-resolution technique used to micro- and nanofabrication processes. It employs a precisely focused electron beam to meticulously delineate intricate patterns onto a substrate. Electron beam lithography (EBL) has a multiple steps from substrate preparation, resist coating, electron beam exposure, pattern design, development to post-processing, to create high-resolution patterns for micro- and nanoscale devices.

The source material can be evaporated utilizing high energy electrons in the form of an intense beam in electron beam evaporation. A heated filament creates thermionic emission of electrons, which can give enough energy to evaporate any material following acceleration. On impact, 10 kW is delivered in a typical situation involving 1 A of emission accelerated by a 10 kV voltage drop. To avoid melting the filament in the approaching evaporant, the filament is placed out of sight of the evaporant, as illustrated in figure 3.7, and the electron beam is drawn around to the surface by a magnetic field, B, the point in this figure displays the direction. Lorentz force is defined as the combined force, (F), on an electron in an electric (E) and magnetic field (B) [79].

$$\boldsymbol{F} = \boldsymbol{F_E} + \boldsymbol{F_B} = q_e\boldsymbol{E} + q_e(\boldsymbol{v} \times \boldsymbol{B}) \tag{3.3}$$

where F is in N, q_e in C, E in V/m, B in tesla, and the electron velocity v is in m/s.

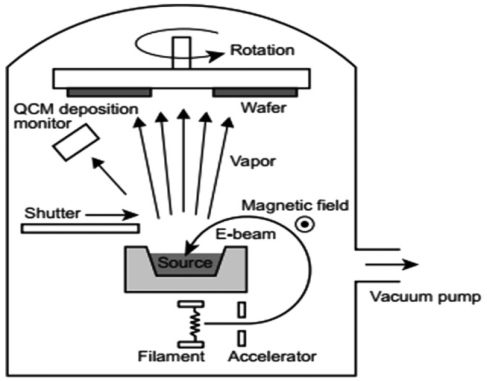

(a)

Figure 3.7: A schematic representation of the electron beam evaporation system's phenomenon [79].

Focused ion beam

This techniques was first discussed by W. H. ESCOVITZ, T. R. FOX,

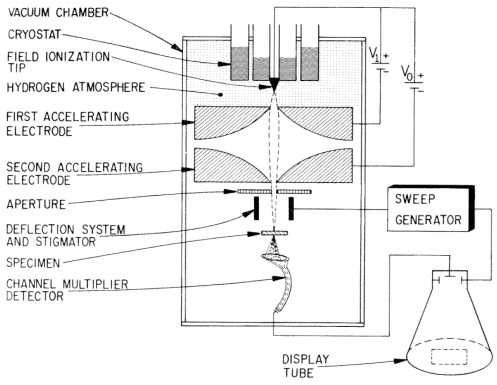

(a)

Figure 3.8: Schematic diagram of the first proposed FIB [80].

AND R. LEVI-SETTI in 1975 [80], after this technique get developed by several researchers. Focused ion beam (FIB) technology have significantly enhanced its capability to fabricate intricate nanoscale structures with remarkable precision and adaptability. FIB-based nanofabrication encompasses four primary techniques, namely milling, implantation, ion-induced deposition, and ion-assisted etching, enabling both subtractive (milling and etching) and additive (implantation and deposition) processes. The essential components of an FIB system include an ion source, ion optics, a substrate stage, and a vacuum chamber equipped with auxiliary tools. Notably, recent technological progress in FIB has concentrated on refining system equipment, such as ultra-precision stages, controlled environments, and feedback mechanisms for optimizing material removal and deposition rates. FIB technology's remarkable flexibility, resolution, precision, and cost-effectiveness establish it as a prominent player in the field of nanofabrication. Particularly, among the four FIB direct writing techniques, ion-assisted etching (FIBAE) stands out as the most efficient, boasting a processing rate approximately one order of magnitude faster than the other three processes. In sum, FIB technology's evolution has empowered it to fabricate intricate nanoscale structures with unparalleled accuracy and efficiency, making it a pivotal player in the realm of academic and industrial nanofabrication [81].

EBL and FIB fabrication techniques have their advantages and disadvantages. EBL can be contaminated by residual resist or solvents, while FIB can damage the sample and reduce product quality. EBL is faster for large-area lithography, while FIB is faster for single antenna or small antenna fields [82]. The main deference of these two fabrication techniques are presented in figure 3.9.

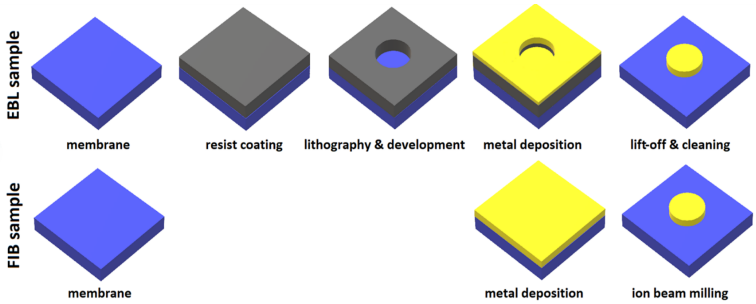

Figure 3.9: Schematic stages of EBL and FIB fabrication techniques[82].

Nanoimprint lithography

The first time the idea of Nanoimprint was discussed in 1996 by [83], then the phrase nanoimprint lithography was coined in the scientific literature and developed by the same researcher Stephen Y. Chou and his team in [84] and [85]. in 2004 They have developed this technique to rich 5 nm linewidth and 14 nm pitch [86].

A mold is pressed into a low viscosity photocurable resist liquid in photocurable nanoimprint lithography (P-NIL) as shown in figure 3.10 to physically bend the resist shape such that it conforms to the topology of the mold. The resist is cured by exposing it to UV radiation, which crosslinks the various components of the resist liquid, resulting in a uniform, moderately hard polymer network. After that, the mold is detached from the cured resist. Finally, an anisotropic reactive ion etch (RIE) is used to remove the leftover resist in the compressed area, revealing the substrate surface.

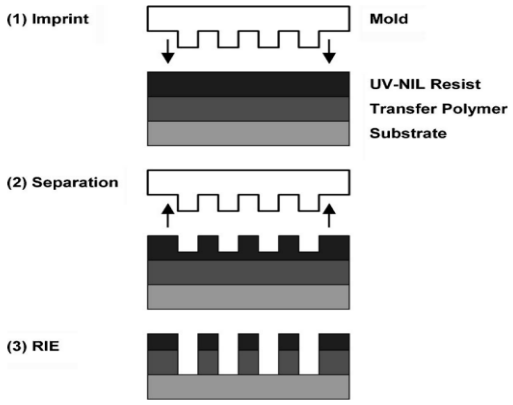

(a)

Figure 3.10: Schematic stages of NIL fabrication process[86].

3.5.2 Nonlithographic Techniques

Solid state dewetting

In its initial deposited state, thin films typically exist in a metastable condition, demonstrating a tendency to undergo dewetting or agglomeration, forming arrays of islands upon exposure to heat as depicted in figure 3.11. Notably, this process can transpire well before the film reaches its melting temperature, resulting in dewetting, or agglomeration, while the film remains in a solid state. The underlying impetus driving dewetting lies in the imperative to minimize the overall energy associated with the free surfaces of both the film and the substrate, as well as the film-substrate interface. Importantly, this driving force intensifies with diminishing film thickness, thereby accelerating the rate of dewetting. Consequently, the temperature at which dewetting occurs decreases in tandem with reductions in film thickness [87].

The challenge of dewetting in thin films has been a persistent issue for manufacturers of integrated circuits and various microsystems. Specific attention has been directed towards addressing dewetting in metal silicides and silicon-on-insulator (SOI) structures, prompting extensive research endeavors to understand and mitigate this phenomenon. The repercussions of dewetting extend beyond these systems, affecting the reliability of other microdevices and systems, particularly in scenarios demanding high-temperature operation [87].

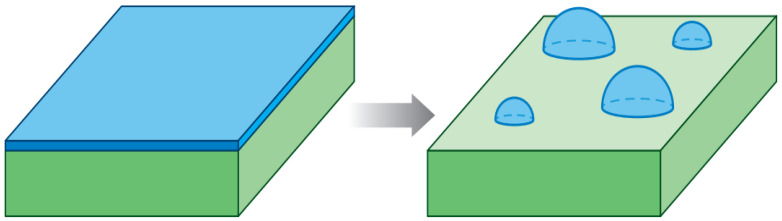

(a)

Figure 3.11: Fabrication schematic stages of SSD process[87].

Magnetron sputtering technique

In the foundational sputtering technique, a target plate (or cathode) undergoes bombardment from energetic ions produced within a glow discharge plasma positioned in front of the target. This bombardment results in the removal, or sputtering, of target atoms, which then condense onto a substrate, forming a thin film see figure 3.12. Additionally, secondary elec-

trons are emitted from the target surface due to ion bombardment, playing a pivotal role in sustaining the plasma. Although the basic sputtering process has a long-established history and has successfully deposited a variety of materials, it faces limitations such as low deposition rates, sub-optimal ionization efficiencies in the plasma, and heightened substrate heating effects. To overcome these challenges, advancements in sputtering techniques, particularly magnetron sputtering and more recently, unbalanced magnetron sputtering, have been developed [88].

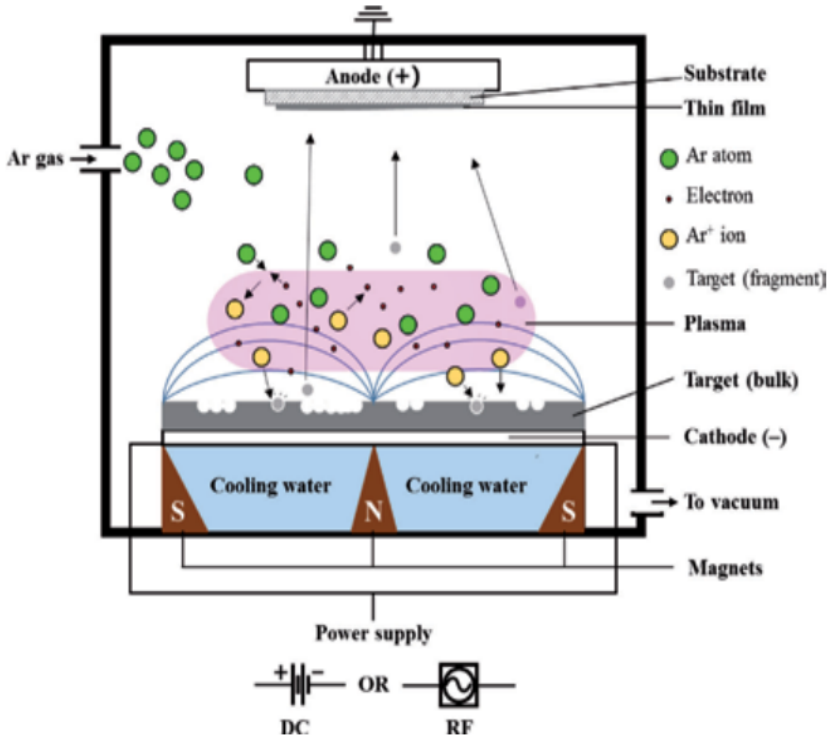

(a)

Figure 3.12: Illustration depicting a magnetron sputtering equipment and the associated deposition process[89].

3.6 Application of nanotechnology

In the realm of forefront scientific advancements, the fusion of nanotechnology with photonics and plasmonics has created a captivating domain with significant potential to transform how we capture and control light. The convergence of these disciplines sets the stage for a intricate interplay among tiny structures and materials, enabling novel opportunities in information processing, sensing, and imaging that were previously unexplored.

Nanotechnology, which involves working with incredibly tiny particles, gives us the tools to create materials and devices at an incredibly small scale about a billionth of a meter. In the world of photonics and plasmonics, this means we can design structures that have the remarkable ability to confine and manage light with incredible accuracy.

Nanotechnology finds diverse applications across various industries figure(3.13). In electronics, it enables the development of smaller and more efficient components. In energy production, nanomaterials enhance solar cell efficiency and contribute to advanced energy storage. Nanotechnology enhances textiles, creating fabrics with improved durability and functionality. In sports, nanomaterials are used to manufacture lightweight and high-performance equipment. Diagnostic techniques benefit from nanoscale tools for more accurate and sensitive testing. Drug delivery systems leverage nanoscale carriers for targeted and controlled release. Cosmetics incorporate nanoparticles for improved product performance. In paints and varnishes, nanotechnology enhances durability and protective qualities. Nanomaterials are employed in stain-resistant coatings, enhancing product longevity. These applications highlight the versatility and impact of nanotechnology in various sectors.

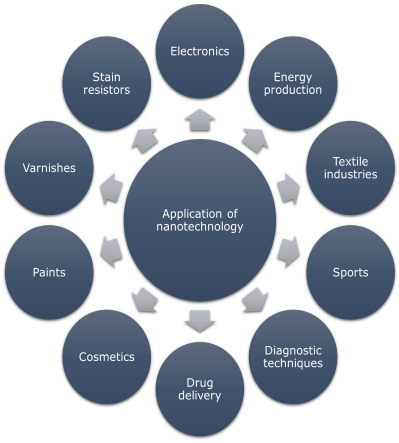

Figure 3.13: Applications of nanotechnology.

3.7 Non linear optics

Nonlinear optics delves into phenomena triggered by changes in a material's optical properties induced by intense light, typically from lasers. The field's origin is often linked to the 1961 discovery of second-harmonic generation by Franken, Hill, Peters and Weinreich [90], following Maiman's debut of the first laser in 1960 [91]. Nonlinear optical effects earn the "nonlin-

ear" tag as they emerge when a material's response to light behaves in a non-straightforward manner concerning the field's strength. For instance, second-harmonic generation arises from an atomic response that scales not linearly but quadratically with the optical field's intensity. This results in the light generated at the second-harmonic frequency increasing in intensity squared relative to the applied laser light [92].

In the linear systems, the induced polarization exhibits a linear dependence on the magnitude of the electric field, which can frequently be characterized by the relation:

$$\tilde{P}(t) = \varepsilon_0 \chi^{(1)} \tilde{E}(t) \tag{3.4}$$

where ϵ_0 is the permittivity of free space and $\chi^{(1)}$ is the linear susceptibility.

In the nonlinear optics, Equation 3.4 can be espressed as a power series in the field strength $\tilde{E}(t)$ as:

$$\begin{aligned} \tilde{P}(t) &= \varepsilon_0 \left[\chi^{(1)} \tilde{E}(t) + \chi^{(2)} \tilde{E}^2(t) + \chi^{(3)} \tilde{E}^3(t) + \cdots \right] \\ &\equiv \tilde{P}^{(1)}(t) + \tilde{P}^{(2)}(t) + \tilde{P}^{(3)}(t) + \cdots \end{aligned} \tag{3.5}$$

where $\chi^{(2)}$ and $\chi^{(3)}$ are the second and third nonlinear susceptibilities. The tilde ($\sim$) is used to denote that these quantities varies rapidly in time and constant quantities or Fourier amplitudes or slowly varying quantities can be written without it [92].

3.7.1 Second-harmonic generation

Let us examine the second-harmonic generation process, which is schematically depicted in figure 3.14, as an illustration of a nonlinear optical interaction. The process of second harmonic generation can be described by Equation 3.6:

$$\tilde{P}^{(2)}(t) = \varepsilon_0 \chi^{(2)} \tilde{E}^{(2)}(t) \tag{3.6}$$

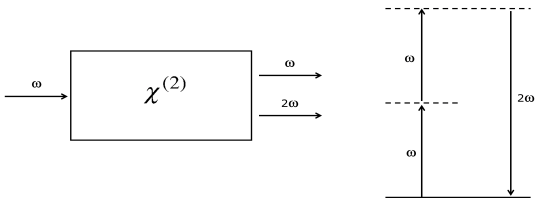

Figure 3.14: Geometry and energy-level diagram describing second-harmonic generation[92].

Nearly all of the power in the incident beam at frequency ω can be transformed to radiation at the second-harmonic frequency 2ω by the use of an efficient second-harmonic generation process, provided that the right experimental circumstances are met. A popular application of second-harmonic generation is to change the spectral region of a fixed-frequency laser's output [92].

Sum-Frequency Generation

In the Sum-Frequency Generation the nonlinear polarization describing the process is given by:

$$P(\omega_1 + \omega_2) = 2\varepsilon_0 \chi^(2) E_1 E_2 \tag{3.7}$$

This process is illustrated in figure 3.15

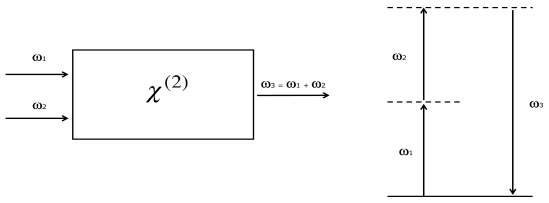

Figure 3.15: Geometry and energy-level diagram describing sum-frequency generation[92].

In numerous respects, the mechanism underlying sum-frequency generation bears resemblance to that of second-harmonic generation. The key distinction lies in the fact that, in sum-frequency generation, the two input waves are characterized by disparate frequencies. An illustrative application of sum-frequency generation involves the generation of tunable radiation within the ultraviolet spectral domain. This is achieved by designating one of the input waves as the output emanating from a fixed-frequency visible laser, while the other wave originates from a frequency-tunable visible laser [92].

Difference-Frequency Generation

Difference-Frequency Generation process is illustrated in figure 3.16
and can be described by a non linear polarization of the form:

$$P(\omega_1 - \omega_2) = 2\varepsilon_0 \chi^{(2)} E_1 E_2^* \tag{3.8}$$

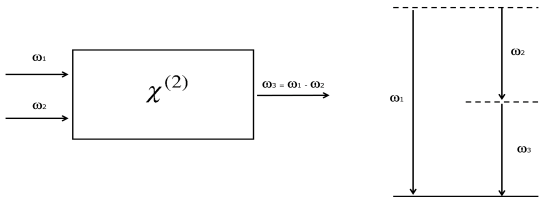

Figure 3.16: Geometry and energy-level diagram describing difference-frequency generation[92].

In this particular circumstance, it is crucial to mention that the frequency of the wave that is created is directly connected to the discrepancy between the frequencies of the applied fields. It is worth mentioning that the phenomenon known as difference-frequency generation demonstrates the capability to generate infrared radiation that can be tuned according to specific requirements. This is attained by combining the outcome of a visible laser that can be adjusted in terms of frequency with the outcome of another visible laser that has a fixed frequency [92].

3.7.2 Third-harmonic generation

The process of the third-harmonic generation is described in figure 3.17 and can be mathematically described by :

$$\tilde{P}^{(3)}(t) = \varepsilon_0 \chi^{(3)} \tilde{E}^{(3)}(t) \tag{3.9}$$

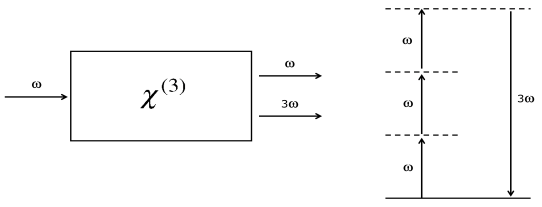

Figure 3.17: Geometry and energy-level diagram describing third-harmonic generation[92].

One widely employed application of third harmonic generation (THG) is in the field of biomedical imaging, particularly in multiphoton microscopy. In this context, THG serves as a valuable tool for label-free imaging of biological tissues with high spatial resolution. By utilizing three input photons to generate a single photon at triple the frequency, THG enables researchers to visualize cellular structures and dynamics without the need for exogenous contrast agents. This has significant implications for studying biological samples, as it minimizes potential interference with natural cellular processes and provides detailed insights into tissue morphology. Multi-photon microscopy employing THG has found applications in various areas, including neuroscience, where it facilitates the non-invasive imaging of live brain tissues and cellular structures, contributing to advancements in our understanding of complex biological systems.

3.8 Conclusion

In conclusion, our exploration in this chapter has navigated the intricate landscape of plasmonic structures, covering their simulation, modeling, fabrication, and applications in the captivating realm of nanotechnology. The indispensable role of simulation software platforms like COMSOL and Lumerical has allowed us to virtually unravel the complexities of plasmonic systems, offering a dynamic and comprehensive approach to understanding their behaviors. These tools empower researchers to gain profound insights into the nuanced dance between electromagnetic fields and metallic nanostructures, providing a robust foundation for fine-tuning design parameters. Moreover, our journey through various modeling techniques has not only unraveled the theoretical underpinnings of plasmonic phenomena but has also illuminated the path toward a deeper comprehension of the captivating interplay at the nanoscale. On the fabrication front, the artistry of creating plasmonic structures has advanced remarkably, granting us precise control over their geometry and material composition through sophisticated nanofabrication techniques. This not only ensures reproducibility but also sparks the imagination for tailoring plasmonic properties to cater to specific applications. As nanotechnology continues to evolve, the applications of plasmonic structures in diverse fields such as sensing, imaging, and energy harvesting are poised to make profound impacts, underscoring the significance of ongoing research endeavors in this burgeoning interdisciplinary field.

Chapter 4

Result and Discussion

4.1 Introduction

As we delve into the conclusion of this thesis, we embark on a detailed exploration of the results derived from our meticulous study on plasmonic basic filters and demultiplexers. Rooted in the Metal-Insulator-Metal (MIM) structural paradigm and leveraging the Drude model with silver as the chosen metal, our investigation centers around Surface Plasmon Polaritons (SPP) in the infrared (IR) region, spanning from 0.8 to 2 micrometers.

The fundamental motivation driving our research lies in the quest for sophisticated optical communication and signal processing solutions. The utilization of plasmonic structures, particularly those based on MIM configurations, harnesses the extraordinary capabilities of Surface Plasmon Polaritons. These subwavelength phenomena afford us the ability to confine and manipulate light, thereby offering promising avenues for the development of compact and efficient devices operating in the IR spectrum.

Within this chapter, the culmination of our efforts manifests in a comprehensive examination of the empirical results obtained through extensive experimentation and analysis. Key parameters such as spectral characteristics, transmission efficiency, and the capacity for signal demultiplexing take center stage as we unravel the intricacies of our designed plasmonic structures.

The chosen metal, silver, characterized by the Drude model, has been instrumental in shaping the optical properties of our MIM-based devices. The spectral region of interest, extending from 0.8 to 2 micrometers, is strategically selected to align with the IR spectrum, where these plasmonic filters and demultiplexers find applicability in diverse technological domains.

Our empirical findings offer a nuanced perspective, showcasing not only the theoretical predictions but also the practical implications of our plasmonic devices. As we navigate through the results, it becomes evident that the performance enhancements achieved through systematic design parame-

ter variations hold significant promise for advancing optical communication technologies, especially in the specified IR regime.

Moreover, this chapter serves as a platform to elucidate the broader implications of our work. By presenting the challenges encountered and lessons learned throughout the course of our research, we contribute valuable insights to the evolving landscape of plasmonics, particularly in the context of MIM structures, Drude model-based silver, and SPPs operating in the IR spectrum.

In essence, this concluding chapter encapsulates the essence of our journey, revealing the potential and limitations of our plasmonic basic filters and demultiplexers. Through empirical evidence and theoretical understanding, we provide a meaningful contribution to the field, shaping the discourse on plasmonics in the domain of IR-based optical communication and signal processing.

4.2 Basic filter design, four and eight plasmonic DEMUX based on rectangular resonator

A new plasmonic demultiplexer (DEMUX) featuring four and eight channel outputs was developed by integrating rectangular resonators with a metal-insulator-metal plasmonic waveguide. By situating the output port adjacent to the rectangular resonator, the desired wavelength is extracted from the combined wavelengths. The wavelength obtained at the output ports is contingent on the width of the rectangular resonators. In this design, silver and air serve as the metal and insulator layers, respectively, with the silver's permittivity modeled using the Drude model. The proposed structures were investigated numerically using the finite element method. The fundamental plasmonic filter utilized in the DEMUX design is a single-mode filter. Results indicate that our proposed DEMUXs exhibit a Q-factor averaging 81.08 and 101.93 for the 4 and 8 output channels, respectively, with low full width at half maximum (FWHM) values of 9.625 nm and 8.9 nm, respectively. Given the number of outputs (particularly for an eight-channel configuration) and the compact dimensions of the proposed DEMUXs, they demonstrate potential utility in integrated optical circuits for communication applications.

4.2.1 Basic filter design

In telecommunication systems, the preference often leans towards having a single-mode filter, yet many plasmonic resonators exhibit multimode responses. Overcoming this challenge involves adjusting cavities in specific ways, although such modifications may hinder the absorption and transmission of incident power, resulting in lower transmission efficiency. Addition-

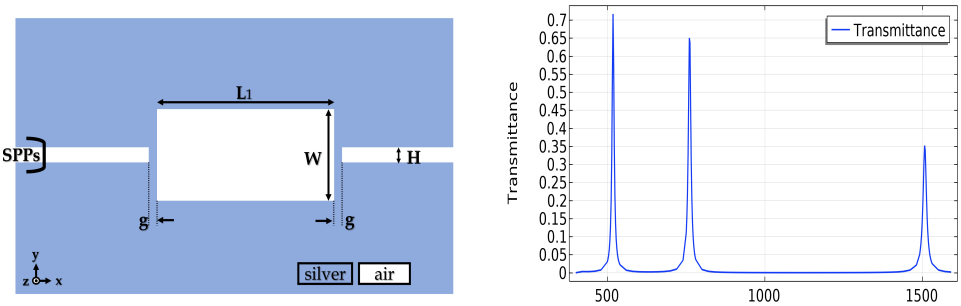

(a) (b)

Figure 4.1: Basic filter (a) design and (b) transmission spectrum.

ally, issues arise in selectivity; even when achieving good transmission rates, some filters may experience an undesirably large full width at half maximum (FWHM), exceeding 50 or 100 nm. This poses a concern in telecommunication systems where spectrum efficiency is crucial, and any inefficiency could translate to financial implications. The initial design of the basic filter centers around a nano-rectangular cavity, as detailed in figure 4.1(a). This particular cavity exhibits three distinct modes, as illustrated in figure 4.1(b). To address the multimode characteristics inherent in this cavity, a meticulous examination of the field profiles associated with each mode was conducted.

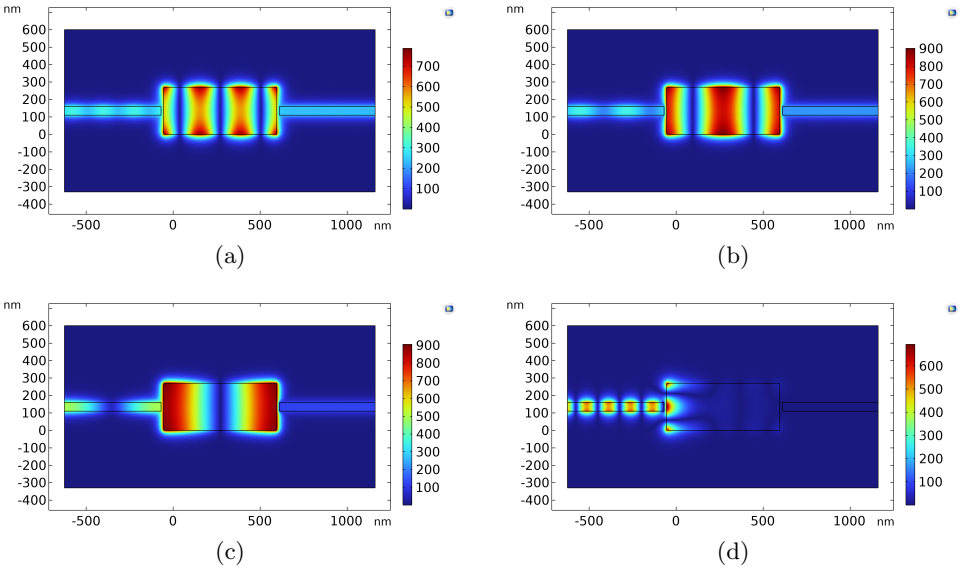

(a) (b)

(c) (d)

Figure 4.2: Filed profile of resonant wavelengths (a) $\lambda = 520$ nm (b) $\lambda = 761.5$ nm (c) $\lambda = 1500$ nm and (d) non-resonant wavelengths.

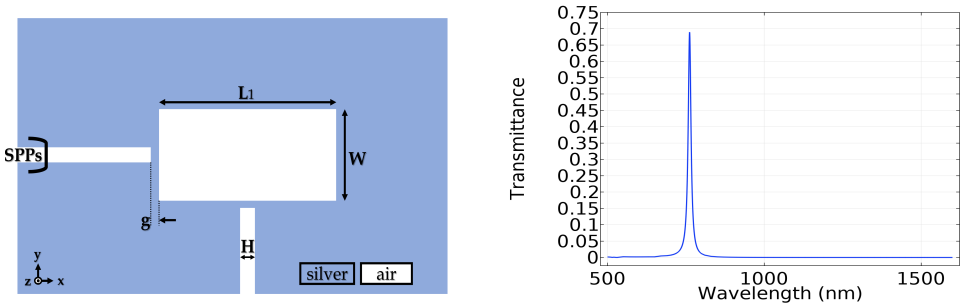

(a) (b)

Figure 4.3: Mono-mode basic filter (a) design (b) transmission spectrum.

The objective was to identify an optimal location for the output waveguide that introduces a deliberate mismatch between the field profile and the output waveguide.

The field profile was subjected to detailed scrutiny to strategically position the output waveguide for maximal effectiveness in generating a mismatch with the field profile of other resonant wavelengths. This strategic placement is perceptible in both figure 4.2(a) and (c), where the field profiles reveal a distinctive central portion of empty space within the cavity.

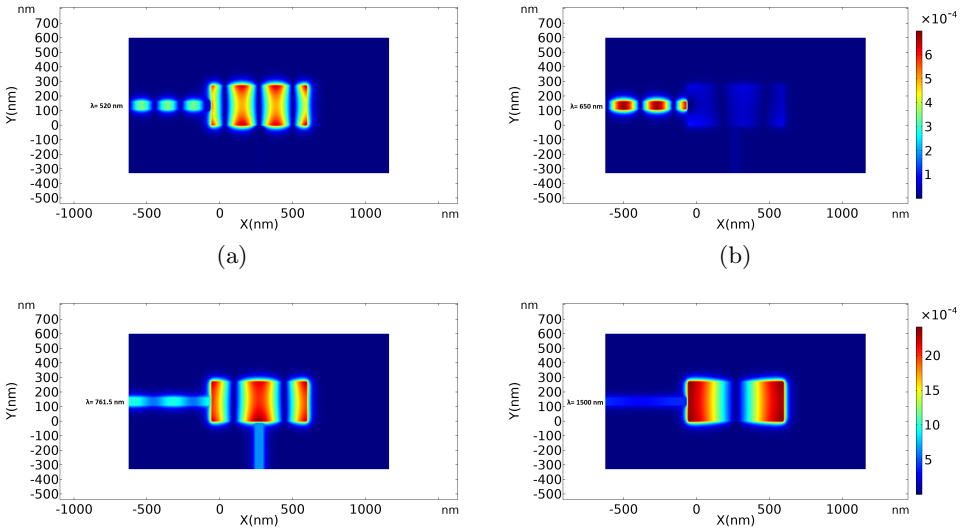

(a) (b)

(c) (d)

Figure 4.4: Profile of the magnetic field $|Hz|$ at both resonance and non-resonance wavelengths (a) $\lambda = 520$ nm; (b) $\lambda = 650$ nm; (c) $\lambda = 761.5$ nm; (d) $\lambda = 1500$nm; for the primary filter.

This spatial feature serves as an opportune location for inducing the desired mismatch, ensuring that only the field profile of 4.2(b) is transmitted to the output waveguide.

This strategic placement ensures that only a singular resonant wavelength is transmitted to the output port. Remarkably, this design achievement is realized without the incorporation of supplementary materials or slabs, thereby avoiding potential impacts on transmission efficiency or the full width at half maximum (FWHM). The resulting configuration represents the inaugural monomode basic filter design.

The mono-mode basic filter design represented in figure 4.3(a), is the first mono-mode filter discussed in this thesis, this filter has one resonant wavelength at $\lambda = 761.5$ nm as shown in figure 4.3(b), with a transmission of 69% and FWHM of 11nm; it is well seen that the output port is on the middle bottom side of the cavity to create the mismatch with the field profile of the other resonant wavelengths, the geometrical parameters are crucial and any change can effect the outlets, for the length of the rectangular cavity $L_1 = 650$, the width $W = 270$, the gap between the waveguides and the cavity is $g = 15$ and the width of the waveguides is set $H = 50$, all in nm. The white areas are assumed to be air and the blue areas are silver, the relative permittivity of the silver is characterized by the Drude model [93]:

$$\varepsilon_m = \varepsilon_\infty - \frac{\omega_p^2}{\omega(\omega + i\gamma)} \tag{4.1}$$

The relative permittivity in high frequency $\varepsilon_\infty = 3.7$, the plasma frequency $\omega_p = 1.38 \times 10^{16}$ Hz, the damping frequency $\gamma = 2.73 \times 10^{13}$ Hz and the angular frequency is set to be ω.

We employed a predetermined highly refined mesh size in the insulator (air) layer, with a minimum size of 0.098 nm. Simultaneously, we utilized a predefined standard size in the metal layer, setting a minimum mesh size of 1.47 nm. Notably, we opted for different meshing sizes across the entire geometry, considering the significantly longer surface plasmon polaritons (SPPs) in the dielectric medium. This choice aimed to minimize processing time and concentrate on interactive zones. Additionally, a numeric port was applied to both the input port and all output ports, employing boundary mode analyses for each.

The filed profile of the basic filter design of resonance and non resonance wavelengths are shown in figure 4.4, In figure 4.4(a), (c) and (d) it is evident that the rectangular cavity exhibits three resonance wavelengths at $\lambda_a = 520$ nm, $\lambda_c = 761.5$ nm, and $\lambda_d = 1500$ nm. However, resonance wavelengths in the rectangular cavity are obstructed for λ_a and λ_d due to a mismatch with the field profile and the output waveguide. Consequently, only λ_c is able to pass through the output port. Figure 4.4(b) illustrates that non-resonance wavelengths are unable to propagate to the rectangular cavity.

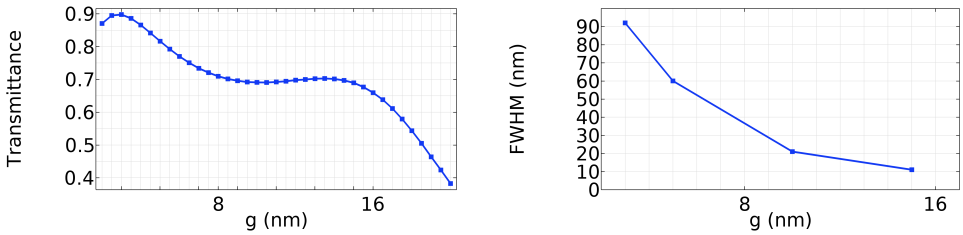

(a) (b)

Figure 4.5: The gap g effectiveness on (a) the transmission and (b) the selectivity.

The geometric parameters in plasmonic structures plays a crucial role in the outlets of the system, for that we have studied the geometrical parameters carefully to obtain the optimal results. Figure 4.5(a), shows the variation of the transmission with the variation of the gap (g) between the waveguides and the resonance cavity, we have changed the gap from $2 < g < 20$nm with 0.5 nm steps, while Figure 4.5(b) describe the effect on the FWHM according to the changes of the gap (g). When the parameter g is set to 3 nm, the transmission peak reaches its maximum value of 89.75%, but the full width at half maximum $FWHM = 70$ nm. Consequently, we opt for g = 15 nm as it yields a narrower FWHM of 11 nm while maintaining a reasonable transmission peak of 69%.

The change of the length and the width of the resonance cavity leads to a red or a blue shift of the transmission spectrum, which can be used as a parameter to obtain different transmission spectrum in the visible and near infrared spectrum.The variations in width do not exhibit consistent changes compared to the length. To achieve optimal control over dimensions, we establish a fixed width and adjust the length to induce shifts; As illustrated in figure 4.6, the sweeping of 10 nm of L_1 to a higher value gives a red-shifted transmission by 10.5 nm.

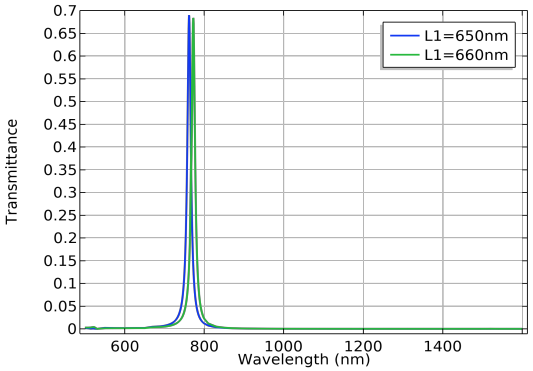

Figure 4.6: The transmission spectrum shift by the length.

This design and strategic results in single mode filter at $\lambda = 761.5$ nm, a transmission of $T_r = 69\%$ and selectivity of $FWHM = 11$ nm between visible and near-infrared (NIR) spectrum $0.5\mu m < \lambda < 1.6\mu m$.

4.2.2 Four channel demultiplexer

We used the predefined single mode filter to design four channel output $DEMUX$, obviously we used four resonant cavities for each wavelength, in addition to a T-shaped waveguide to connect them to the same input as shown in figure 4.7. The geometrical parameter are as follow: $L_1 = 650, L_2 = 660, L_3 = 670, L_4 = 680, L_5 = 690, L_6 = 700, L_7 = 710, L_8 = 720, W = 270, g = 15, H = 50, a_1 = 1470, a_2 = 2137, b_1 = 345, b_2 = 345, b_3 = 355, b_4 = 355, c_1 = 227.5, c_2 = 227.5, c_3 = 200, c_4 = 257.5, c_5 = 245, c_6 = 245, c_7 = 200$ and $c_8 = 245$, all in nm.

The resonance wavelengths are $\lambda_1 = 762\,\text{nm}$, $\lambda_2 = 772.5\,\text{nm}$, $\lambda_3 = 783.2\,\text{nm}$, $\lambda_4 = 793.8\,\text{nm}$, corresponding to maximum transmission peaks of 59.17%, 53.4%, 55.4%, and 56.04%, respectively. The full width at half maximum (FWHM) values are 10.5 nm, 9 nm, 9.5 nm, and 9.5 nm, respectively. The channel spacing is 10.5 nm, 10.7 nm, and 10.6 nm, and the Q-factors are 72.57, 85.84, 82.44, and 83.47, respectively.

When designing a DEMUX, it's crucial to think about Crosstalk. Crosstalk is like the interference or influence that nearby channels can have on the channel we actually want, especially when we're sending an optical wave into the input of the demultiplexer (DEMUX). Table 4.1 represent the values of the Crosstalk calculated using the formula $10 \times log\frac{p_{low}}{p_{high}}$ [94].

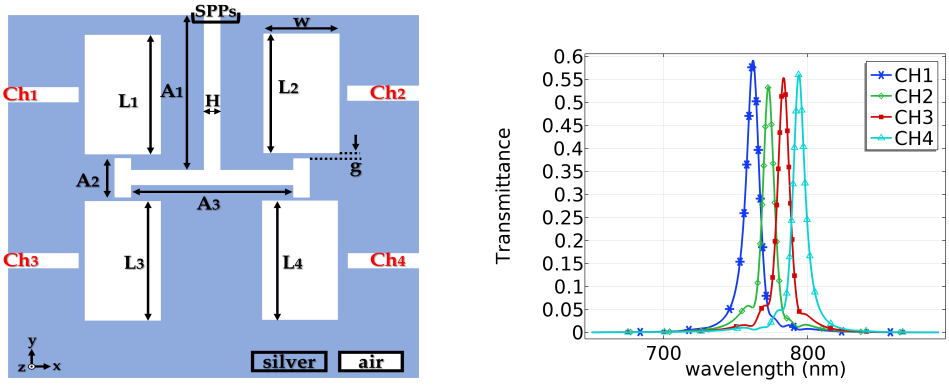

(a) (b)

Figure 4.7: (a)Schematic diagram of the four channel DEMUX and its (b) transmission spectrum.

$Crosstalk(dB)$	CH_1	CH_2	CH_3	CH_4
CH_1	\	-10.31	-15.95	-19.26
CH_2	-10.28	\	-9.49	-15.81
CH_3	-15.96	-11.19	\	-10.45
CH_4	-19.7	-16.69	-10.85	\

Table 4.1: Crosstalk values of the 4-output DEMUX.

In figure 4.8, we investigate what happens when we systematically varied A_1, A_2, and A_3 in our setup. Surprisingly, A_1 doesn't do much unless it's less than 950 nm, and we decide to set it at 1000 nm to avoid issues. When we tweak A_2 between 200 and 600 nm, things get interesting. Turns out, the transmission peaks at its best when A_2 hits 505 nm for all the outputs. Then, we play around with A_3 between 400 and 800 nm, and the best spot for the best results is when A_3 is 640 nm.

In figure 4.9, you can see how the field looks for the resonance wavelengths. Basically, it shows that most wavelengths are blocked, except for those chosen ones at 762 nm, 772.5 nm, 783.2 nm, and 793.8 nm. These special ones manage to pass through to channels Ch_1, Ch_2, Ch_3, and Ch_4.

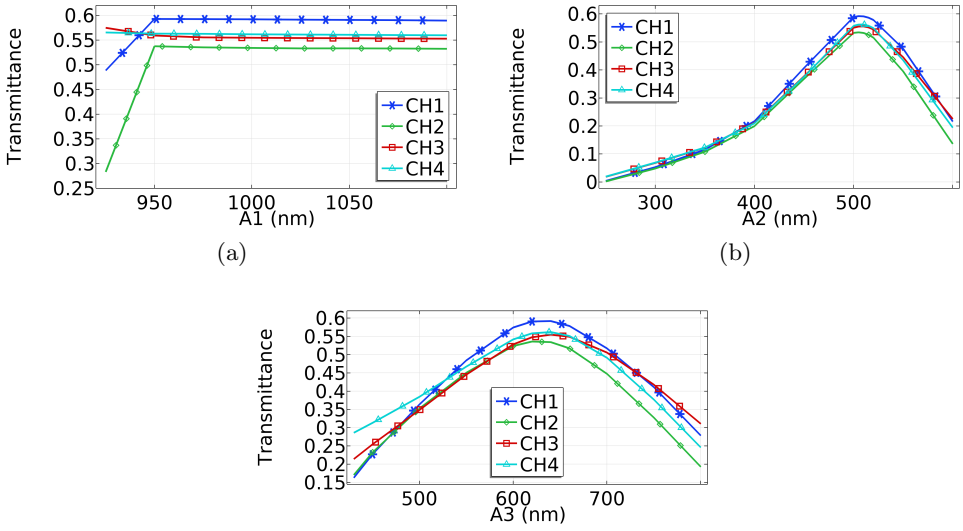

Figure 4.8: (a) A_1; (b) A_2; (c) A_3; effect on the transmission spectra.

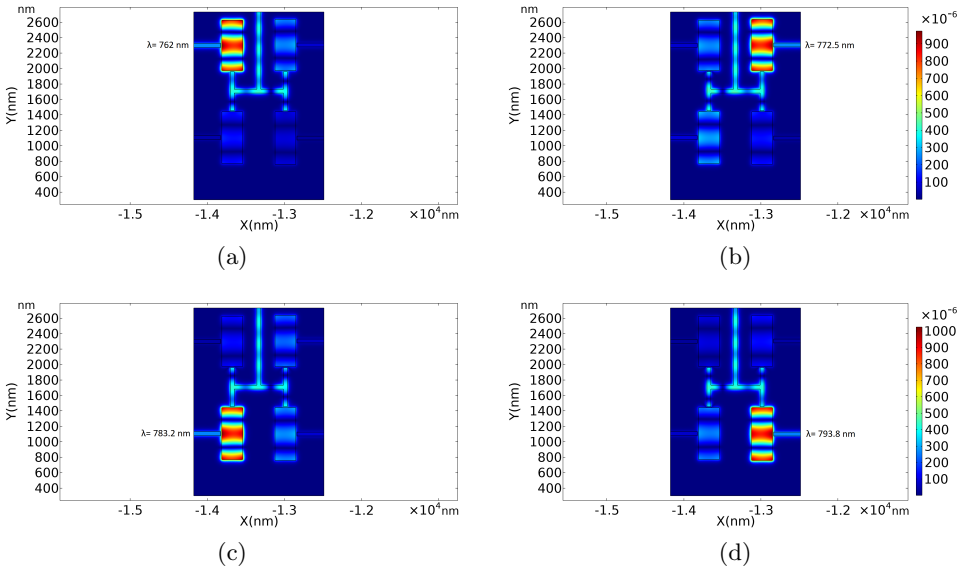

Figure 4.9: The four channel DEMUX field profile: (a) $\lambda = 762.5$ nm; (b) $\lambda = 772.5$ nm; (c) $\lambda = 783.2$ nm; (d) $\lambda = 793.8$ nm.

4.2.3 Eight channel demultiplexer

An eight plasmonic DEMUX was proposed based on the basic filter as seen in figure 4.10(a), the structural parameters are $L_1 = 650$; $L_2 = 660$; $L_3 = 670$; $L_4 = 680$; $L_5 = 690$; $L_6 = 700$; $L_7 = 710$; $L_8 = 720$; $W = 270$; $g = 15$; $H = 50$; $a_1 = 1470$; $a_2 = 2137$; $b_1 = 345$; $b_2 = 345$; $b_3 = 355$; $b_4 = 355$; $c_1 = 227.5$; $c_2 = 227.5$; $c_3 = 300$; $c_4 = 257.5$; $c_5 = 245$; $c_6 = 245$; $c_7 = 200$; $c_8 = 245$; all in nm.

The transmitted resonance wavelengths for Channels 1 to 8 are as follows: $\lambda_1 = 761, \text{nm}, \lambda_2 = 771.5, \text{nm}, \lambda_3 = 782.5, \text{nm}, \lambda_4 = 793, \text{nm}, \lambda_5 = 805, \text{nm}, \lambda_6 = 814.5, \text{nm}, \lambda_7 = 825, \text{nm}, \lambda_8 = 835, \text{nm}$. The corresponding maximum transmission peaks are 47.35%, 47.81%, 45.83%, 46.08%, 37.58%, 35.41%, 35.11%, and 26.91%, respectively. The full width at half maximum (FWHM) values are 10 nm, 9.5 nm, 9.5 nm, 11 nm, 8 nm, 7.5 nm, 8.5 nm, and 7.25 nm, respectively. The spacing between channels is 10.5 nm, 11 nm, 10.5 nm, 12 nm, 9.5 nm, 10.5 nm, and 10 nm, respectively as shown in 4.10(b); Cross-talk values are presented in table 4.2 The geometrical parameter effect on the transmission is shown in figure 4.11;

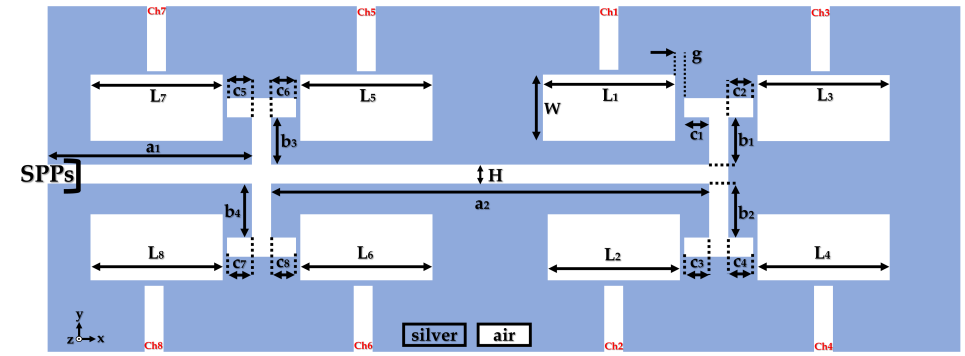

(a)

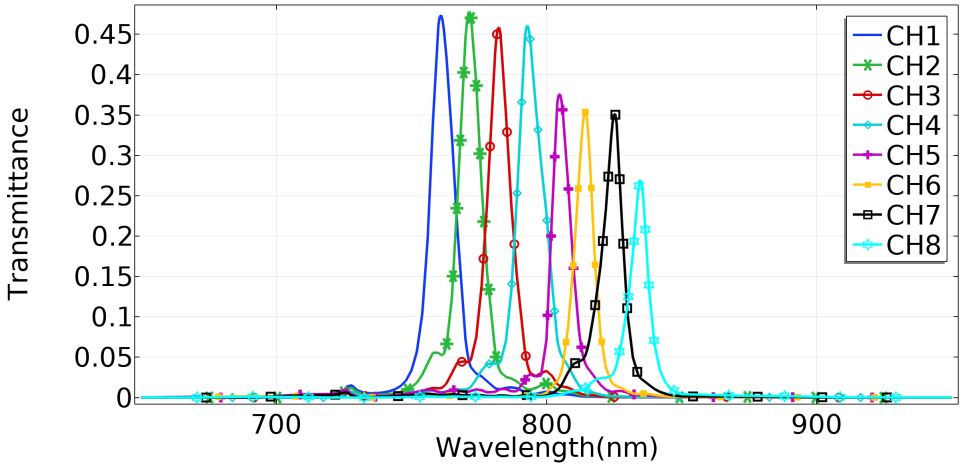

(b)

Figure 4.10: (a) Schematic and (b) transmission spectrum, of the eight channel DEMUX.

Cross-talk(dB)	CH_1	CH_2	CH_3	CH_4	CH_5	CH_6	CH_7	CH_8
CH_1	\	-9.76	-5.96	-16.97	-18.97	-23.74	-22.77	-26.75
CH_2	-10.35	\	-10.26	-16	-18.34	-23.78	-23.78	-26.79
CH_3	-16.61	-11.17	\	-10.38	-16.61	-22.63	-22.63	-26.61
CH_4	-10.64	-16.63	-10.61	\	-12.48	-19.64	-21.86	-26.63
CH_5	-18.75	-16.2	-13.98	-8.11	\	-11.43	-14.61	-19.72
CH_6	-25.49	-22.48	-19.47	-15.95	-9.36	\	-8.24	-14.7
CH_7	-25.45	-25.45	-25.45	-25.45	-17	-13.4	\	-10.4
CH_8	-31.28	-27.3	-27.3	-25.27	-19.53	-17.3	-10.5	\

Table 4.2: Cross-talk values for the 8-output DEMUX.

The impact of parameters (a_1) on transmission is minimal but significant for (a_2), particularly affecting $CH_1, CH_5, CH_6, CH_7, and CH_8$. Choosing $a_2 = 2100$ nm yields favorable transmission across channels. Parameters (b_1) and (b_2) significantly influence transmission for values exceeding 350 nm, and we select $b_{1,2} = 345$ nm for optimal transmission. Values of $b_{3,4}$ show less impact within the range $320nm < b_{3,4} < 370nm$, with most channels peaking at $b_{3,4} = 355$ nm. Analysis of (c) values reveals similar responses for (c_1) and (c_2), with $c_{1,2} = 227.5$ nm providing satisfactory transmission. The highest transmission peaks for (c_3) occur at 197.5 nm. To prevent $CH_{2,8}$ dropping below 15% for $c_4 < 150nm$ and $CH_{1,5}$ dropping below 12% for $c_4 = 300nm$, we choose $c_4 = 257.5nm$, ensuring CH_8 records a minimum of 20% transmission. Channels 5, 6, 7, and 8 exhibit consistent responses between 220 and 260 nm; hence, we set $C_{5,6,7,8} = 245$ nm for optimal results across all outputs.

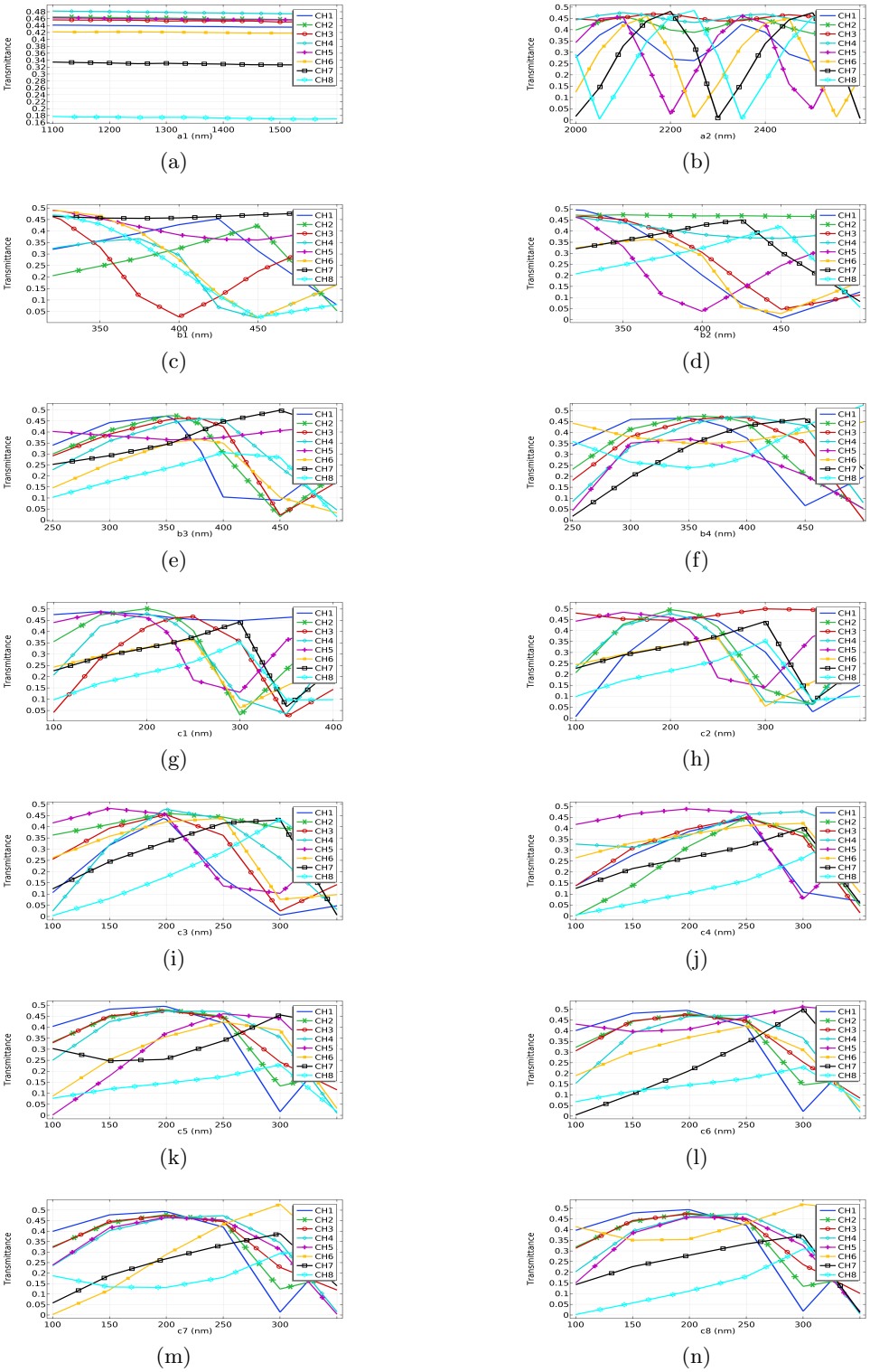

Figure 4.11: The geometrical parameter effect on the transmission spectra of the eight channel DEMUX.

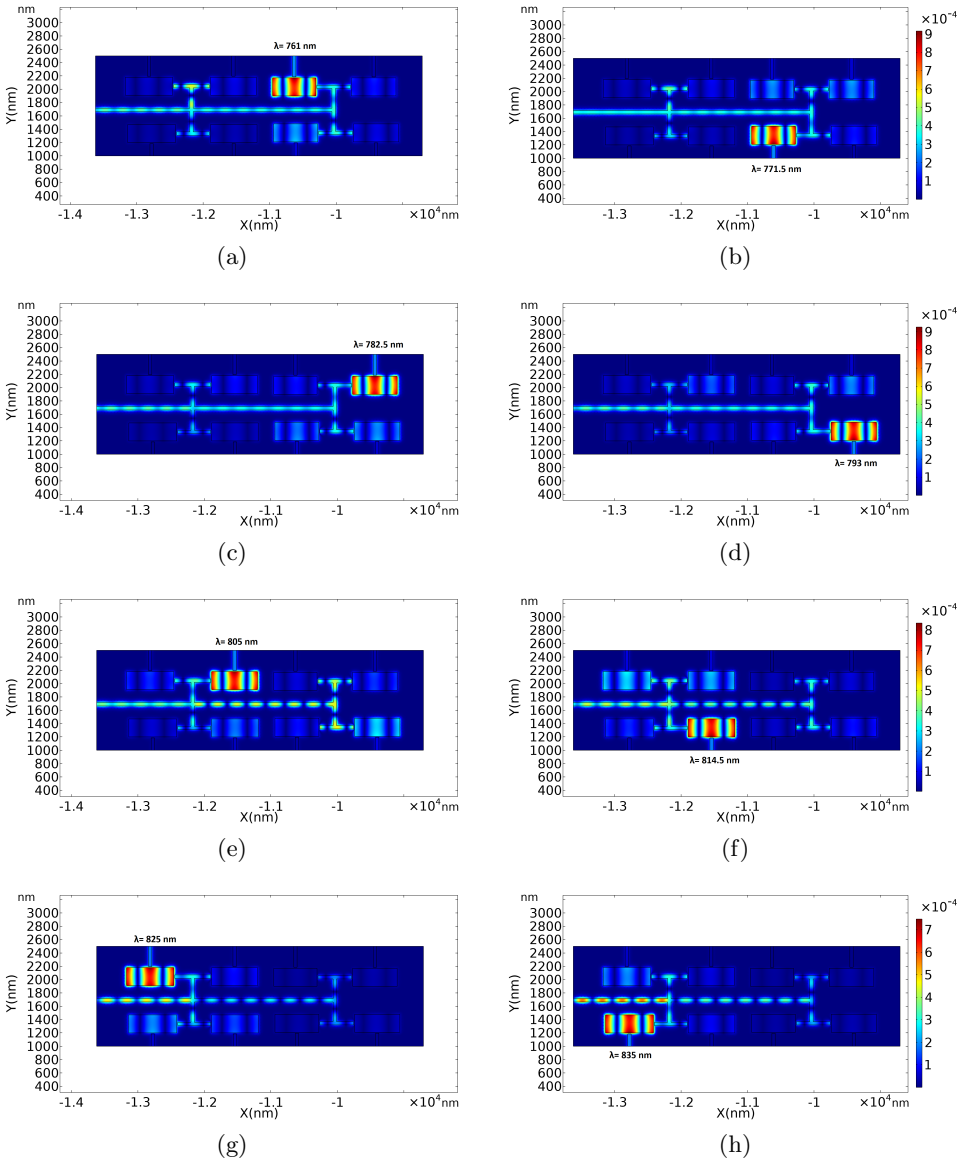

Figure 4.12: The field profile of the eight channel DEMUX.

The filed profile of the eight channels is presented in figure 4.12. As witnessed, all the resonance wavelengths appear in the rectangular cavities of the appropriate ones.

4.3 Basic filter design, four and eight plasmonic DEMUX based on nanodisk resonator

4.3.1 Basic filter design

The second basic filter is base on nanodisk resonator as shown in figure 4.13(a), the cavity is coupled with a T-shaped waveguide to the input, the geometrical parameters are as follow: w=50, A_s = 210, d=100, t=20 and g=15, all in *nm*. the same configuration of the metal is used as the in first structures. It is noticed from figure 4.13(b) that the transmission spectrum of the basic filter contain two modes at λ_1 = 525 nm and at λ_2 = 799 nm with 67.3% and 71.4% of transmission

To eliminate the wavelengths bellow λ = 600 nm, we get the idea of using a high pass filter that have the ability to block any wavelength bellow the cut-off frequency. we have used a high pass filter that is made of a loaded waveguide with multiple stubs wish act as a high pass filter.

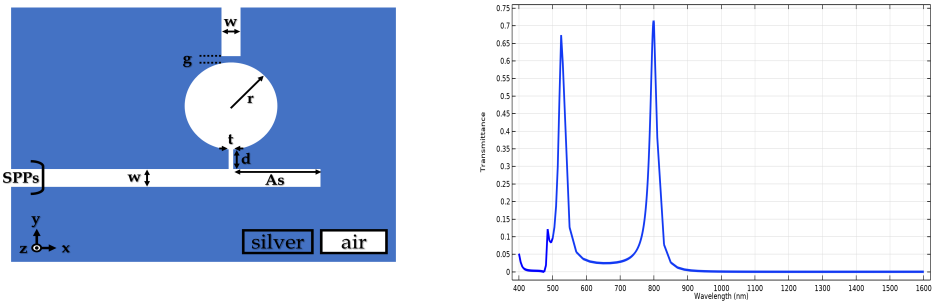

(a) (b)

Figure 4.13: (a) Proposed basic filter design, (b) its transmission spectrum.

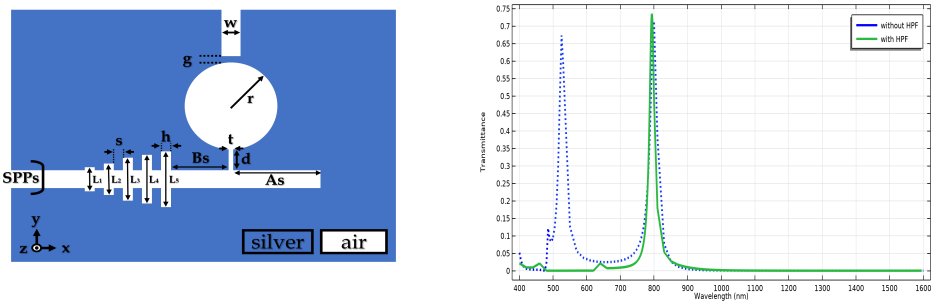

(a) (b)

Figure 4.14: (a) Proposed basic filter design with the HPF, (b) its transmission spectrum.

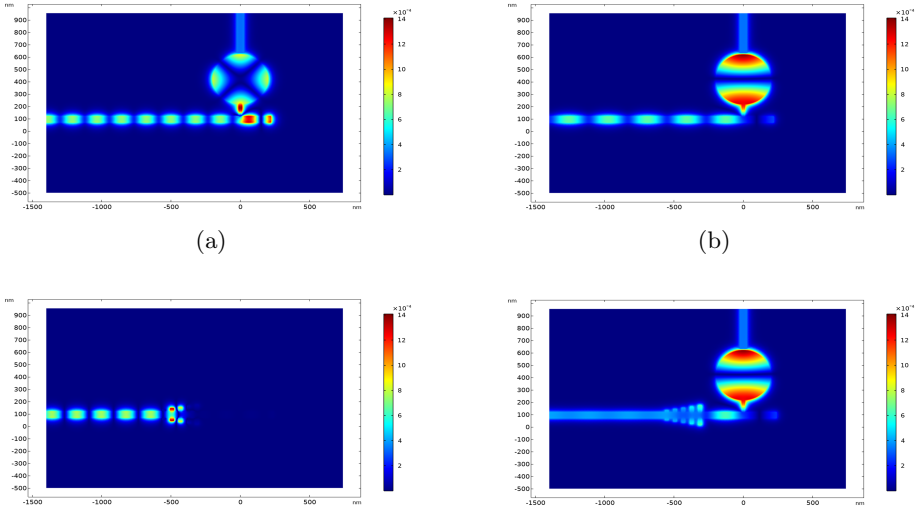

(a) (b)

(c) (d)

Figure 4.15: Filed profile of the basic filter with and without the HPF, (a)(c) $\lambda = 525nm$, (b)(d)$\lambda = 793nm$.

The use of such structure give the mono mode filter shown in figure 4.14(a) and its transmission spectrum in (b). we have add the HPF geometrical parameters: $B_s = 290$, $L_1 = 80$, $L_2 = 100$, $L_3 = 120$, $L_4 = 140$, $L_5 = 160$, $s = 35$ and $h = 25$, all in nm, to the multimode design. The use of the plasmonic HPF gives a 6 nm shift to the left and an increase of 2.1% of the transmission with a decrease in the FWHM from 25 to 19 nm wish resolve in a match better single mode filter. For better understanding the field profile of the basic filter design with and without the HPF is presented in figure 4.15.

The majority of geometrical parameters exhibit a straightforward impact on transmission spectra, while parameters A_s and B_s exert a pronounced

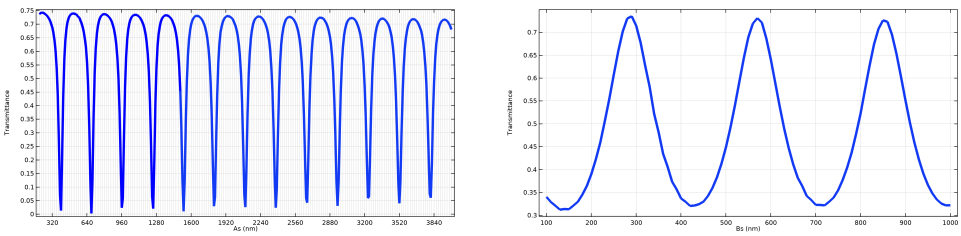

(a) (b)

Figure 4.16: The effect of (a) A_s, (b) B_s, values on the transmission spectra at $\lambda = 793nm$.

influence. Maintaining constant values for all other parameters, we systematically varied A_s from 200 to 4000 nm, revealing in figure 4.16(a) that transmission undergoes sinusoidal changes concerning A_s. This sinusoidal pattern implies that certain A_s values result in the highest transmission, while others yield close to zero transmission in a systematic fashion. This information guides the optimal placement of nanodisk resonators to achieve the best transmission spectrum. Subsequently, we varied B_s from 100 to 1000 nm, as depicted in figure 4.16(b). The response of B_s also exhibits a sinusoidal shape, reaching a peak of 73.5% and a nadir of 32%. Consequently, we select $A_s = 230$ nm and $B_s = 290$nm.

It is helpful to expand the basic filter design to four or eight channel DEMUXs since increasing the radii results in a red-shifted spectrum with little impact on transmission or FWHM.

4.3.2 Four channel DEMUX

To achieve the four channel demultiplexer four nano-disk resonator with different radii have been used based on the basic filter design figure 4.17(a). The geometrical parameter are as follow: $r_1 = 200$, $r_2 = 210$, $r_3 = 220$, $r_4 = 230$, w=50, $b_s = 300$, $L_1 = 80$, $L_2 = 100$, $L_3 = 120$, $L_4 = 140$, $L_5 = 160$, s=35, h=25, g=15, d=100, t=20, $As_1 = 200$, $As_2 = 180$, $As_3 = 1090$, $As_4 = 1400$, all in nm. Figure 4.17(b) demonstrate the transmission spectra of the four channel demultiplexer, as can be seen, there are four resonance wavelengths, $\lambda_1 = 794.5$ nm, $\lambda_2 = 827.5$ nm, $\lambda_3 = 863$ nm, $\lambda_4 = 897$ nm with maximum transmission of 72.48%, 67.29%, 59.47% and 63.43%, respectively. The channel spacing is 33 nm, 35.5 nm and 34 nm with a FWHM of 17.5 nm, 15.5 nm, 15 nm, and 13.5 nm, sequentially. The cross-talk values are presented in table 4.3.

The field profile $|H_z|$ corresponding to the resonance wavelengths is de-

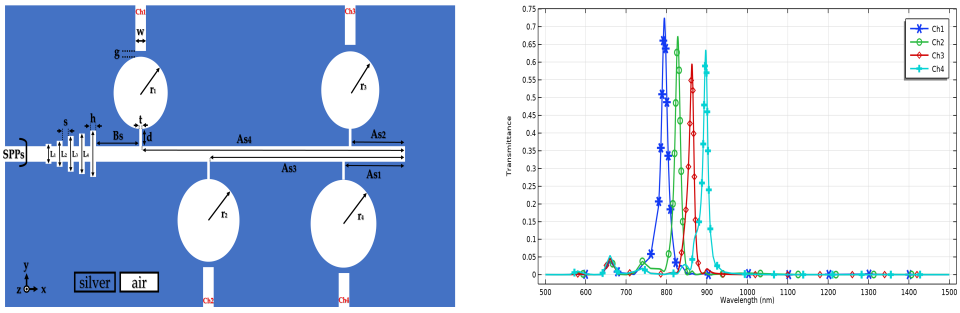

(a) (b)

Figure 4.17: (a) Proposed four channel DEMUX design, (b) it's transmission spectrum.

$Crosstalk(dB)$	CH_1	CH_2	CH_3	CH_4
CH_1	\	-18.6	-28.6	-28.6
CH_2	-16.37	\	-19.24	-22.83
CH_3	-22.97	-17.74	\	-12.06
CH_4	-25.01	-21.3	-16.88	\

Table 4.3: Crosstalk values associated with the 4-output DEMUX.

picted in figure 4.18. Notably, all wavelength ranges are obstructed except for the previously mentioned resonance wavelength.

Figure 4.19 elucidates the impact of geometrical parameters on transmission spectra within the context of our study. Notably, the perturbation of As_1, as delineated in figure 4.19(a), manifests minimal consequences on Ch_1, Ch_2, and Ch_3, but distinctly influences Ch_4. Transmission experiences a discernible reduction to zero at $As_1 = 140$ nm, with a subsequent ascent to its zenith at $As_1 = 200$ nm. Concomitantly, As_2 emerges as the preeminent factor, with Ch_1, Ch_2, and Ch_4 reaching their apex in transmission at $As_2 = 100$ nm, albeit at the expense of a reduction to 11% in Ch_3. A judicious trade-off is imperative. Remarkably, at $As_2 = 180$ nm, all channels attain their optimal transmission as illustrated in figure 4.19(b). As_3 imparts a pronounced effect on Ch_2 and a moderate influence on Ch_1, culminating in peak values across all outputs at $As_3 = 1090$ nm as seen in figure 4.19(c).

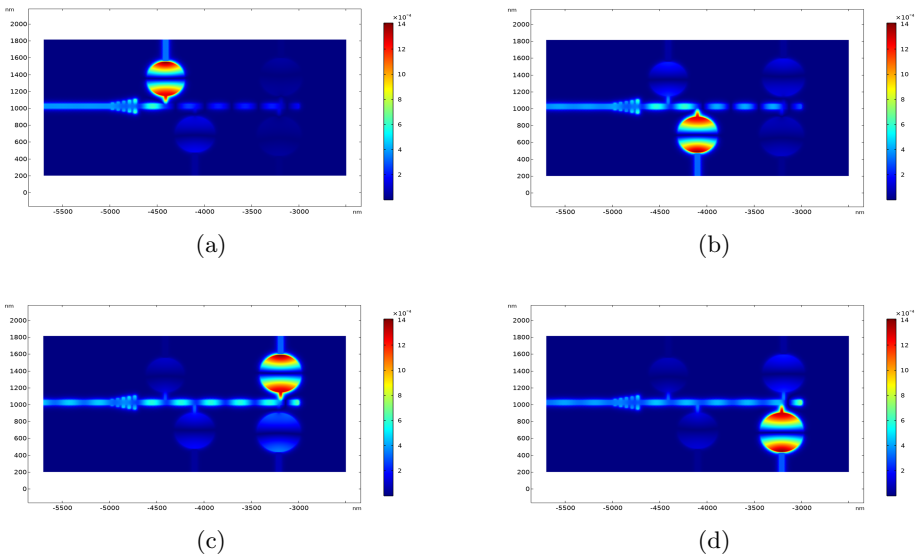

(a) (b) (c) (d)

Figure 4.18: The four channel demultiplexer field profile $|H_z|$. (a) λ=794.5 nm, (b) λ= 827.5 nm, (c) λ= 863 nm, (d) λ= 897 nm.

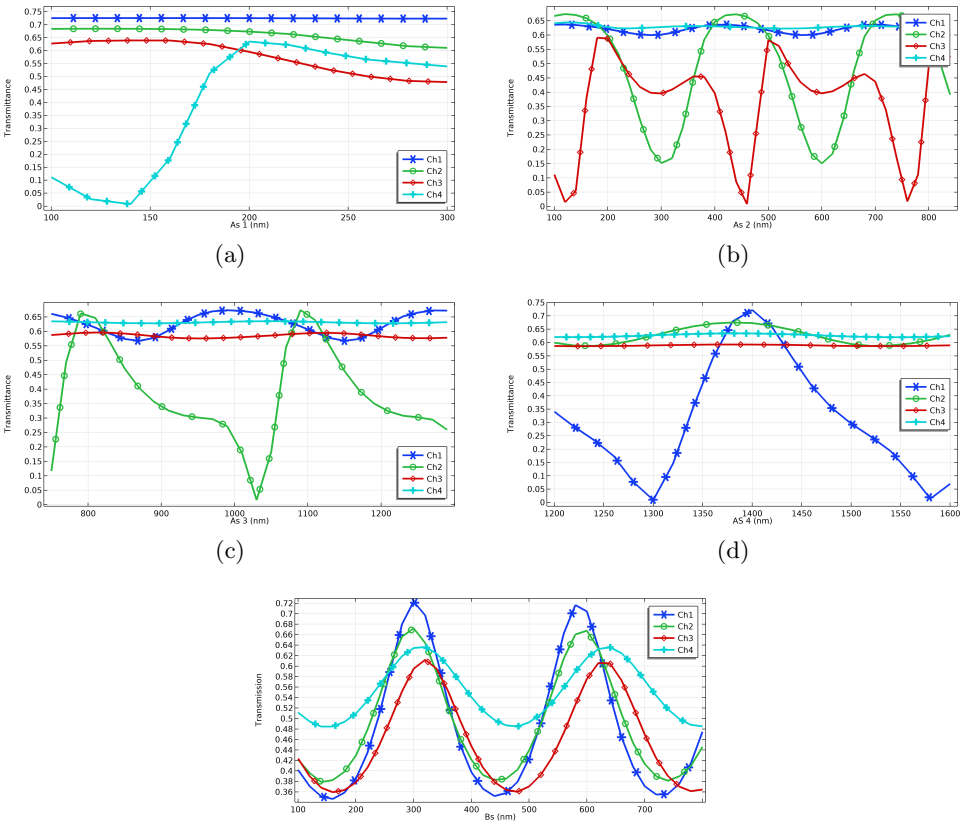

Figure 4.19: Geometrical parametere effect on the four channel DEMUX. (a) As_1, (b) As_2, (c) As_3, (d) As_4, (e) Bs.

The influence of the fourth resonator's position on transmission spectra is predominantly confined to Ch_1. In figure 4.19(d), specifically, at $As_4 =$ 1300 nm and $As_4 = 1570$ nm, Ch_1 transmission remains below 2%, while at $As_4 = 1400$ nm, it attains superlative results. Subsequently, in figure 4.19(e), an inquiry into the ramifications of B_s values on the transmission spectra of the four-channel DEMUX is conducted, revealing that $B_s = 300$ nm confers optimal outcomes for all output channels.

4.3.3 Eight channel DEMUX

A second DEMUX is proposed based on the nanodisk mono-mode filter, the proposed demultiplexer is an eight output channel as elucidated in figure 4.20(a), the resonance wavelengths are $\lambda_1 = 794.5$ nm, $\lambda_2 = 827$ nm, $\lambda_3 =$ 855 nm, $\lambda_4 = 884$ nm, $\lambda_5 = 918.5$ nm, $\lambda_6 = 950$ nm, $\lambda_7 = 992$ nm and $\lambda_8 =$ 1026 nm, for Ch_1, Ch_2, Ch_3, Ch_4, Ch_5, Ch_6, Ch_7 and Ch_8 with 71.51%, 62.14%, 60.54%, 56.32%, 48.78%, 53.01%, 53.66% and 53.57% sequentially

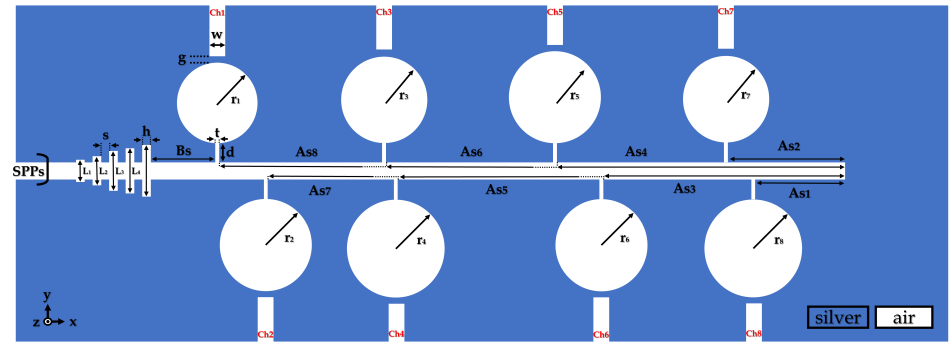

(a)

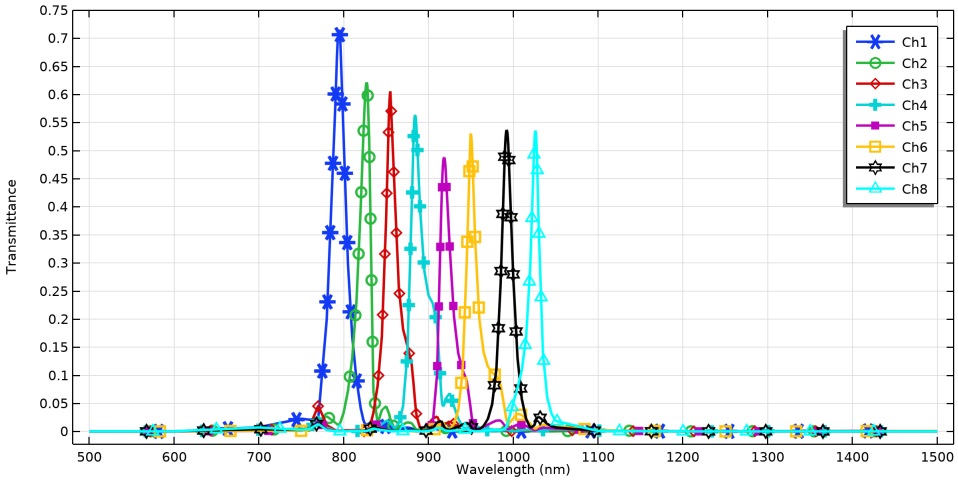

(b)

Figure 4.20: (a) Proposed eight channel DEMUX design, (b) it's transmission spectrum.

observed in figure 4.20(b). The channels spacing are 32.5nm, 28 nm, 29 nm, 34.5 nm, 31.5 nm, 42 nm and 34 nm with a Q-factor of 40.74, 55.13, 55.16, 50.51, 57.4, 70.37, 66.13 and 78.92 respectively. The cross-talk values are calculated and presented in table 4.4.

The geometrical parameter of the second plasmonic demultiplexer are as follow: $r_1 = 200$, $r_2 = 210$, $r_3 = 220$, $r_4 = 230$, $r_5 = 240$, $r_6 = 250$, $r_7 = 260$, $r_8 = 270$, $w = 50$, $B_s = 300$, $L_1 = 80$, $L_2 = 100$, $L_3 = 120$, $L_4 = 140$, $L_5 = 160$, $s = 35$, $h = 25$, g = 15, d = 100, t = 20, $As_1 = 220$, $As_2 = 240$, $As_3 = 1125$, $As_4 = 1400$, $As_5 = 1400$, $As_6 = 1400$, $As_7 = 2860$, $As_8 = 3170$, all in nm.

Figure 4.21 illustrates the impact of geometric parameters on transmission spectra. In figure 4.21(a), As_1 significantly influences Ch_8 and has a minor effect on other channels, yielding optimal results at $As_1 = 220$ nm.

Moving to figure 4.21(b), As_2 affects Ch_7, with a lesser impact on other channels. Optimal transmission for Ch_7 is achieved at $As_2 = 240$ nm. As indicated in figure 4.21(c), As_3 exhibits comparatively lower impact levels, but Ch_6 shows a small peak at 1125 nm.

Examining figure 4.21(d), As_4 profoundly influences transmission. At $As_4 = 1160$ nm, transmission drops to 2.2%, while at $A_4 = 1120$ nm, it reaches 49.25%, the highest observed value for Ch_5. Figure 4.21(e) demonstrates that As_5 affects both Ch_2 and Ch_4 similarly, with optimal results at $As_5 = 1950$ nm. As portrayed in figure 4.21(f), As_6 influences Ch_2 and Ch_3, and both channels exhibit their highest transmission peaks at $As_6 = 1940$ nm.

Cross-talk(dB)	CH_1	CH_2	CH_3	CH_4	CH_5	CH_6	CH_7	CH_8
CH_1	⟍	-17.4	-27.75	-29.5	-30.76	-32.52	-33.77	-35.53
CH_2	-17.14	⟍	-34.92	-37.93	-23.46	-25.38	-26.47	-28.9
CH_3	-20.83	-14.39	⟍	-16.36	-27.03	-29.36	-27.82	-30.83
CH_4	-24.08	-19.44	-10.10	⟍	-37.5	-37.5	-25.2	-28.47
CH_5	-22.9	-19.89	-16.47	-10.05	⟍	-16.09	-17.85	-22.9
CH_6	-27.24	-24.93	-20.8	-17.24	-11.61	⟍	-17.7	-25.2
CH_7	-28.8	-27.3	-25.25	-13.32	-19.51	-14.11	⟍	-17.51
CH_8	-29.16	-28.26	-27.75	-25.98	-23.3	-20.3	-15.14	⟍

Table 4.4: Crosstalk values associated with the 8-output DEMUX.

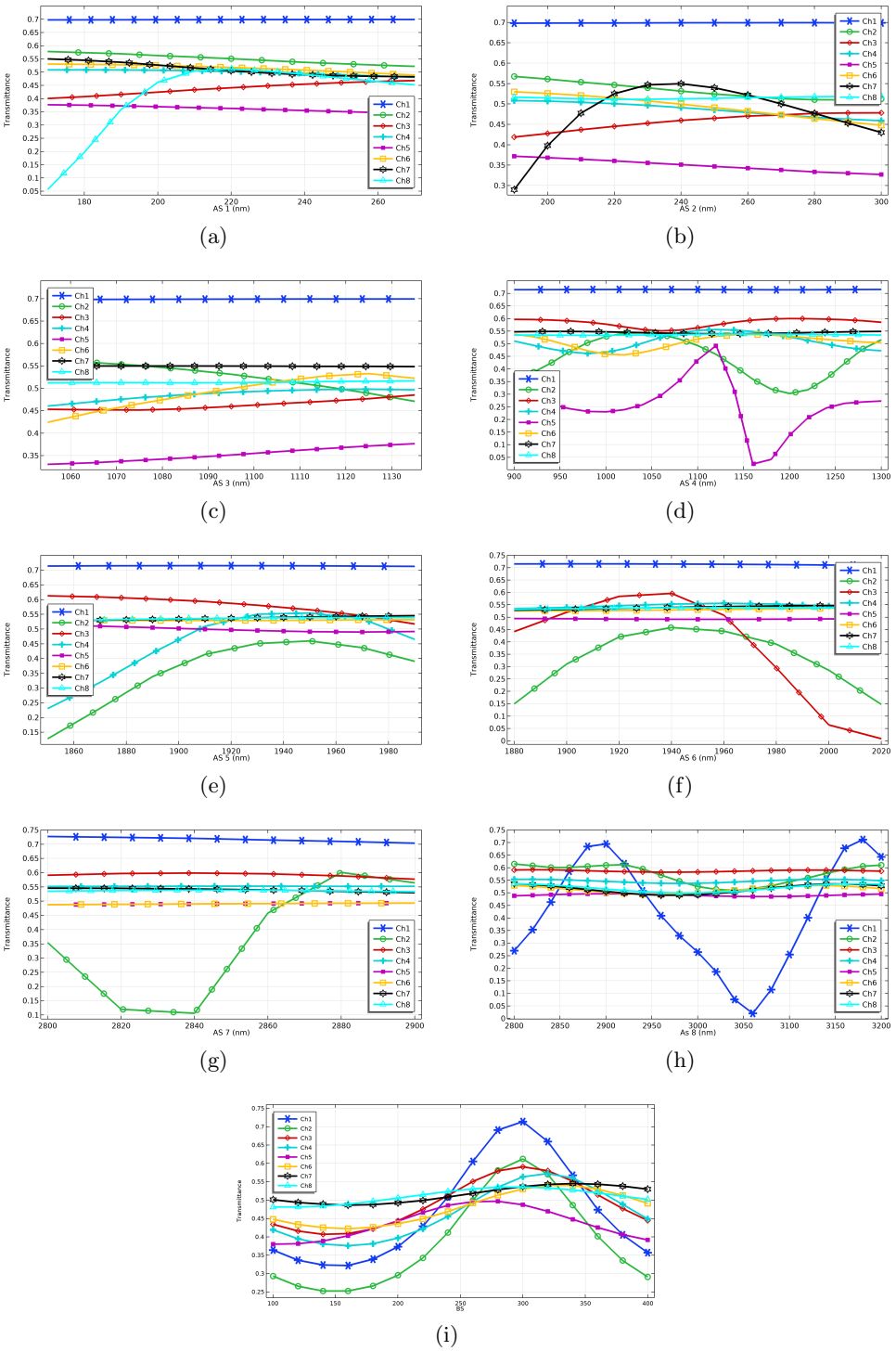

(a) (b) (c) (d) (e) (f) (g) (h) (i)

Figure 4.21: Geometrical parametere effect on the eight channel DEMUX. (a) As_1, (b) As_2, (c) As_3, (d) As_4, (e) As_5, (f) As_6, (g) As_7, (h) As_8, (i) Bs.

In figure 4.21(g), As_7's influence on transmission is depicted, affecting only Ch_2 and achieving a transmission rate of 60.1% at $As_7 = 2880$ nm. Considering As_8, which unevenly affects Ch_1 and other channels, figure 4.21(h) reveals two prominent transmission peaks at $As_8 = 2900$ nm and $As_8 = 3180$ nm. Transmission rates of 69.4% and 71.15%, respectively, were observed, while other channels ranged between 48.77% and 61.2%. As a result of its exceptional performance, $As_8 = 3180$ nm was chosen as the preferred parameter setting.

The impact of Bs values is notably pronounced on Ch_1 and Ch_2, while exerting a more subtle influence on the remaining channels figure 4.21(i). Specifically, when Bs is set to 150 nm, the transmission rates experience a substantial decline, with Ch_2 dropping to 25% and $Ch_1$to 32%. To ensure a harmonious outcome across all channel outputs, Bs was judiciously selected at 300 nm. This choice yielded compatible results: 71.36% transmission for Ch_1, 61.2% for Ch_2, and transmission rates ranging between 48.72% and 59.06% for all other channels.

Figure 4.22 visually depicts the field profile $|Hz|$ of the proposed eight-channel DEMUX for enhanced clarity. The illustration reveals resonance wavelengths confined within the nanodisk resonators, effectively blocking all other wavelengths except for specific resonances at 794.5 nm, 827 nm, 855 nm, 884 nm, 918.5 nm, 950 nm, 992 nm, and 1026 nm. These distinctive wavelengths seamlessly pass through to the respective output ports of Ch_1, Ch_2, Ch_3, Ch_4, Ch_5, Ch_6, Ch_7, and Ch_8, offering a comprehensive view of the device's operational dynamics.

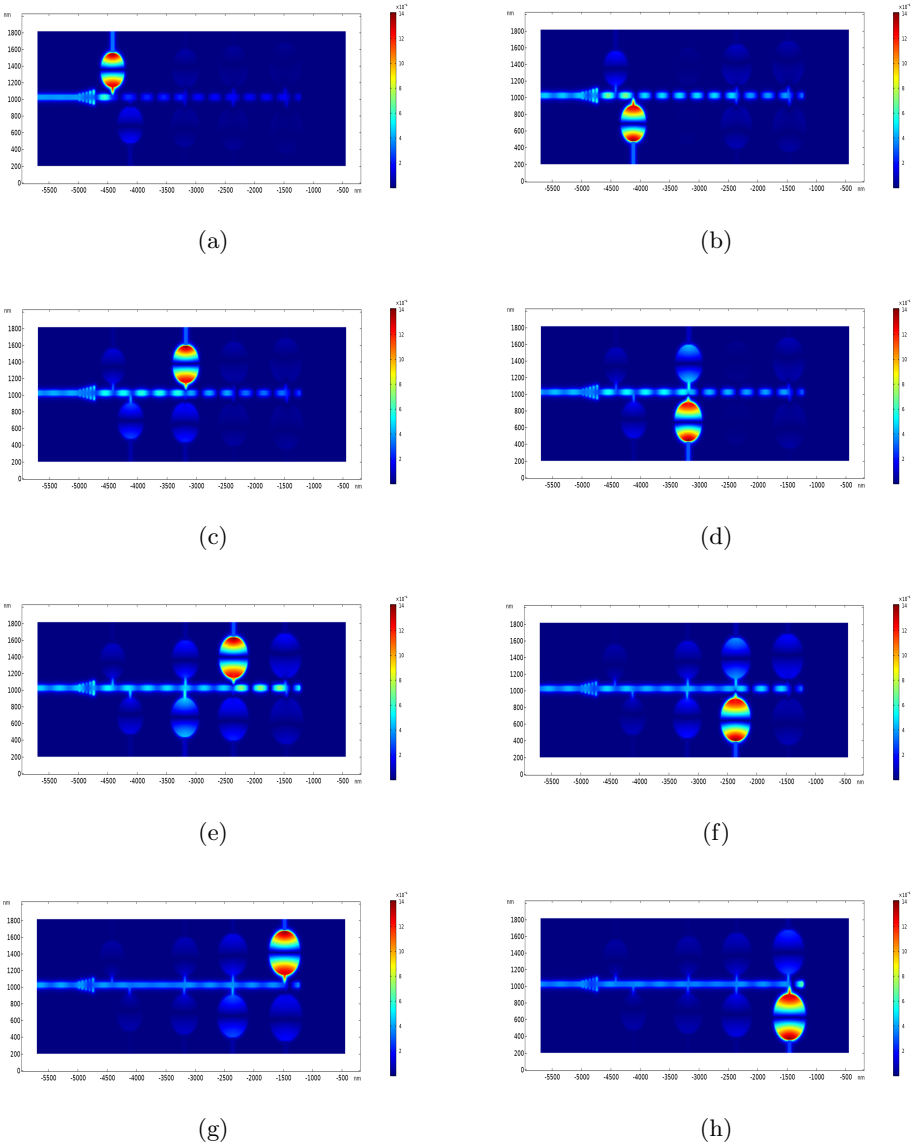

Figure 4.22: The field profile of the eight channel DEMUX based nanodisk resonator.

4.4 Basic filter based on pill resonator

The third basic filter design is based on a plasmonic MIM waveguide coupled with pill resonator as illustrated in figure 4.23(a), the geometrical parameters are $W = 650$, $R = 135$, $G = 15$, $H = 50$ all on nm. The same metal have been used and with the same characteristics of relative permittivity, plasma frequency and the damping frequency. As witnessed

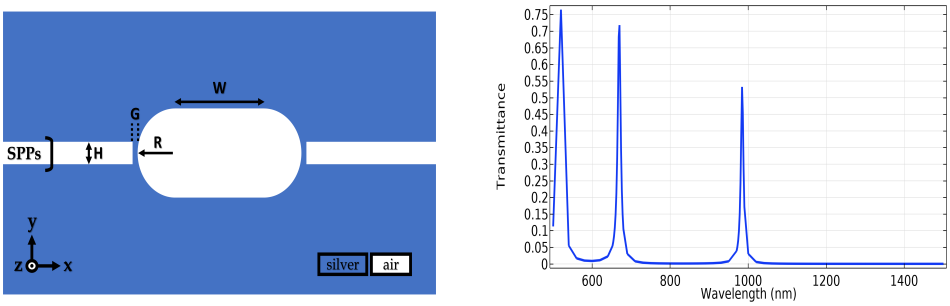

(a) (b)

Figure 4.23: The basic filter based on the pill resonator. (a) Schematic design, (b) transmission spectrum.

from figure 4.23(b) this cavity have three resonance modes at $\lambda = 520$ nm, $\lambda = 670$ nm and $\lambda = 984$ nm with transmission peaks of 76.43%, 71.78% and 53.21%, respectively. The FWHM are 23 nm, 9 nm and 8 nm with Q-factor of 22.6, 74.44 and 118.5, sequentially.

In order to provide a clearer understanding of the operational efficiency of the fundamental filter, figure 4.24 displays the field profiles $|Hz|$ for both resonance and non-resonance wavelengths. The visualization distinctly highlights the presence of resonance wavelengths within the cavity, while simultaneously demonstrating the inability of non-resonance wavelengths to propagate towards the output port. This graphical representation serves to underscore the effective discrimination and selective transmission characteristics of the basic filter.

To selectively eliminate undesired wavelengths, we implemented a strategy involving the deliberate mismatch of the output waveguide with the field profile. Initially, in figure 4.25(a), the output waveguide was positioned at the bottom-middle side of the cavity. The corresponding transmission spectra in figure 4.25(b) reveal the effective elimination of the 670nm wavelength, while wavelengths at 520nm and 984nm successfully reach the output port.

Subsequently, in figure 4.25(c), we relocated the output port to the right-bottom side of the cavity. In this configuration, only wavelengths $\lambda = 520$nm and $\lambda = 668$nm are observed to reach the output port. It is noteworthy that both cases exhibited some noteworthy alterations. In the first scenario, the transmission of the first mode decreased to 42.73%, and the Full Width at Half Maximum (FWHM) measured 23 nm. The second mode was entirely suppressed, while the third mode maintained approximately the same transmission at 54.62% with an FWHM of 8.5 nm.

The second scenario indicated a marginal reduction in the transmission of the first mode, dropping from 76.43% to 66.5%, with an FWHM of 23 nm. Simultaneously, the second mode experienced a 2 nm leftward shift, resulting

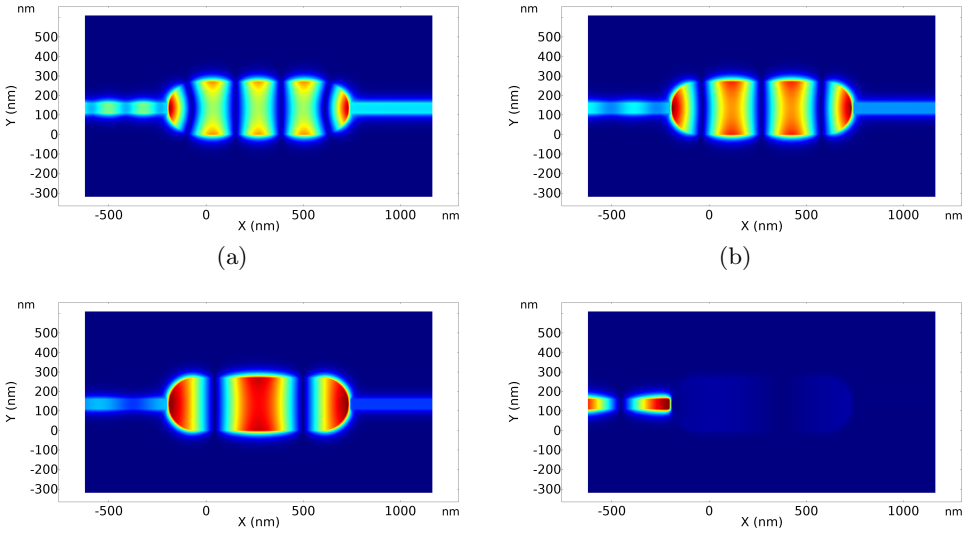

Figure 4.24: The field profile $|H_z|$ of resonance, (a) λ=520 nm, (b) λ= 670 nm, (c) λ= 984 nm, and non resonance (d) λ= 1500 nm wavelengths.

in a transmission decrease from 71.78% to 63.6%, along with an FWHM of 7.5nm. These adjustments underscore the efficacy of strategically placing

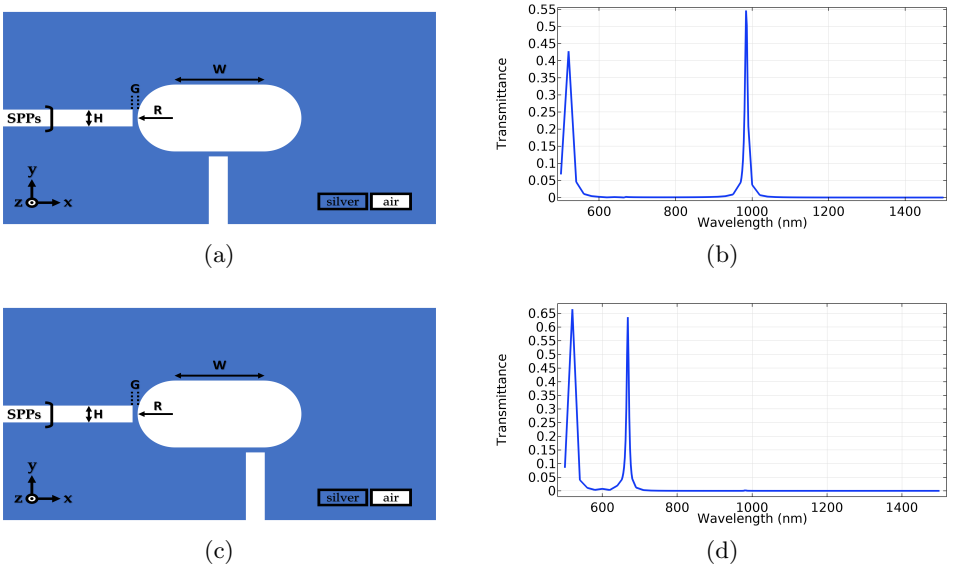

Figure 4.25: (a)(c) Double mode basic filter designs, (b)(d) its transmission spectrum respectively.

the output waveguide to selectively filter and control the transmission of specific wavelengths.

4.4.1 Design procedure of the high pass filter

Using a coupled sided output waveguide doesn't resolve the problem of the multimode filter, so it comes to the idea of a high pass filter that could blocked the first wavelength of 520 nm wish is presented in the two above proposed filters, to do so, we have proposed a multi-stub structure that act as a high pass filter as shown in figure 4.26(a), these nano stubs with the geometrical parameters : T = 20 nm, E = 35 nm, S = 120 nm. Figure 4.26(b) illustrate the transmission spectrum of the proposed HPF, and as seen the cut-off wavelength is $\lambda_c = 600$ nm.

The investigation focused on analyzing the impact of geometric parameters to strategically adjust the cutoff wavelength, aiming to position it in a suitable range. This adjustment enables precise control over the filter's output. As witnessed from figure 4.27(a) the impact of the parameter "T" on the transmission spectra. The values of "T" were varied from 20 nm to 40 nm in increments of 5 nm. Throughout this range, a consistent response was observed with a noticeable red shift. However, all values exhibited a multi-peak pattern around 550 nm, which is undesirable for high-pass filters. The most favorable outcome was observed at T = 20 nm. Subsequently, the influence of the "E" values on the transmission spectra of the HPF was assessed, as depicted in figure 4.27(b). "E" was varied from 20 nm to 40 nm with a step size of 5 nm. It was observed that "E" had minimal impact on the transmission spectra, but the optimal result was achieved at E = 35 nm.

4.4.2 Mono-mode filters based pill resonator

Incorporating the proposed HPF outlined earlier into the foundational

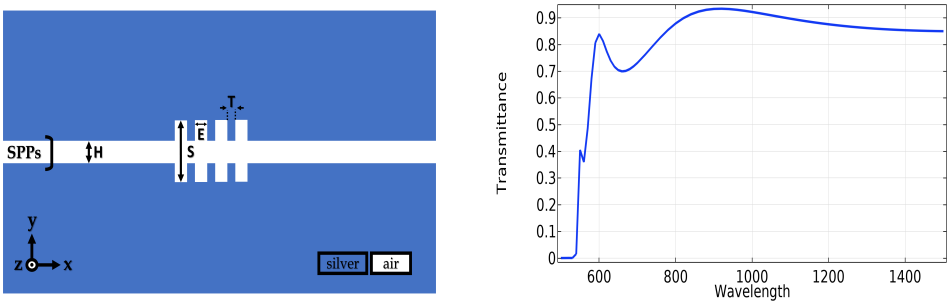

(a) (b)

Figure 4.26: (a) Schematic of the HPF; (b) transmission spectrum of the proposed HPF.

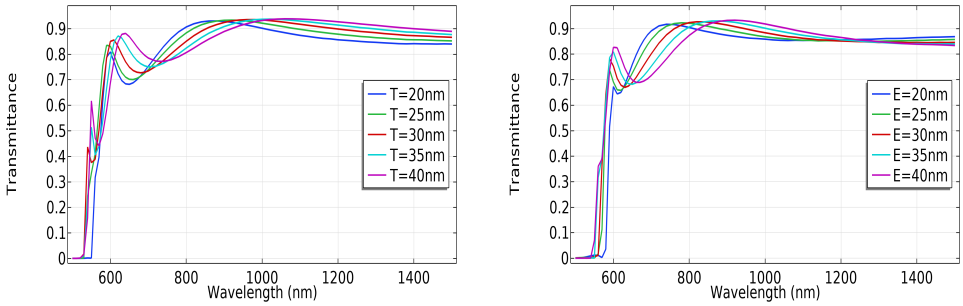

(a) (b)

Figure 4.27: (a) "T" and (b) "E" parameter effect on the transmission spectra of the HPF.

filter design before the racetrack cavity results in the selective passage of wavelengths greater than 600 nm to reach the resonance cavity. In the initial scenario, the HPF is utilized alongside the first double-mode filter, as illustrated in figure 4.28(a). The transmission spectra of the first single-mode filter are presented in figure 4.28(b), revealing a single-mode filter at 986 nm with a transmission rate of 50.93%. The full width at half maximum (FWHM) is measured at 9 nm, boasting a high-quality factor (Q-factor) of approximately 109.56. The insertion loss is recorded at 2.93 dB.

In the second scenario, the design involves the second single-mode filter configuration, depicted in figure 4.28(c). Examining figure 4.28(c), it is evident that a single-mode filter is achieved at $\lambda = 666$ nm within the wavelength range of 500 nm to 1500 nm. This filter exhibits a transmission peak of 62%, with a remarkably narrow full width at half maximum (FWHM) of 7 nm. The quality factor (Q-factor) for this configuration is measured at 95.14, indicating a high level of spectral selectivity. The insertion loss is calculated to be 2.076 dB.

To obtain a clearer understanding of the basic filter's performance, the field distributions of resonant and non-resonant wavelengths are plotted in figure 4.29. In figure 4.29(a), it is evident that the resonance wavelength at 520 nm is effectively blocked by the high-pass filter (HPF). The second mode at 668 nm cannot reach the output due to a mismatch between the output waveguide and the field profile, as depicted in figure 4.29(b). On the other hand, the third mode at 986 nm successfully reaches the output port, as seen in figure 4.29(c), while non-resonant wavelengths are impeded from reaching the output, as demonstrated in figure 4.29(d). For the second proposed filter, notably, the resonant wavelength of 520 nm is obstructed by the HPF, failing to find a path to the resonator see figure 4.29(e). In contrast, the wavelength of 666 nm can penetrate to the output port figure 4.29(f), and the third resonant wavelength at 984 nm is hindered by the

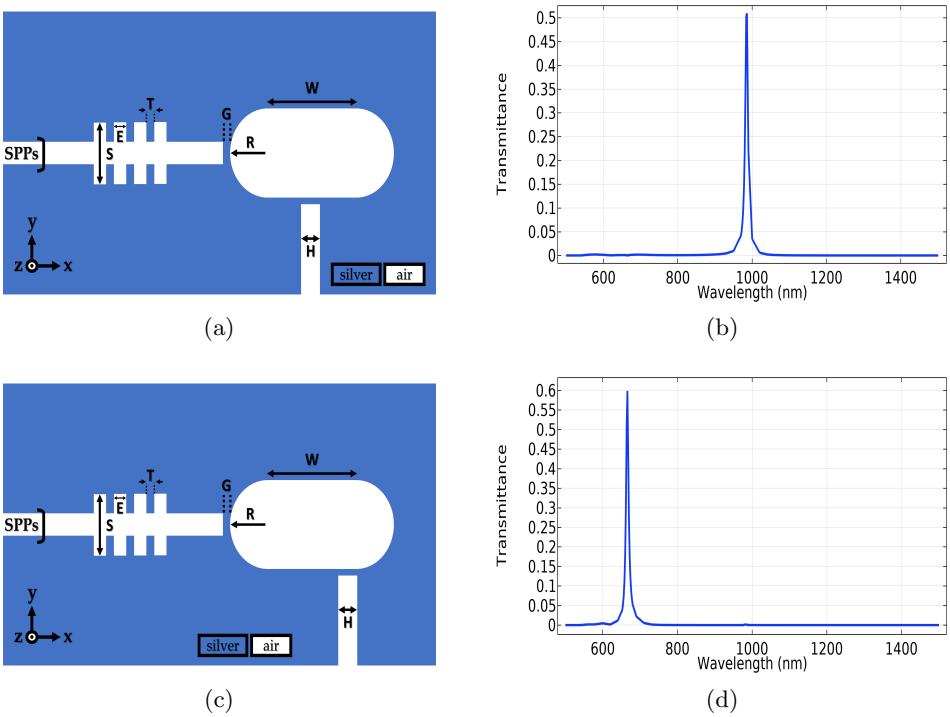

Figure 4.28: (a)(c) Mono-mode basic filter designs, (b)(d) its transmission spectrum respectively.

output waveguide mismatch, preventing it from reaching the output. Figure 4.29(g) and figure 4.29(h) represent the non resonance wavelength. These observations collectively contribute to the realization of a two single-mode filters.

4.5 Results comparison

The proposed demultiplexers with four and eight channels were assessed by comparing them to existing research from various publishers. Numerical investigations and simulations were conducted using the Finite Element Method (FEM) implemented in COMSOL Multiphysics software. The obtained results were then compared based on the number of output ports (Np), resonance wavelengths (λ_r), transmission values (Tr%), channel spacing (ChSp), Full Width at Half Maximum (FWHM), Q-factor, and minimum cross-talk.

In comparing the number of output ports (Np) across various demultiplexer designs, it is observed that the proposed demultiplexers in this study exhibit distinct characteristics in comparison to previously published works. Reference [95] presents a demultiplexer with six output ports,

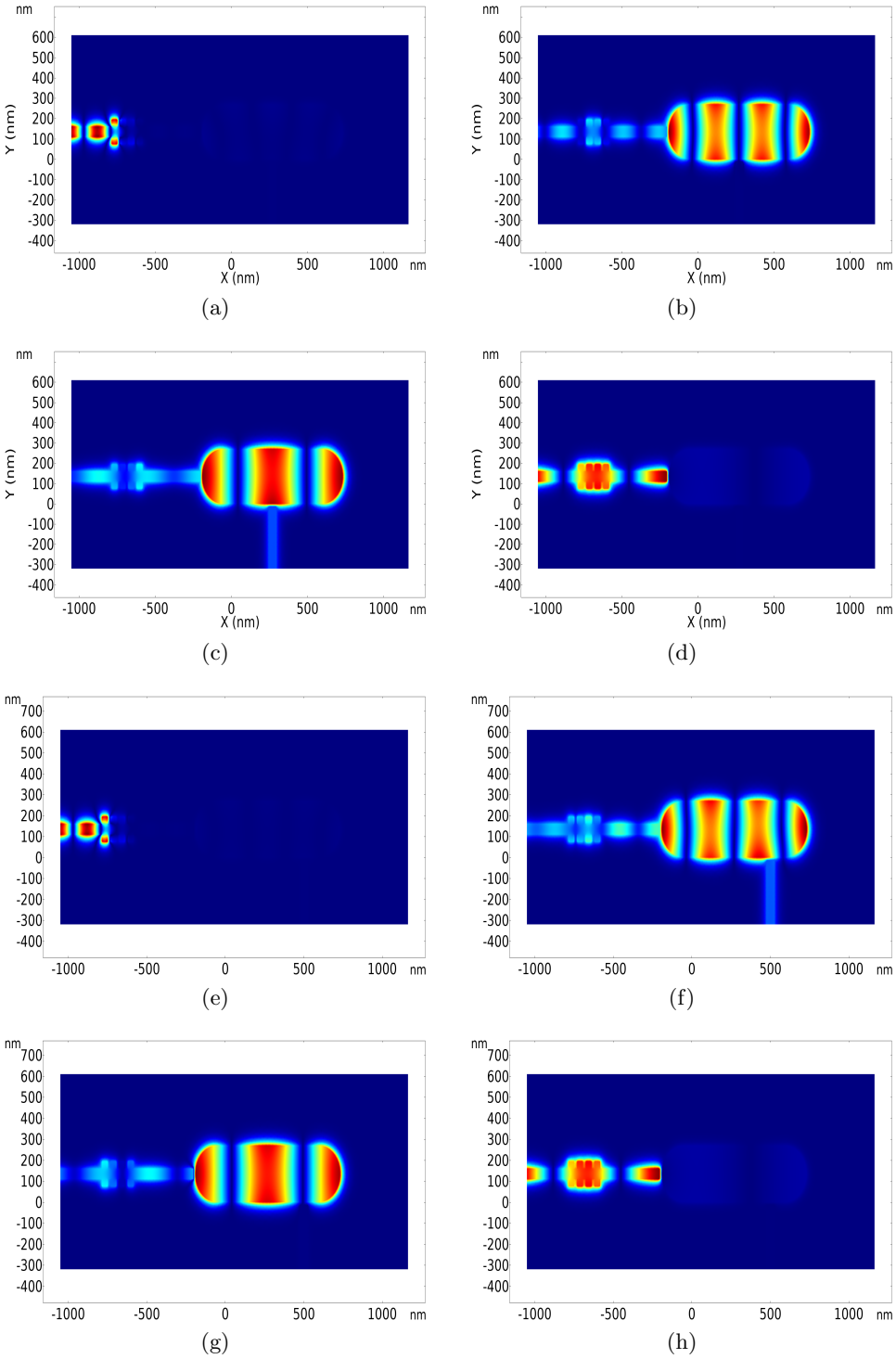

Figure 4.29: Field profiles illustrating (a)(e) High Pass Filter (HPF) in operation, (b)(g) mismatch with the output waveguide, (c)(f) mono-mode filters, and (d)(h) non-resonant wavelength.

while [96] features a design with four output ports. Another study by [93] explores demultiplexers with four and six output ports. In contrast, the current work introduces demultiplexers with four and eight output ports, showcasing an expansion in the number of channels. This augmentation in output ports holds potential implications for increased data throughput and versatility in optical communication systems. The numerical values associated with Np further emphasize the diversity and progression in demultiplexer designs, underscoring the nuanced contributions and advancements introduced in this research.

In examining the resonance wavelengths (λ_r) across different demultiplexer configurations, a comparative analysis reveals noteworthy distinctions among the proposed demultiplexers and those previously reported in the literature. Reference [95] employs a demultiplexer design with multiple resonance wavelengths, specifically at 720 nm, 760 nm, 810 nm, 870 nm, 930 nm, and 980 nm. In contrast, [96] features a demultiplexer with distinct resonance wavelengths at 1450 nm, 1500 nm, 1550 nm, and 1600 nm. Additionally, [93] investigates demultiplexers with resonance wavelengths at 1377 nm, 1576 nm, 1682 nm, and 1789 nm for four channels and 1385 nm, 1479 nm, 1553 nm, 1628 nm, 1736 nm, and 1883 nm for six channels.

Comparatively, the proposed demultiplexers in the current work in [97] and [98], exhibit resonance wavelengths at 762 nm, 772.5 nm, 783.2 nm, and 793 nm for the four-channel configuration and at 761 nm, 771.5 nm, 782.5 nm, 793 nm, 805 nm, 814.5 nm, 825 nm, and 835 nm for the eight-channel configuration.

In the context of transmission characteristics, the comparison among demultiplexer configurations, as detailed in various references and the current work, highlights distinctive features in terms of transmission percentages (Tr%). Reference [95] reports transmission values of 75%, 71%, 68%, 65%, 61%, and 58% for its demultiplexer design with six output ports. In [96], a demultiplexer with four output ports exhibits varying transmission percentages with a maximum of 40% and a minimum of 30%. Additionally, [93] presents transmission values of 54.13%, 52.75%, 53.6%, and 49.4% for a demultiplexer with four output ports and 37%, 37.15%, 49.62%, 43.67%, 48.43%, and 35% for a six-output-port demultiplexer.

In contrast, the proposed demultiplexers in the current work, as outlined in [97] and [98], demonstrate transmission percentages that differ across the number of output ports and channels. For instance, the four-channel demultiplexer in [97] exhibits transmission percentages of 59.17%, 53.40%, 55.40%, and 56.04%, while the eight-channel demultiplexer ranges from 47.35% to 26.91%. Similarly, the four-channel demultiplexer in [98] showcases transmission percentages of 72.48%, 67.29%, 59.47%, and 63.43%, and the eight-channel demultiplexer presents values from 71.51% to 53.57%.

Examining the channel spacing (ChSp) parameter across various demultiplexer designs, a comparative analysis reveals distinct characteristics

among different configurations detailed in references and the present study. Reference [95] employs a demultiplexer with varying channel spacing values, specifically at 40 nm, 50 nm, 60 nm, 60 nm, and 50 nm.

In [96], the demultiplexer design with four output ports features a consistent channel spacing of 50 nm. Additionally, [93] explores demultiplexers with four and six output ports, showcasing channel spacing values of 137.33 nm and 99.6 nm, respectively.

Comparatively, the proposed demultiplexers in the current work, detailed in [97] and [98], exhibit consistent channel spacing for both four-channel and eight-channel configurations. The four-channel demultiplexer in [97] demonstrates channel spacing values of 10.5 nm, 10.7 nm, and 10.6 nm, while the eight-channel demultiplexer ranges from 10.5 nm to 12 nm. Similarly, the four-channel demultiplexer in [98] showcases channel spacing values of 33 nm, 35.5 nm, and 34 nm, and the eight-channel demultiplexer presents values ranging from 28 nm to 42 nm.

In evaluating the Full Width at Half Maximum (FWHM) parameter across various demultiplexer configurations, a comparative analysis reveals distinctive characteristics among different designs presented in references and the current study. Reference [95] reports a fixed FWHM value of 50 nm for its demultiplexer design with six output ports.

In [96], the demultiplexer design with four output ports features a consistent FWHM of 40 nm. Additionally, [93] explores demultiplexers with four and six output ports, showcasing FWHM values of 137.33 nm and 99.6 nm, respectively.

Comparatively, the proposed demultiplexers in the present work, detailed in [97] and [98], exhibit varying FWHM values for both four-channel and eight-channel configurations. The four-channel demultiplexer in [97] demonstrates FWHM values ranging from 10.5 nm to 10.7 nm, while the eight-channel demultiplexer exhibits a range from 9.5 nm to 12 nm. Similarly, the four-channel demultiplexer in [98] showcases FWHM values ranging from 33 nm to 35.5 nm, and the eight-channel demultiplexer presents values ranging from 28 nm to 42 nm.

The calculated values of Q-Factor are high, resulting from the fact that we have good FWHM values. We have the lowest cross talk values among all the references in table 4.5 which indicate the minimum effect of channels on each other.

As observed, the previously documented demultiplexers (DEMUXs) generally feature two, three, four, or six output channels. Notably, two of the proposed structures in our work extend to eight-channel DEMUXs, exhibiting a commendable maximum transmittance suitable for the expanded configuration. An essential characteristic of filters and DEMUXs is the Full Width at Half Maximum (FWHM). As depicted in table 4.5, our DEMUXs demonstrate the narrowest FWHM compared to all previously reported works, signifying superior selectivity. A lower FWHM corresponds

Table 4.5: Comparaison of the proposed DEMUX and recently published works.

Refs	Np	λ_r(nm)	Tr%	ChSp	FWHM (nm)	Q-factor	Min Cross talk(dB)
[95]	6	720 760 810 870 930 980	75 71 68 65 61 58	40 50 60 60 50	50	\	\
[96]	4	1450 1500 1550 1600	Max=40 Min=30	50	40	\	\
[93]	4	1377 1576 1682 1789	54.13 52.75 53.6 49.4	137.33	83.1 91.1 121.4 122.5	16.57 17.3 13.86 14.6	\
[93]	6	1385 1479 1553 1628 1736 1883	37 37.15 49.62 43.67 48.43 35	99.6	88.4 57 80.2 78.8 127.5 120	15.67 25.94 19.36 20.66 13.62 15.7	\
[97] Our work	4	762 772.5 783.2 793	59.17 53.40 55.40 56.04	10.5 10.7 10.6	10.5 9 9.5 9.5	72.57 85.84 82.44 83.47	-19.26 -15.81 -15.96 -19.7
[97] Our work	8	761 771.5 782.5 793 805 814.5 825 835	47.35 47.81 45.83 46.08 37.58 35.41 35.11 26.91	10.5 11 10.5 12 9.5 10.5 10	10 9.5 9.5 11 8 7.5 8.5 7.25	76.1 81.2 82.37 72.1 100.625 108.6 97.06 115.17	-26.75 -26.79 -22.63 -26.63 -19.72 -25.49 -25.45 -31.28
[98] Our work	4	794.5 827.5 863 897	72.48 67.29 59.47 63.43	33 35.5 34	17.5 15.5 15 13.5	45.4 53.39 57.53 66.44	-28.6 -22.83 -22.97 -25.01
[98] Our work	8	794.5 827 855 884 918.5 950 992 1026	71.51 62.14 60.54 56.32 48.78 53.01 53.66 53.57	32.5 28 29 34.5 31.5 42 34	19.5 15 15.5 17.5 16 13.5 15 13	40.74 55.13 55.16 50.51 57.4 70.37 66.13 78.92	-35.53 -37.93 -30.83 -37.5 -22.9 -27.24 -28.8 -29.16

to a higher Q-factor, and consequently, our designs exhibit the highest Q-factors. The spacing between channels poses a challenge in many reported works, with potential issues of either too low spacing causing spectral overlap or excessively high spacing leading to inefficient use of the spectral range. In our proposed structures, the channel spacing is carefully controlled and studied to prevent spectral overlap without unnecessary waste of spectral field. We have achieved low cross-talk values for both four and eight-channel outputs, indicating minimal interference between channels.

4.6 Conclusion

In drawing the final lines of this chapter, our exploration into infrared plasmonic communication devices has unveiled a transformative breakthrough in the realm of optical technology. The pioneering achievement of the highest number of demultiplexer outputs, coupled with exceptional transmission efficiency and selectivity, establishes our work as a benchmark in the field.

What distinguishes our approach is the introduction of a novel technique, where the careful observation of field profiles precedes the refinement of output ports. This innovative methodology has proven instrumental in surpassing existing benchmarks and sets the stage for a new paradigm in plasmonic device design. As we conclude this chapter, the profound implications of our work extend beyond numerical achievements, signaling a paradigm shift and inviting future researchers to explore the untapped potential of plasmonics in the evolution of infrared communication technologies.

Conclusion and perspectives

As we draw the curtains on this exploration into plasmonic basic filters and demultiplexers operating in the infrared (IR) region, the culmination of our efforts heralds a significant leap forward in the realm of optical communication technologies. Our investigation, rooted in Metal-Insulator-Metal (MIM) structures, the Drude model with silver as the metal, and the manipulation of Surface Plasmon Polaritons (SPPs), has yielded groundbreaking results that surpass existing benchmarks in the field.

Foremost among our achievements is the attainment of the highest number of demultiplexer outputs recorded to date, surpassing benchmarks set by previously published papers. This remarkable feat not only underscores the efficacy of our plasmonic devices but positions our work at the forefront of advancements in the field. The unprecedented number of demultiplexer outputs stands as a testament to the innovation and optimization embedded in our design.

Moreover, the empirical results presented herein showcase not only the highest number of demultiplexer outputs but also the best transmission efficiency and selectivity reported in the existing literature. Our devices exhibit unparalleled performance, demonstrating that our approach to plasmonic filter and demultiplexer design has achieved an exceptional balance between output quantity and signal fidelity. This achievement positions our work as a benchmark for future developments in the domain of plasmonic communication devices.

Central to our success is the introduction of a novel technique—one that involves the meticulous observation of field profiles as a precursor to the refinement of output ports. This innovative approach, where a keen understanding of electromagnetic field distributions precedes device optimization, has proven instrumental in achieving the extraordinary results presented in this thesis. It not only represents a departure from conventional methodologies but also establishes a paradigm for future investigations in plasmonics.

As we reflect on the significance of our work, it becomes evident that the implications extend far beyond the confines of this thesis. We have not only pushed the boundaries of achievable demultiplexer outputs, transmission efficiency, and selectivity but have also introduced a novel methodology that redefines the design and optimization process. This thesis stands as

a beacon for researchers and innovators, inviting them to explore the untapped potential of plasmonics in the pursuit of advanced communication technologies.

In conclusion, our journey through the intricacies of plasmonic structures has yielded not just numerical achievements but a transformative approach to device design. The legacy of this work extends an invitation to future explorers, signaling a new era in the evolution of infrared plasmonic communication devices.

Published works

Abderrahmane, I., Hadjira, B., & Mehadji, A. (2023). Efficient 4 and 8 plasmonic wavelength DEMUX with ultra high Q-factor and low FWHM based on nano-rectangular resonators. Optical and Quantum Electronics, 55(2), 108.

Rahmi, B., Badaoui, H., Abri, M., & Imam, A. (2023). High-performance all-optical 3× 8 photonic crystal decoder using nonlinear micro-ring resonators. Applied Physics B, 129(3), 35.

Abderrahmane, I., Hadjira, B., Mehadji, A., & Bachir, R. (2023). High performance single mode plasmonic filter and efficient wavelength demultiplexing based on nanodisk resonators. Optical and Quantum Electronics, 55(5), 413.

Abderrahmane, I., Hadjira, B., Mehadji, A., Bensalah, H., & Bachir, R. (2023, March). High selective single mode plasmonic filters based on MIM coupled with pill resonator. In 2023 International Conference on Advances in Electronics, Control and Communication Systems (ICAECCS) (pp. 1-5). IEEE.

Bibliography

[1] I. F. Akyildiz, A. Kak, and S. Nie, "6g and beyond: The future of wireless communications systems," *IEEE access*, vol. 8, pp. 133 995–134 030, 2020.

[2] A. Alves, M. C. Melo, J. Siqueira, F. Zanella, J. R. Mejía-Salazar, and C. S. Arismar, "Plasmonic nanoantennas for 6g intra/inter-chip optical-wireless communications," in *2020 2nd 6G Wireless Summit (6G SUMMIT)*. IEEE, 2020, pp. 1–4.

[3] M. Shur, G. Aizin, T. Otsuji, and V. Ryzhii, "Plasmonic field-effect transistors (terafets) for 6g communications," *Sensors*, vol. 21, no. 23, p. 7907, 2021.

[4] W. O. F. Carvalho and J. R. Mejía-Salazar, "Plasmonics for telecommunications applications," *Sensors*, vol. 20, no. 9, p. 2488, 2020.

[5] J. Zhang, L. Zhang, and W. Xu, "Surface plasmon polaritons: physics and applications," *Journal of Physics D: Applied Physics*, vol. 45, no. 11, p. 113001, 2012.

[6] S. A. Maier *et al.*, *Plasmonics: fundamentals and applications*. Springer, 2007, vol. 1.

[7] A. K. Sharma, R. Jha, and B. Gupta, "Fiber-optic sensors based on surface plasmon resonance: a comprehensive review," *IEEE Sensors journal*, vol. 7, no. 8, pp. 1118–1129, 2007.

[8] S. Wang, X.-Y. Wang, B. Li, H.-Z. Chen, Y.-L. Wang, L. Dai, R. F. Oulton, and R.-M. Ma, "Unusual scaling laws for plasmonic nanolasers beyond the diffraction limit," *Nature communications*, vol. 8, no. 1, p. 1889, 2017.

[9] B. Lee, I.-M. Lee, S. Kim, D.-H. Oh, and L. Hesselink, "Review on sub-wavelength confinement of light with plasmonics," *Journal of Modern Optics*, vol. 57, no. 16, pp. 1479–1497, 2010.

[10] S. Khani, M. Danaie, and P. Rezaei, "Size reduction of mim surface plasmon based optical bandpass filters by the introduction of arrays of silver nano-rods," *Physica E: Low-Dimensional Systems and Nanostructures*, vol. 113, pp. 25–34, 2019.

[11] A. Yariv and P. Yeh, *Photonics: optical electronics in modern communications*. Oxford university press, 2007.

[12] H. Gibbs, *Optical bistability: controlling light with light*. Elsevier, 2012.

[13] F. Hong and R. Blaikie, "Plasmonic lithography: recent progress," *Advanced Optical Materials*, vol. 7, no. 14, p. 1801653, 2019.

[14] S. Li, P. Miao, Y. Zhang, J. Wu, B. Zhang, Y. Du, X. Han, J. Sun, and P. Xu, "Recent advances in plasmonic nanostructures for enhanced photocatalysis and electrocatalysis," *Advanced Materials*, vol. 33, no. 6, p. 2000086, 2021.

[15] V. Yesudasu, H. S. Pradhan, and R. J. Pandya, "Recent progress in surface plasmon resonance based sensors: A comprehensive review," *Heliyon*, vol. 7, no. 3, p. e06321, 2021.

[16] Y. H. Shwan, B. N. Ghafoor, and G. H. Hamasalih, "Optimization of surface plasmon resonance (spr) for gold/air interface by using kretschmann configuration," *Engineering and Technology Journal*, vol. 40, no. 10, pp. 1334–1341, 2022.

[17] M. G. Hudedmani and B. S. Pagad, "Plasmonics: a path to replace electronics and photonics by scalable ultra-fast technology," *Advanced Journal of Graduate Research*, vol. 7, no. 1, pp. 37–44, 2020.

[18] R. Yang, J. Xu, N.-H. Shen, F. Zhang, Q. Fu, J. Li, H. Li, and Y. Fan, "Subwavelength optical localization with toroidal excitations in plasmonic and mie metamaterials," *InfoMat*, vol. 3, no. 5, pp. 577–597, 2021.

[19] R. S. Anwar, H. Ning, and L. Mao, "Recent advancements in surface plasmon polaritons-plasmonics in subwavelength structures in microwave and terahertz regimes," *Digital Communications and Networks*, vol. 4, no. 4, pp. 244–257, 2018.

[20] A. Rider, K. Ostrikov, and S. Furman, "Plasmas meet plasmonics: Everything old is new again," *The European Physical Journal D*, vol. 66, pp. 1–19, 2012.

[21] L. Wang, M. Hasanzadeh Kafshgari, and M. Meunier, "Optical properties and applications of plasmonic-metal nanoparticles," *Advanced Functional Materials*, vol. 30, no. 51, p. 2005400, 2020.

[22] M. I. Stockman, "Nanoplasmonics: fundamentals and applications," *Nano-Structures for Optics and Photonics: Optical Strategies for Enhancing Sensing, Imaging, Communication and Energy Conversion*, pp. 3–102, 2015.

[23] R. S. Anwar, H. Ning, and L. Mao, "Recent advancements in surface plasmon polaritons-plasmonics in subwavelength structures in microwave and terahertz regimes," *Digital Communications and Networks*, vol. 4, no. 4, pp. 244–257, 2018. [Online]. Available: https://www.sciencedirect.com/science/article/pii/S2352864817301992

[24] R. Zia, M. D. Selker, P. B. Catrysse, and M. L. Brongersma, "Geometries and materials for subwavelength surface plasmon modes," *JOSA A*, vol. 21, no. 12, pp. 2442–2446, 2004.

[25] G. Veronis and S. Fan, "Modes of subwavelength plasmonic slot waveguides," *Journal of Lightwave Technology*, vol. 25, no. 9, pp. 2511–2521, 2007.

[26] V. A. Zenin, R. Malureanu, I. P. Radko, A. V. Lavrinenko, and S. I. Bozhevolnyi, "Near-field characterization of bound plasmonic modes in metal strip waveguides," *Optics Express*, vol. 24, no. 5, pp. 4582–4590, 2016.

[27] O. Kozina, I. Nefedov, L. Melnikov, and A. Karilainen, "Plasmonic coaxial waveguides with complex shapes of cross-sections," *Materials*, vol. 4, no. 1, pp. 104–116, 2010.

[28] D. Dai and S. He, "A silicon-based hybrid plasmonic waveguide with a metal cap for a nano-scale light confinement," *Optics express*, vol. 17, no. 19, pp. 16 646–16 653, 2009.

[29] G. Li, C. M. De Sterke, and S. Palomba, "Fundamental limitations to the ultimate kerr nonlinear performance of plasmonic waveguides," *ACS Photonics*, vol. 5, no. 3, pp. 1034–1040, 2018.

[30] F. Renna, D. Cox, and G. Brambilla, "Efficient sub-wavelength light confinement using surface plasmon polaritons in tapered fibers," *Optics Express*, vol. 17, no. 9, pp. 7658–7663, 2009.

[31] W. Li, J. Wu, X. Li, and Z. Li, "Perovskite hybrid surface plasmon waveguide," *Plasmonics*, vol. 16, no. 6, pp. 1937–1944, 2021.

[32] Z. Han and S. I. Bozhevolnyi, "Radiation guiding with surface plasmon polaritons," *Reports on Progress in Physics*, vol. 76, no. 1, p. 016402, 2012.

[33] Y.-F. C. Chau, "Enhanced plasmonic waveguide sensing performance with a semicircular-ring resonator," *Micro and Nanostructures*, vol. 174, p. 207469, 2023.

[34] L. Niu, Q. Xu, X. Zhang, Z. Zhang, S. Li, X. Chen, Y. Xu, J. Ma, M. Kang, J. Han *et al.*, "Coupling plasmonic system for efficient wavefront control," *ACS Applied Materials & Interfaces*, vol. 13, no. 4, pp. 5844–5852, 2021.

[35] P. Berini, "Figures of merit for surface plasmon waveguides," *Optics Express*, vol. 14, no. 26, pp. 13 030–13 042, 2006.

[36] B. Dastmalchi, P. Tassin, T. Koschny, and C. M. Soukoulis, "A new perspective on plasmonics: confinement and propagation length of surface plasmons for different materials and geometries," *Advanced Optical Materials*, vol. 4, no. 1, pp. 177–184, 2016.

[37] M. Eldlio, Y. Ma, H. Maeda, and M. Cada, "A long-range hybrid thz plasmonic waveguide with low attenuation loss," *Infrared Physics & Technology*, vol. 80, pp. 93–99, 2017.

[38] J.-H. Zhu, X.-G. Huang, and X. Mei, "Double-teeth-shaped plasmonic waveguide electro-optical switches," *Chinese Physics Letters*, vol. 28, no. 8, p. 088501, 2011.

[39] S. Dahiya, S. Kumar, and B. Kaushik, "Hybrid plasmonic waveguide with centimeter-scale propagation length for nanoscale optical confinement," *Applied optics*, vol. 55, no. 36, pp. 10 341–10 346, 2016.

[40] H. C. Zhang, T. J. Cui, Y. Luo, J. Zhang, J. Xu, P. H. He, and L. P. Zhang, "Active digital spoof plasmonics," *National Science Review*, vol. 7, no. 2, pp. 261–269, 2020.

[41] X. Han, K. Liu, and C. Sun, "Plasmonics for biosensing," *Materials*, vol. 12, no. 9, p. 1411, 2019.

[42] S. I. Bozhevolnyi and N. A. Mortensen, "Plasmonics for emerging quantum technologies," *Nanophotonics*, vol. 6, no. 5, pp. 1185–1188, 2017.

[43] P. Ma, Y. Salamin, A. Messner, B. Bäuerle, A. Emboras, W. Heni, A. Josten, F. Eltes, S. Abel, J. Fompeyrine *et al.*, "Plasmonic modulators and photodetectors for communications," in *Broadband Access Communication Technologies XV*, vol. 11711. SPIE, 2021, p. 1171105.

[44] M. Klein, B. H. Badada, R. Binder, A. Alfrey, M. McKie, M. R. Koehler, D. G. Mandrus, T. Taniguchi, K. Watanabe, B. J. LeRoy *et al.*, "2d semiconductor nonlinear plasmonic modulators," *Nature communications*, vol. 10, no. 1, p. 3264, 2019.

[45] M.-H. Shih, "Small and fast plasmonic modulator," *Nature Photonics*, vol. 8, no. 3, pp. 171–172, 2014.

[46] N. Yang, M. J. Ryan, M. Son, A. Mavric, and M. T. Zanni, "Voltage-dependent ftir and 2d infrared spectroscopies within the electric double layer using a plasmonic and conductive electrode," *The Journal of Physical Chemistry B*, vol. 127, no. 9, pp. 2083–2091, 2023.

[47] Y.-L. Chang, C.-J. Su, L.-C. Lu, and D. Wan, "Aluminum plasmonic nanoclusters for paper-based surface-enhanced raman spectroscopy," *Analytical Chemistry*, vol. 94, no. 47, pp. 16 319–16 327, 2022.

[48] N. Mhlanga, T. A. Ntho, H. Chauke, and L. Sikhwivhilu, "Surface-enhanced raman spectroscopy substrates: Plasmonic metals to graphene," *Frontiers in Chemistry*, vol. 10, p. 832282, 2022.

[49] R. Grumich, T. Griggs-Demmin, M. Glover, and B. Negru, "Fabrication of stabilized gold nanoparticle oligomers for surface-enhanced spectroscopies," *ACS omega*, vol. 6, no. 47, pp. 31 818–31 821, 2021.

[50] X. Xiong, D. Clarke, Y. Lai, P. Bai, C. E. Png, L. Wu, and O. Hess, "Substrate engineering of plasmonic nanocavity antenna modes," *Optics Express*, vol. 31, no. 2, pp. 2345–2358, 2023.

[51] S. K. Patel and C. Argyropoulos, "Plasmonic nanoantennas: enhancing light-matter interactions at the nanoscale," *arXiv preprint arXiv:1511.03140*, 2015.

[52] A. Arumona, I. Amiri, S. Punthawanunt, and P. Yupapin, "High-density quantum bits generation using microring plasmonic antenna," *Optical and Quantum Electronics*, vol. 52, pp. 1–12, 2020.

[53] D. Lavrukhin, A. Yachmenev, I. Glinskiy, R. Khabibullin, M. Ryzhii, T. Otsuji, M. Shur, K. Zaytsev, and D. Ponomarev, "Plasmonic terahertz emitters with high-aspect ratio metal gratings," in *International Conference on Micro-and Nano-Electronics 2018*, vol. 11022. SPIE, 2019, pp. 9–13.

[54] Y. Shen, J. Zhou, T. Liu, Y. Tao, R. Jiang, M. Liu, G. Xiao, J. Zhu, Z.-K. Zhou, X. Wang *et al.*, "Plasmonic gold mushroom arrays with refractive index sensing figures of merit approaching the theoretical limit," *Nature communications*, vol. 4, no. 1, p. 2381, 2013.

[55] M. Naughton, K. Kempa, Z. Ren, Y. Gao, J. Rybczynski, N. Argenti, W. Gao, Y. Wang, Y. Peng, J. Naughton *et al.*, "Efficient nanocoax-based solar cells," *physica status solidi (RRL)–Rapid Research Letters*, vol. 4, no. 7, pp. 181–183, 2010.

[56] J. Wallentin, N. Anttu, D. Asoli, M. Huffman, I. Åberg, M. H. Magnusson, G. Siefer, P. Fuss-Kailuweit, F. Dimroth, B. Witzigmann *et al.*, "Inp nanowire array solar cells achieving 13.8% efficiency by exceeding the ray optics limit," *Science*, vol. 339, no. 6123, pp. 1057–1060, 2013.

[57] H. M. Yassin, Y. M. El-Batawy, and E. A. Soliman, "Enhancement of plasmonic photovoltaics with pyramidal nanoparticles," *Applied Optics*, vol. 62, no. 8, pp. 1961–1969, 2023.

[58] K. Nagpal, E. Rauwel, F. Ducroquet, and P. Rauwel, "Assessment of the optical and electrical properties of light-emitting diodes containing carbon-based nanostructures and plasmonic nanoparticles: a review," *Beilstein Journal of Nanotechnology*, vol. 12, no. 1, pp. 1078–1092, 2021.

[59] A. Fakharuddin, M. K. Gangishetty, M. Abdi-Jalebi, S.-H. Chin, A. R. bin Mohd Yusoff, D. N. Congreve, W. Tress, F. Deschler, M. Vasilopoulou, and H. J. Bolink, "Perovskite light-emitting diodes," *Nature Electronics*, vol. 5, no. 4, pp. 203–216, 2022.

[60] W. Du, T. Wang, H.-S. Chu, and C. A. Nijhuis, "Highly efficient on-chip direct electronic–plasmonic transducers," *Nature Photonics*, vol. 11, no. 10, pp. 623–627, 2017.

[61] F. Bilotti, S. Tricarico, and L. Vegni, "Plasmonic metamaterial cloaking at optical frequencies," *IEEE Transactions on Nanotechnology*, vol. 9, no. 1, pp. 55–61, 2009.

[62] W. Cai, U. K. Chettiar, A. V. Kildishev, and V. M. Shalaev, "Optical cloaking with metamaterials," *Nature photonics*, vol. 1, no. 4, pp. 224–227, 2007.

[63] J. Renger, M. Kadic, G. Dupont, S. S. Aćimović, S. Guenneau, R. Quidant, and S. Enoch, "Hidden progress: broadband plasmonic invisibility," *Optics Express*, vol. 18, no. 15, pp. 15 757–15 768, 2010.

[64] M. Song, D. Wang, Z. A. Kudyshev, Y. Xuan, Z. Wang, A. Boltasseva, V. M. Shalaev, and A. V. Kildishev, "Enabling optical steganography, data storage, and encryption with plasmonic colors," *Laser & Photonics Reviews*, vol. 15, no. 3, p. 2000343, 2021.

[65] F. Mao, A. Davis, Q. C. Tong, M. H. Luong, C. T. Nguyen, I. Ledoux-Rak, and N. D. Lai, "Direct laser coding of plasmonic nanostructures for data storage applications," in *Nanophotonics VII*, vol. 10672. SPIE, 2018, pp. 167–173.

[66] Y. Chen, X. Yang, and J. Gao, "3d janus plasmonic helical nanoapertures for polarization-encrypted data storage," *Light: Science & Applications*, vol. 8, no. 1, p. 45, 2019.

[67] M. A. El-Rabiaey, N. F. Areed, and S. S. Obayya, "Novel plasmonic data storage based on nematic liquid crystal layers," *Journal of Lightwave Technology*, vol. 34, no. 16, pp. 3726–3732, 2016.

[68] K. Yee, "Numerical solution of initial boundary value problems involving maxwell's equations in isotropic media," *IEEE Transactions on antennas and propagation*, vol. 14, no. 3, pp. 302–307, 1966.

[69] A. Taflove and M. E. Brodwin, "Numerical solution of steady-state electromagnetic scattering problems using the time-dependent maxwell's equations," *IEEE transactions on microwave theory and techniques*, vol. 23, no. 8, pp. 623–630, 1975.

[70] Y. Merle, "Etude de la dispersion électromagnétique dans les matériaux diélectriques bidimensionnels," Ph.D. dissertation, Limoges, 2003.

[71] W. K. Liu, S. Li, and H. S. Park, "Eighty years of the finite element method: Birth, evolution, and future," *Archives of Computational Methods in Engineering*, vol. 29, no. 6, pp. 4431–4453, 2022.

[72] S. Duczek and U. Gabbert, "Fundamental principles of the finite element method," *Lamb-Wave Based Structural Health Monitoring in Polymer Composites*, pp. 63–90, 2018.

[73] K. Y. Kim, *Plasmonics: Principles and Applications*. BoD–Books on Demand, 2012.

[74] F. Shamshad and M. Amin, "Simulation comparison between hfss and cst for design of conical horn antenna," *Journal of Expert Systems (JES)*, vol. 1, no. 4, pp. 84–90, 2012.

[75] J. Hoffmann, C. Hafner, P. Leidenberger, J. Hesselbarth, and S. Burger, "Comparison of electromagnetic field solvers for the 3d analysis of plasmonic nanoantennas," in *Modeling Aspects in Optical Metrology II*, vol. 7390. SPIE, 2009, pp. 174–184.

[76] A. Ali, F. El-Mellouhi, A. Mitra, and B. Aïssa, "Research progress of plasmonic nanostructure-enhanced photovoltaic solar cells," *Nanomaterials*, vol. 12, no. 5, p. 788, 2022.

[77] R. D. Piner, J. Zhu, F. Xu, S. Hong, and C. A. Mirkin, "" dip-pen" nanolithography," *science*, vol. 283, no. 5402, pp. 661–663, 1999.

[78] G. Liu, M. Hirtz, H. Fuchs, and Z. Zheng, "Development of dip-pen nanolithography (dpn) and its derivatives," *Small*, vol. 15, no. 21, p. 1900564, 2019.

[79] T. I. Awan, A. Bashir, and A. Tehseen, *Chemistry of nanomaterials: fundamentals and applications*. Elsevier, 2020.

[80] W. Escovitz, T. Fox, and R. Levi-Setti, "Scanning transmission ion microscope with a field ion source." *Proceedings of the National Academy of Sciences*, vol. 72, no. 5, pp. 1826–1828, 1975.

[81] A. A. Tseng, "Recent developments in nanofabrication using focused ion beams," *Small*, vol. 1, no. 10, pp. 924–939, 2005.

[82] M. Horák, K. Bukvišová, V. Švarc, J. Jaskowiec, V. Křápek, and T. Šikola, "Comparative study of plasmonic antennas fabricated by electron beam and focused ion beam lithography," *Scientific Reports*, vol. 8, no. 1, p. 9640, 2018.

[83] S. Y. Chou, P. R. Krauss, and P. J. Renstrom, "Imprint lithography with 25-nanometer resolution," *Science*, vol. 272, no. 5258, pp. 85–87, 1996.

[84] ——, "Nanoimprint lithography," *Journal of Vacuum Science & Technology B: Microelectronics and Nanometer Structures Processing, Measurement, and Phenomena*, vol. 14, no. 6, pp. 4129–4133, 1996.

[85] S. Y. Chou, P. R. Krauss, W. Zhang, L. Guo, and L. Zhuang, "Sub-10 nm imprint lithography and applications," *Journal of Vacuum Science & Technology B: Microelectronics and Nanometer Structures Processing, Measurement, and Phenomena*, vol. 15, no. 6, pp. 2897–2904, 1997.

[86] M. D. Austin, H. Ge, W. Wu, M. Li, Z. Yu, D. Wasserman, S. Lyon, and S. Y. Chou, "Fabrication of 5 nm linewidth and 14 nm pitch features by nanoimprint lithography," *Applied Physics Letters*, vol. 84, no. 26, pp. 5299–5301, 2004.

[87] C. V. Thompson, "Solid-state dewetting of thin films," *Annual Review of Materials Research*, vol. 42, pp. 399–434, 2012.

[88] P. J. Kelly and R. D. Arnell, "Magnetron sputtering: a review of recent developments and applications," *Vacuum*, vol. 56, no. 3, pp. 159–172, 2000.

[89] P. N. Hishimone, H. Nagai, and M. Sato, "Methods of fabricating thin films for energy materials and devices," in *Lithium-ion Batteries-Thin Film for Energy Materials and Devices*. IntechOpen, 2020.

[90] e. P. Franken, A. E. Hill, C. Peters, and G. Weinreich, "Generation of optical harmonics," *Physical review letters*, vol. 7, no. 4, p. 118, 1961.

[91] T. MAIMAN, "Stimulated optical radiation in ruby," *Nature*, vol. 187, no. 4736, pp. 493–494, 1960.

[92] R. W. Boyd, *Nonlinear optics*, 3rd ed. Academic Press, 2008.

[93] S. Khani, A. Farmani, and A. Mir, "Reconfigurable and scalable 2, 4- and 6-channel plasmonics demultiplexer utilizing symmetrical rectangular resonators containing silver nano-rod defects with fdtd method," *Scientific Reports*, vol. 11, no. 1, p. 13628, 2021.

[94] B. Rahmi, H. Badaoui, and M. Abri, "Original architecture of an efficient all-optical 2× 4 photonic crystals decoder based on nonlinear ring resonators," *Optical and Quantum Electronics*, vol. 54, no. 10, p. 676, 2022.

[95] E. Rafiee, R. Negahdari, and F. Emami, "Plasmonic multi channel filter based on split ring resonators: application to photothermal therapy," *Photonics and Nanostructures-Fundamentals and Applications*, vol. 33, pp. 21–28, 2019.

[96] O. Abbaszadeh-Azar and K. Abedi, "A wavelength demultiplexing structure based on the multi-teeth-shaped plasmonic waveguide structure," *Plasmonics*, vol. 15, pp. 1403–1409, 2020.

[97] I. Abderrahmane, B. Hadjira, and A. Mehadji, "Efficient 4 and 8 plasmonic wavelength demux with ultra high q-factor and low fwhm based on nano-rectangular resonators," *Optical and Quantum Electronics*, vol. 55, no. 2, p. 108, 2023.

[98] I. Abderrahmane, B. Hadjira, A. Mehadji, and R. Bachir, "High performance single mode plasmonic filter and efficient wavelength demultiplexing based on nanodisk resonators," *Optical and Quantum Electronics*, vol. 55, no. 5, p. 413, 2023.